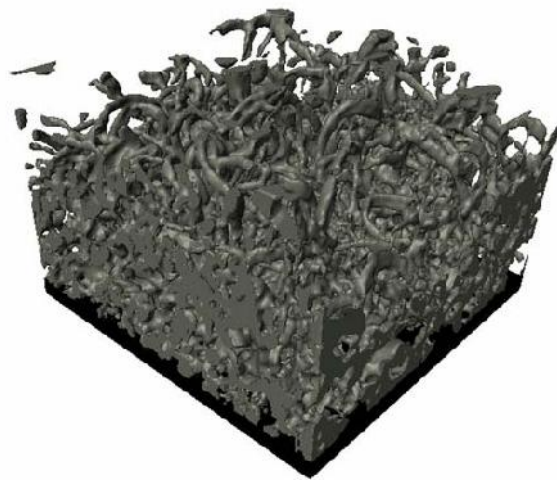# Topographical Control and Characterization of Al/Al$_2$O$_3$ Nanowire Coatings for Improved Osseointegration of Implant Materials

Dissertation

zur Erlangung des Grades des Doktors der Ingenieurwissenschaften
der Naturwissenschaftlich-Technischen Fakultät III
Chemie, Pharmazie, Bio- und Werkstoffwissenschaften
der Universität des Saarlandes

von

Marina Martinez Miró

Saarbrücken, Germany
2012

Tag des Kolloquiums: 22.02.2013

Dekan: Prof. Dr. V. Helms

Vorsitz: Prof. Dr. D. Scheschkewitz
Berichterstatter: Prof. Dr. Dr. h.c. M. Veith
     Prof. Dr. A. Ott
Akad. Mitarbeiter: Dr. G. Falk

Die vorliegende Arbeit wurde in der Zeit von Oktober 2009 bis Oktober 2012 am Leibniz Institut für Neue Materialien gGmbH unter Anleitung von Prof. Dr. Dr. h.c Michael Veith angefertigt.

Als meus pares

Abstract

Medical implants are a clinical reality and thousands of patients have been treated increasing in this way his life quality. Although many native materials have been used for bone implants, future biomaterials will include specific topographies to obtain the desired function. In this thesis, Al/Al_2O_3 nanowires (NWs) are suggested as possible coatings for improved osseointegration. The coatings have been fabricated by chemical vapour deposition (CVD) of the molecular precursor $[^tBuOAlH_2]_2$. Depending on the deposition time four different densely coated nanostructures have been obtained. A 3D-model has been reconstructed using the Focus Ion Beam/Scanning Electron Microscopy (FIB/SEM) technique and software reconstruction tools and the surface properties have been characterised using well known techniques. Finally, the prepared Al/Al_2O_3 NWs have been biologically tested. The Al/Al_2O_3 coatings are here studied as models for a better understanding of the topographic effect of the features on the cells independently from the chemical effect. Human osteoblast cells (HOB) and normal dermal human fibroblast cells (NHDF) were cultured separately on the deposited Al/Al_2O_3 NWs to investigate a possible selective cell adhesion. Additionally, gene experiments have been performed in order to understand the effect of the different topographies on the osteogenic gene expression. Lastly, the cell monolayer rheology (CMR) has been used to quantify the mechanical behaviour of the cells.

Kurzfassung

Medizinische Implantate sind in der klinischen Praxis eingeführt und die Lebensqualität Tausender behandelter Patienten hat sich damit erhöht. In dieser Arbeit werden Al/Al_2O_3 Nanodrähte (NWs) als mögliche Beschichtungen für eine verbesserte Osseointegration vorgeschlagen. In diesem Zusammenhang wurden Al/Al_2O_3 Schichten durch chemische Gasphasenabscheidung (CVD) des molekularen Präkursors $[^tBuOAlH_2]_2$ hergestellt. Je nach Dauer der Abscheidung wurden vier verschiedene Nanostrukturen gewonnen. 3D-Modelle wurden für jede dieser Nanostrukturen mit Hilfe der Fokus Ion Beam/Scanning Electron Microscopy (FIB/SEM) Technik rekonstruiert. Die Oberflächeneigenschaften wurden unter Verwendung etablierter Techniken charakterisiert. Schließlich wurden die vorbereiteten Al/Al_2O_3 NWs biologisch getestet. Die Al/Al_2O_3 Beschichtungen wurden hier als Modelle für ein besseres Verständnis des topographischen Effekts der Oberflächenmerkmale von Implantwerkstoffen auf Zellen unabhängig von der chemischen Wirkung des Werkstoffs selbst untersucht. Menschliche Osteoblasten (HOB) und normale dermale menschliche Fibroblasten (NHDF) wurden separat auf den abgeschiedenen Al/Al_2O_3 NWs kultiviert, um eine mögliche selektive Zell-Adhäsion zu untersuchen. Genexperimente wurden durchgeführt. Genexpression auf Al/Al_2O_3 NWs wurde quantifiziert. Schließlich hat die Zellmonoschicht Rheologie (CMR) verwendet worden, um das mechanische Verhalten der Zellen zu quantifizieren.

Acknowledgments

Firstly, I would like to express my sincere thanks to **Prof. Dr. Dr. hc. Michael Veith** for the chance to join his research group. It has been an honour for me. Thank you for the attention you paid to me and my work. Thank you for your enthusiastic predisposition, for the fruitful discussions and for your freedom and trust.

I would like to mention special thanks to all the people from the INM who helped me during these years:

- **Dr. Cenk Aktas**, group leader of the CVD/Life Science group, for helping me improve my career.
- Special thanks to **all the colleagues from the CVD/Life Science group**; Dieter Anschütz, Awadelkareem Ali, Stefan Brück, Cecile Dufloux, Sandra Litzenburger, Fadime Shain, Dr. Karin Löw, Ina Marsollek and Alexander May, for the nice and friendly working atmosphere.
- Sylvia de Graaf for giving always a solution to my logistic problems.
- Dietmar Serwas and all the workshop: Herbert Beermann, Johannes Berrar, Uwe Mager, Klaus Schmitt and Wermer Schneider for their help with all the devices.
- Melanie Groh and Elke Bubel from the library for their help during my literature search.
- Wolfgang Türk, Ralph Stoltz and Ralph Muth from the EDV.
- The former people from the AK Veith, Inorganic Chemistry department of the Universität des Saarlandes: Dr. Tatjana Kirs, Dr. David Kolano and Dr. Hameed Ullah.

I would like to mention special thanks to my dear colleagues and friends **Juseok Lee** and **Cagri Kaan Akkan**; walking our "PhD roads" together during these years built a very strong relationship between us. Thank you for everything, including KFC sessions and mensa discussions.

Also my sincere thanks to the experts who helped me with the material characterization:

- Thanks to **Dr. Falvio Soldera** and **Federico Miguel** (Material Science Department, Saarland University) for their work, suggestions and guidance concerning the FIB analysis.
- Thanks to **Johannes Maurer** and **Prof. Dr. Roland Bennewitz** (INM, nanotribologie group) for the roughness measurement using AFM technique.
- Special mention to **Dr. Vladimir Zaporojtchenko** (TF Kiel Universität – AK Prof. Fappel) who performed the XPS analysis. I had the pleasure to spend with him nice conference moments and the recent news about his unexpected death still shock me. Rest in peace.

I would like to express my thanks to all the cell experts who made this work possible:

- **Dr. Wolfgang Metzger, Benedikt Schwab, Lisa Schimmelpfennig, Prof. Dr. Tim Pohleman and PD Dr. Martin Oberringer** (Clinic of Trauma, Hand and Reconstructive Surgery, Saarland University, Homburg) for their collaborative works with the osteoblast and fibroblast cells, their suggestions, their interest and their continuous help. Thanks to **Prof. med. G. Wennemuth** for the SEM imaging of the cells.
- Collaborative Research Centre of Homburg from **AO foundation** and the **AO Reasearch Institute Davos** in Switzerland for the gene expression experiments.
- Thanks to **Mathias Sander** and **Prof. Dr. Albrecht Ott** (Biophysics Department, Universität des Saarlandes) for his collaborative work with the CMR technique. Thank you for introducing the CMR technique to me, for your suggestions and fruitful discussions.

Thanks to my dear friends here in Saarbrücken: Carla Sofia Amado, Salut Camilleri Rimbau, Stephan Rouven, Hassan Soumsoumani and Jana Kathrin for all the memorable moments we spent together.

Last but not least I would like to thank **my family**: **Andrés Martinez Gil, Conxita Miró Perez, Diana Martinez Miró and Ayman Haidar**. I have no words enough to thank you for the unconditional support, the encouragement in the difficult moments and for being the real rocks of my life. Gràcies per estar sempre al meu costat i ser la meva inspiració constant.

Table of contents

Symbols and Abbreviations

List of Abbreviations

0D	**Zero D**imensional
1D	**One D**imensional
2D	**Two D**imensional
3D	**Three D**imensional
AFM	**A**tomic **F**orce **M**icroscope
ALP	**A**lkaline **P**hosphate
ANOVA	**An**alysis Of **Va**riance between groups
BE	**B**inding **E**nergy
BSP	**B**one **S**ialoprotein
Cbfa1	**C**ore-**b**inding **fa**ctor subunit alpha-**1**
CMFDA	5-**c**hloro**m**ethyl**f**luoroscencein**dia**cetate
CMR	**C**ell **M**onolayer **R**heology
CVD	**C**hemical **V**apour **D**eposition
COL1	**Col**lagen **1**
DAPI	4´,6-**dia**midino-2-**p**henyl**i**ndole
DMEM	**D**ubelcco´s **M**odified **E**agle **M**edium
DMSO	**Dim**ethyl**s**ulf**o**xide
DNA	**D**eoxyribo**n**ucleic **A**cid
DRG	**D**orsal **R**oot **G**anglia
EBID	**E**lectron **B**eam **I**nduced **D**eposition
EBSD	**E**lectron **B**ackscatter **D**iffraction
ECM	**E**xtra**c**ellular **M**atrix
EDX	**E**nergy **D**ispersive **X**-Ray
FIB	**F**ocus **I**on **B**eam
FCS	**F**etal **C**alf **S**erum
HA	**H**ydroxy**a**patite
HOB	**H**uman **O**steoblast
HUVEC	**H**uman **U**mbilical **V**ein **E**ndothelial **C**ells
HUSMC	**H**uman **U**mbilical **V**ein **S**mooth **M**uscle **C**ells
ISO	**I**nternational **O**rganization for **S**tandardization

MAVI	**M**olecular **A**lgorithms for **V**olume **I**mages
MO_x	**M**etal **O**xides
mRNA	**M**essenger **R**ibonucleic **A**cid
NHDF	**N**ormal **H**uman **D**ermal **F**ibroblast
NW	**N**ano**w**ire
LD-NWs	**L**ow **D**ensity **N**ano**w**ires
MD-NWs	**M**iddle **D**ensity **N**ano**w**ires
HD-NWs	**H**igh **D**ensity **N**anowires
UHD-NWs	**U**ltra **H**igh **D**ensity **N**anowires
OC	**O**steo**c**alcin
OPG	**O**steo**p**rote**g**erin
OPN	**O**steo**pon**tin
PBS	**P**hosphate **B**uffered **S**aline
PVD	**P**hysical **V**apour **D**eposition
qRT-PCR	**q**uantitative **R**eal **T**ime **P**olymerase **C**hain **R**eaction
ROI	**R**egion **o**f **I**nterest
RMS	**R**oot **M**ean **S**quare
RNA	**R**ibo**n**ucleic **A**cid
RT	**R**oom **T**emperature
RT	**R**everse **T**ranscription (chapter 5)
Runx2	**Run**-related Transcription Factor **2**
SEM	**S**canning **E**lectron **M**icroscopy
SSP	**S**ingle **S**ource **P**recursor
TEM	**T**ransmission **E**lectron **M**icroscopy
UV	**U**ltra**v**iolet
Vis	**Vis**ible
VLS	**V**apour-**L**iquid-**S**olid
WST-1	**W**ater **S**oluble **T**etrazolium -**1**
XPS	**X**-Ray **P**hotoelectron **S**pectroscopy

List of Symbols:

r_0	radius of the contact area
S_0	contact angle defined by a modified Young's equation
S_v	specific surface area
$\emptyset$	diameter
	euler number
Φ	total porosity
V_v	volume density
τ	geometric tortuosity
R_a	roughness (arithmetic mean)
I_T	transmitted light
I_0	incident light
I_R	reflected light
I_S	scattered light
I_A	absorbed light
x_{lf}	surface free energy of liquid/fluid
x_{sl}	surface free energy of solid/liquid
x_{sf}	surface free energy of solid/fluid
$_{\prime\prime}x$	young contact angle

1

Introduction

In orthopaedics and dental surgery prostheses and dental implants have been used since decades. Nevertheless, lack of integration of the implants in surrounding bone tissue is sometimes noticed. The causes are still unclear. In order to optimize implant surface performance it is needed to have a better understanding about how cells and tissue interact with the implant surface. For years, several authors tried to describe and understand the mechanisms under the human bone cell response to materials used in orthopaedics and dental surgery for bone filling or bone replacement [1-6]. On the other hand, alumina (Al_2O_3) has been used for a long time in orthopaedic surgery due to its excellent biocompatibility, thin capsule formation and low coefficient of friction and wears rates[7,8] and various research groups showed the effectiveness of such ceramic coatings to improve the biocompatibility of implant materials[9-11]. Although many native materials have been used for bone implants, future biomaterials will include specific topographies and patterns on the native surface to obtain the desired function. In this thesis, one dimensional (1D) Al/Al_2O_3 nanowires (NWs) are suggested as possible coatings for improved osseintegration (Figure 1.1).
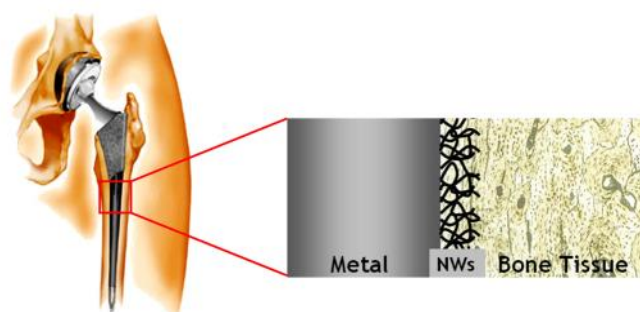
Figure 1.1: Schema: Nanowire coated layer between implant and bone tissue.

In **chapter 2** a brief state of the start is presented about 1D nanostructures and their use in biomaterials. It is explained the gas phase synthesis of 1D nanostructures through the vapour-liquid-solid (VLS) growth and some basics of chemical vapour deposition (CVD) technique are presented. Advantages and disadvantages of the CVD technique are listed as well as the key steps of the process. The synthesis of Al/Al_2O_3 nanostructures is explained in **chapter 3**. A background about the MOCVD of the precursor [^{t}BuOAlH$_2$]$_2$ is given where the properties of

the used precursor are reviewed. The production of stoichiometric bi-phasic composites using molecular precursors is summarized as well as the 1D growth of biphasic Al/Al_2O_3 NWs by self-catalysis from zero dimensions. A short overview about the functional applications of Al/Al_2O_3 nanostructured surfaces is also given. Last but not least, the experimental approach using the CVD technique for this thesis is introduced. All the parts of the CVD system used for this thesis are here described in detail as well as the process and parameters used in order to deposit the different Al/Al_2O_3 deposited nanostructures studied in this thesis. Depending on the deposition time four nanostructures with different nanowire density are obtained: low density nanowires (LD-NWs), middle density nanowires (MD-NWs), high density nanowires (HD-NWs) and ultra high density nanowires (UHD-NWs).

The deposited Al/Al_2O_3 coatings are characterized in detail in **chapter 4**. The FIB/SEM (Focus ion beam/Scanning Electron microscope) technique has been used for reconstruction of a 3D model for every Al/Al_2O_3 nanostructure. The data obtained from the reconstruction has been analysed using specific softwares in order to quantify some structural characteristics of our nanostructures. Besides, the surface properties, which are of high importance for the cell-interaction study, have also been analysed in this chapter using well known techniques.

In **chapter 5** the interaction of cells with Al/Al_2O_3 NWs prepared by CVD is studied. The Al/Al_2O_3 NWs are studied as models for a better understanding of the topography effect on the cell compatibility. A short introduction about the interactions between an implant and a host tissue is given as well as general explanations about the mechanisms involved in cell-surface interactions, protein interaction with a biomaterial and bone composition and formation. Some of the latest biocompatibility studies on nanostructures are reviewed as well as the more recent biocompatibility studies on surfaces prepared by CVD of $[^tBuOAlH_2]_2$. A detailed study about the selective cell adhesion of human osteoblast (HOB) and normal dermal human fibroblast (NHDF) on the different Al/Al_2O_3 nanowire coatings has been performed using *in vitro* cell culture techniques. Additionally, the osteogenic differentiation on the Al/Al_2O_3 NWs has been analysed and the effect of surface topography on changes in gene expression has been investigated. Lastly, the Cell Monolayer Rheology (CMR) technique has been used in order to understand cell-mechanical properties of fibroblast cells cultured on Al/Al_2O_3 NWs.

Finally, in **chapter 6** the main conclusions of this thesis are highlighted and a brief outlook about future work is presented.

2

State of the art

2.1 1D nanostructures

One dimensional (1D) nanostructured materials are those materials that have lateral dimensions in the range of 1 to 100 nm and lengths that can reach several micrometers. Since the discovery of carbon nanotubes[12] there has been a continuing growing interest in fabricating different one dimensional nanostructures, such as nanowires, nanorods or nanobelts. Nanowires and nanorods forms differ from the nanotubes in terms of their filled solid tubular structures. The nanobelt represents a quasi-one-dimensional nanostructure, which does not only have a specific growth direction. Furthermore its top/bottom surfaces and side surfaces exhibit well-defined crystallographic facets[13]. The synthesis of 1D nanostructures is extremely important in several areas such as: electronics, magnetism, optics, energy storage, electrochemistry and biomedical science. There are different methods for the growing of 1D nanostructures. Some of these methods are based on vapour phase techniques, while others are solution techniques. Physical methods such as nanolithography and other pattering techniques have been widely employed to fabricate 1D nanostructures, but chemical methods have been more versatile and effective in the synthesis of large amount of inorganic nanowires. Thus, chemical methods including precursor decomposition, solvothermal, hydrothermal and carbothermal reactions as well as chemical vapour deposition (CVD) have been widely employed to synthesize 1D nanostructures of different materials.

2.2 1D Alumina structures

Al_2O_3, alumina, is one of the most known metal oxides which attracted much interest in the recent years for several technical applications such as hard coatings[14], antireflective coatings on glass substrates[15], electrical insulators in electronic devices[16] and diffusion barriers which are protecting steel against high temperature oxidation[17]. Alumina micro fibres have been used for mechanical applications since 1980. Especially, alumina-whiskers-reinforced ceramic, metal and polymer composites are accepted as structural materials for high performance applications due to their excellent properties, such as low density, high strength and toughness. It is known that alumina fibres have a high melting point, high strength, light

weight and good wear resistances[18]. In order to increase the flexibility, strength and high temperature resistance of the matrix material, such fibres were added to ceramics, metals and polymers to obtain ceramic matrix composites, metal matrix composites and polymer matrix composites respectively. Several methods have been used to produce such fibres, for instance different sol-gel and colloidal synthesis. In these approaches the main problem was the control of size, shape and porosity within the fibre or whisker. Alumina is also extensively used as template for synthesising of 1D nano and microstructures. Anodic porous alumina is an ideal template for the controlled fabrication of nanostructures beyond the limit of the current lithographic techniques. Porous alumina has been used as a template to synthesize carbon nanotube[19]. Other way around, carbon nanotubes were used as templates to prepare different types of nanotubes of nanowires of Al_2O_3[20]. The use of a porous anodic alumina membrane template with ordered nanopores is known as one of the simplest methods to generate 1D Al_2O_3 nanostructures[21]. Other methods are also developed to synthesize 1D Al_2O_3 and metal-Al_2O_3 composite structures for instance lithography based top-down processes and bottom-up chemical approaches such as for instance thermal evaporation, catalyst supported CVD or carbothermal reactions.

2.3 Use of 1D nanostructures in biomaterials

It is known that some ceramics possess exceptional biocompatibility with bone cells and tissues[22]. The cytocompatibility of ceramics with grain sizes larger than 100 nm is well understood within last three decades[23]. On the other hand the biocompatibility of nanostructured ceramics (with grain sizes less than 100 nm) is still under intensive examination[24]. Compared to conventional ceramic formulations, enhanced adhesion of osteoblasts has been observed on nanophase alumina, titania, and hydroxyapatite[25]. Alumina nanofibres hold much promise for orthopaedic applications. The interest in alumina nanofibres has been growing exponentially due to their unique catalytic, mechanical, and surface properties[26]. Tepper et al. explained that compacts of alumina fibres improved osteoblast adhesion and proliferation as compared to notable orthopaedic/dental implant materials such as pure titanium and hydroxyapatite[27]. Similarly, Webster et al. showed increased cytocompatibility properties on theta and delta nanofibre alumina, but, in this study alumina fibres were compressed and there is no detailed information about their 1D morphology. In this context, the choice of the synthesis method is important to achieve 1D alumina nanostructures with controlled morphology and composition.

2.4 Gas Phase Synthesis of 1D Nanostructures: Vapour-liquid-solid (VLS) growth

In the simplest term, the vapour-liquid-solid (VLS) growth mechanism is a nanowire growth process, which utilizes a nanometre-sized metal alloy that is in liquid state during the nanowire growth. It is perhaps the most well-known nanowire growth mechanism, first put forward by Wagner and Ellis[28] and subsequently reviewed in detail by Wagner and Givargizov[29]. The primary feature of this growth mechanism is the liquid metal alloy droplet, which serves as the preferred site for nucleation due to its large accommodation coefficient compared with the surrounding solid surface. Over the years, numerous types of nanowire growths have been successfully attributed to this growth mechanism[30]. The growth mechanism of this process is known as catalyst droplet formation. The materials system used, as well as the cleanliness of the vacuum system and therefore the amount of contamination and/or the presence of oxide layers at the droplet and wafer surface during the experiment, greatly influence the absolute magnitude of the forces present at the droplet/surface interface and, in turn, determine the shape of the droplets. A balance of forces of surface tension and the liquid-solid interface tension determines the shape of a catalyst particle at the surface of a crystalline substrate. The radius of the droplet varies with the contact angle following the equation (2.1):

$$R = r_0 / \sin(s_0) \quad (2.1)$$

Where,

• r_0 : radius of the contact area

• s_0 : contact angle defined by a modified Young's equation

When the nanowire starts growing, its height increases by an amount *dh* and the radius of the contact are decreases as shown in the third picture in figure 2.1. Different line tensions will result in different growth modes.
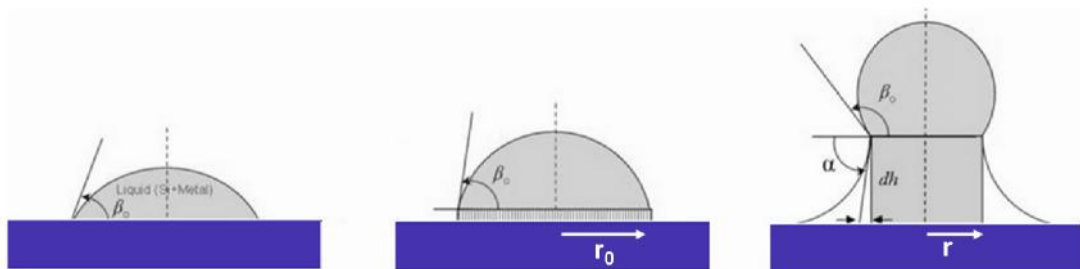
Figure 2.1: Catalysed droplet formation.

2.5 Basics of chemical vapour deposition (CVD) technique

Chemical vapour deposition (CVD) process is used to produce most metals and many non-metallic elements such as carbon and silicon. In this context, this process is used to manufacture coatings, powders, fibres, and monolithic components. A large number of compounds can be produced using chemical vapour deposition: carbides, nitrides, oxides, intermetallics, and many others. Chemical vapour deposition may be defined as the deposition of a solid on a heated surface from a chemical reaction in the vapour phase. It belongs to the class of vapour transfer processes, which is atomistic in nature that is the deposition species are atoms or molecules or a combination of these. Besides CVD, they include various physical-vapour deposition processes (PVD) such as evaporation, sputtering, molecular-beam epitaxial, and ion plating. In many respects, CVD competes directly with the PVD processes, but it is also used in conjunction with them and many of the newer processes are actually combinations of the two systems such as plasma-enhanced CVD or activated sputtering[31].

2.5.1 Advantages and disadvantages of the CVD technique

CVD has several important advantages, which make it the preferred process in many cases. These can be summarized as follows:

• It is not restricted to a line-of-sight deposition which is a general characteristic of sputtering, evaporation and other PVD processes. As such, CVD has high throwing power. Deep recesses, holes, and other difficult three-dimensional configurations can usually be coated with relative ease.

• The deposition rate is high and thick coatings can be readily obtained and the process is generally competitive and, in some cases, more economical than PVD processes.

• CVD equipment does not normally require ultrahigh vacuum and generally can be adapted to many process variations. Its flexibility is such that it allows many changes in composition during deposition and the co deposition of elements or compounds is readily achieved.

On the other hand CVD has some disadvantages:

• The requirement of having chemical precursors with high vapour pressure which are often hazardous and at times extremely toxic. This is not the case of our precursor.

• The by-products of the CVD reactions are also toxic and corrosive and must be neutralized, which may be a costly operation. This is not the case in our experiments.

2.5.2 Key steps of the CVD process

Several studies reported the kinetics and the mechanisms of CVD that provide the key information such as activation energy, and limiting steps of deposition reactions. This information is indispensable to understand the whole deposition process, which is indeed extremely complicated. The key factors of CVD are temperature and concentration gradient, geometric effects, and gas flow patterns in the reaction zones. Beside others, surface kinetics control and mass transport are very predominant[31]. Figure 2.2 shows the steps that are hypothesized to occur during a vapour deposition process.
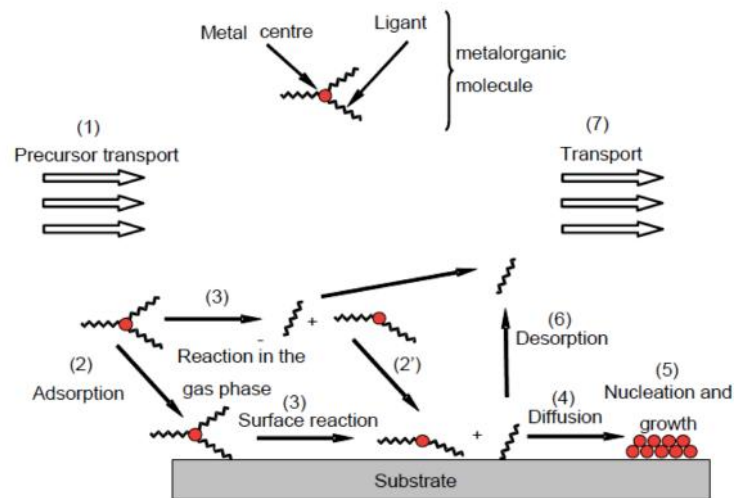
Figure 2.2: Schematic representation of the key steps of the CVD process[32].

1. The reactant species generate active gas.

2. The gaseous species are transported into the reaction chamber.

3. The gaseous reactants form intermediate species.

4. The gaseous reactants are absorved onto the heated substrate and the heterogeneous reaction occurs at the gas–solid interface (i.e. heated substrate). The deposit by-product species are produced.

5. The deposits diffuse along the heated substrate surface and form the crystallisation centre and growth of the film.

6. Removal of the gaseous by-products from the boundary layer through diffusion or convection.

7. Transport of the unreacted gaseous precursors and by-products away from the deposition chamber.

2.5.3 CVD of Alumina and precursors

Oxides are the largest groups of ceramic materials. Such materials are chemical inert, have good high temperature properties, and resistance to oxidation. Most oxides have a significant degree of ionic binding, since oxygen is the most electronegative divalent element. As a result they present instance optical transmission when pure, high electrical resistivity, low thermal conductivity, diamagnetism and chemical stability. Aluminium oxide (Al_2O_3) is one of the most preferred oxides in industrial applications due to its superior properties. In addition to bulk form, alumina can be applied as a thin film for various applications including insulation, corrosion protection and wear resistant surfaces[33]. Thin films of Al_2O_3 are deposited using wet processes such as sol gel spray coating, or physical vapour deposition, the thermal CVD process being the most often used. The classic way of producing alumina thin films by CVD is based on the hydrolysis of AlCl with a mixture of H_2 and CO_2 gases at temperatures between 700°C and 1000°C. The main disadvantage of this process is the corrosive by-product (HCl), which is suspected of facilitating whisker growth, instead of dense layers, on nickel-base super alloys. Alternative precursors have been investigated, in particular aluminium alkoxides, which undergo a pyrolitic decomposition forming alumina even at low temperatures, and in the absence of an oxidizing gas. Many efforts have been made to synthesize highly volatile and non-pyrophoric liquid precursors to deposit dense alumina films free from carbon. The potential of aluminium tri-isopropoxide to produce a suitable film structure with high yield was noted. These investigations concentrated on the low temperature process resulting in amorphous alumina thin films[34].

3

Synthesis of Al/Al$_2$O$_3$ nanostructures

It is well known that the synthesis of materials is directly related to the process and the starting materials. In this chapter the characteristics of the molecular precursor [^{t}BuOAlH$_2$]$_2$, as well as the CVD technique used for all experiments are summarized. The reliability of the results presented in this work depends, in part, on the ability to produce reproducible and repeatable coatings. For this reason, a detailed explanation about the configuration of a fully engineered self-built CVD device and the coating process are explained in detail. Last but not least, the experimental technique to achieve different 1D Al/Al$_2$O$_3$ nanostructures with different nanowire density, shape and distribution of the surface features is introduced.

3.1 Background: MOCVD of [^{t}BuOAlH$_2$]$_2$

3.1.1 Single source precursor [^{t}BuOAlH$_2$]$_2$

A single source precursor (SSP) is defined as a system which has been assembled by chemical interaction and which has a definite composition prior to its use in a sol-gel or gas-phase process[35-37]. In a more restricted definition, it is defined as a molecular entity, which is characterized, by a distinct composition, a molecular mass, a distinct volatility and a precise molecular structure[38-41]. In this context, the precise composition and bonding within the precursor may influence the chemical behaviour and several possibilities for material formation from a single source precursor have been defined[42]. For this work an SSP-III[43] precursor has been employed and as a result a multi phase system of two phases has been obtained in controlled stoichiometry. As both phases originate from a common precursor, their distribution in space is controlled by temperature and pressure of the CVD device. In this regard, the compound tert-butoxyalane [^{t}BuOAlH$_2$]$_2$ was synthesized in 1986 by Veith et al[43]. The molecular structure is illustrated in figure 3.1.
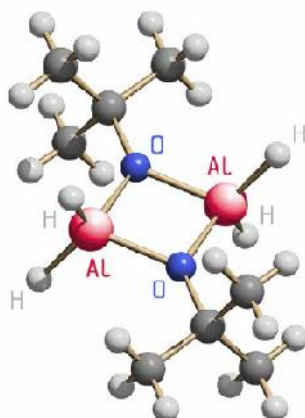
Figure 3.1: Molecular structure of the precursor [^{t}BuOAlH$_2$]$_2$.

The molecule crystallizes in a monoclinic crystal system in the space group P21/n. Two identical units constitute the molecule and it is composed of a centrosymmetric planar 4 membered-ring Al$_2$O$_2$. Tert-butoxy rests are attached to both trigonal planar coordinated oxygen atoms. The molecule constitutes an efficient single source precursor for the fabrication of hydrogen-aluminium-oxygen compounds or aluminium/aluminium oxide materials. This precursor is highly volatile and thermodynamically stable in gas phase, which is a prerequisite for use in the CVD process.

3.1.2 Production of stoichiometric bi-phasic composites using molecular precursors

Veith et al. first became aware of a chemical driven production of solid biphasic composites in 1994 when they discovered that the volatile molecule Sn[OC(CH$_3$)$_3$]$_3$Ba[OC(CH$_3$)$_3$]$_3$Sn on heating released iso-butene and tert-butanol and formed a solid composite Sn/BaSnO$_3$ [44]. On the first glimpse this reaction seemed to be a simple decomposition of the starting precursor; nevertheless, two observations turned out to be important. The ratio of tin (0) to tin (IV) found by XPS or chemical techniques revealed a constant value of 1.0; in other words, the composite always had the same stoichiometric amount of the two oxidation states of tin. Secondly, the composite formed without the usual carbon residues in the solid material (detectable mol % C lower than 0.1 %). The explanation of these findings is that this ''single source precursor process'' is driven by a chemical reaction, which takes place within the precursor molecule. For the composite Sn/BaSnO$_3$ the major reaction can be expressed through equation 3.1.

$$Sn \, [OC(CH_3)_3]_3Ba \, [OC(CH_3)_3]_3Sn \rightarrow Sn/BaSnO_3 + 3(CH_3)_3C-OH + 3(CH_3)_2C=CH_2 \quad (3.1)$$

Note, as only stable volatile compounds are evolved (detected in the on-line mass spectrometer), there is minor formation of organic radicals, which are supposed to be responsible for carbon contamination. Veith and colleagues were able to use this process also for the synthesis of compounds with germanium and lead instead of tin with the general formula M/BaMO$_3$ (M = Ge, Pb) and could transfer it to the simple metal/metal oxide composites (equation 3.2)[45].

$$M[OC(CH_3)_3]_2 \rightarrow M/MO_2 + (CH_3)_3C–OH+(CH_3)_2C=CH_2 \text{ (M=Ge, Sn, Pb) (3.2)}$$
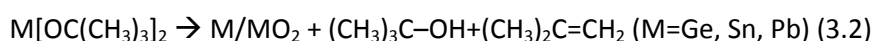
Generally, these cascade reactions within the molecule need temperatures around 300°C, but are run normally at much higher temperatures (500–700°C) in order to drive the disproportionation reaction of the metallic element to an end. Veith et al. found in the case of Sn[OC(CH$_3$)$_3$]$_2$ that at temperatures below 500°C the process compiled in equation 3.2 deviates leading besides the same volatiles tert-butanol and iso-butene to the formation of solid SnO[46]. From these findings it seems clear that the cascade reaction within the molecule leading to the organic products is separated from the disproportionation, leading to the composite.

3.1.3 One-dimensional (1D) growth of biphasic Al/Al$_2$O$_3$ NWs by self-catalysis from zero dimensions (0D)

Al- or alumina wires have been produced previously by catalyst-supported chemical vapour deposition using particles different from the source material as catalytic seeds. Fang et al. synthesized α-Al$_2$O$_3$ NWs in bulk quantity using physical evaporation of mixtures of pure Al powders and nanometre-sized TiO$_2$ powders[47], similarly, Ng et al. fabricated single crystal α-Al$_2$O$_3$ whiskers by displacement reactions using Al-rich powder mixtures containing different kind of metal oxides (MO$_x$)[48], Wang et al. showed polymer derivate ceramics[49] and To et al. obtained ultra thin α-Al$_2$O$_3$ nanobelts with single-crystalline rhombohedral structure by oxidizing Al in moisturized air under reduced pressure. Veith et al. reported for first time the mechanism used in order to get stoichiometric 1D Al/Al$_2$O$_3$ NWs from OD core-shell particles without use of a nobel metal seed[50]. Equation (3) shows the process in which the volatile single source precursor tert-butoxyalane reacts under anaerobic conditions and reduced pressure assembling the metal and oxide phases. The oxide layer in this nanocomposite is stoichiometric with a molecular ratio of Al^0/Al^{3+} = 1:2.

$$T > 400°C \qquad\qquad (3.3)$$

$$1/2\ [(CH_3)_3C\text{-}O\text{-}AlH_2]_2 \rightarrow 3/2\ H_2 + (CH_3)_2C\text{=}CH_2 + 1/3\ Al/Al_2O_3$$
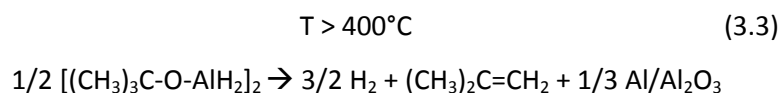
Al/Al$_2$O$_3$ core-shell nanowires are obtained using the same synthetic process as described in equation 3.3 but different conditions (equation 3.4). No external catalyst is needed in this process.

$$[(CH_3)_3C\text{-}O\text{-}AlH_2]_2$$

$$0\text{-}D\ Al/Al_2O_3 \rightarrow 1\text{-}D\ Al/Al_2O_3 \qquad\qquad (3.4)$$

$$T > 490°C$$
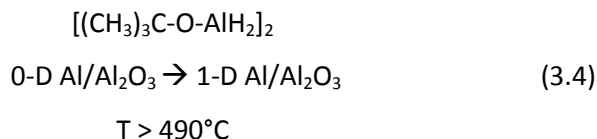
As in the VLS growth of ceramic nanowires it is believed that a liquid metal phase serves as seed[51]. In this case aluminium and not a nobel metal is forming a droplet. As a hypothesis this droplet could form from ball-like shaped fractal entities fusing together by Ostwald ripening[52]. Although the melting point of bulk aluminium is quite high (660.4 °C) the presence of alumina in the melt as well as the lowering of melting point due to the nanoscale could explain the existence of such an aluminium seed at these relatively low temperatures.

3.1.4 Functional applications of Al/Al$_2$O$_3$ nanostructured surfaces

In the last few years we found different applications and properties of the Al/Al$_2$O$_3$ NWs. In all cases the Al/Al$_2$O$_3$ NWs have been deposited on different substrates forming a coating. Such coating modifies the physical and chemical properties of the substrate. In this work Al/Al$_2$O$_3$ surfaces for biological applications (bone implant) are studied.

Adhesion: The Al/Al$_2$O$_3$ nanostructures exhibit adherence to various surfaces depending on their aspect ratio, their degree of interpenetration and entangling. The resulting coating may be used as permanent bonding for metals or ceramics. We showed that the resulting film composed of chaotic Al/Al$_2$O$_3$ NWs could be used as a sort of glue between metal or ceramic surfaces[53].

Solar absorbers: The Al/Al$_2$O$_3$ core-shell nanowire film exhibits a characteristic absorption of light (black colour). We have found that the nanowire films exhibit plasmon resonance absorption over a broad region of wavelengths. The nanowires lead to broadening and

plasmon splitting resulting in a broadband absorption, which can be interesting for ultra thin solar absorbers[54].

Hydrophobic/Hydrophilic bio-mimetic layers:

The stoichiometric Al/Al$_2$O$_3$ core/shell systems may be obtained as nanoballs or nanowires as described before. The fabrication of such surface materials can be tuned by the use of different temperatures and pressures in the same process with the effect that the created surface is no longer homogeneous but structured. In this regard Veith et al. presented such a surface obtained from the CVD of [^{t}BuOAlH$_2$]$_2$ at two different temperatures[55]. The micro- and nanotopography of the obtained artificial Al/Al$_2$O$_3$ surface compared well with the natural *Lupinus polyphyllus*. Barthlott showed that leaf surfaces like that of the lotus leaf family are water repelling[56]. He pointed out that nano-objects arranged in a micrometer array are necessary for that effect. It was therefore not a surprise when Veith and colleagues discovered that the Al/Al$_2$O$_3$ surfaces, under certain condition could even function as ultra-hydrophobic.

3.2 Experimental Approach: CVD technique

3.2.1 Synthesis of the single source precursor [^{t}BuOAlH$_2$]$_2$

The molecular precursor [^{t}BuOAlH$_2$]$_2$ was synthesised following well-established routes[57]. The synthesis starts with the dissolution of 4.554 g (120 mmol) LiAlH$_4$ in 80 ml of diethyl ether in a flask with a reflux cooler. A second dissolution of 5.334 g (40 mmol) of AlCl$_3$ in 80 ml diethyl ether is performed under cooling and added at room temperature to the LiAlH$_4$ already dissolved. In order to mix both dissolutions a steady flow is used. From the resulting mixture a precipitation of lithium chloride occurs. After precipitation, 11.859 g (160 mmol) of tert-butanole are added drop by drop to the suspension. During this step formation of hydrogen takes place noticeable by gas bubbles. After 4-5 h stirring at room temperature this procedure is over. Subsequently lithium chloride is separated by filtration and the solvent is evaporated under vacuum. The remaining solid is sublimed at ambient temperature and 100 Pa pressure obtaining 15.2 g bis (tert-butoxy aluminium dihydride) (93 % yield) (C$_4$H$_9$OAlH$_2$)$_2$. Decomposition temperature > 120 °C, melting point 71 °C, 1H NMR (in C$_6$D$_6$): δ = 1, 21 ppm (s); 4.43 ppm (s, breit). 13C NMR (in C$_6$D$_6$): δ = 30.36 ppm (s); 76.42 ppm (s). Values according to the literature[43]: 1H NMR (in C$_6$D$_6$): δ = 1.22 ppm (18H, C(CH$_3$)$_3$); 4.43 ppm (breit, 4H, AlH$_2$). 13C NMR (in C$_6$D$_6$): δ = 30.36 ppm (CH$_3$); 76.43 ppm (C(CH$_3$)$_3$).

3.2.3 Repeatability and reproducibility of the Al/Al$_2$O$_3$ nanowire coatings

According to ISO standard no. 354-1 (International Organization for Standardization, 1995a) repeatability is defined as the variation in measurements taken by a single person or instrument on the same item and under the same conditions. A measurement is repeatable when this variation is smaller than some agreed limit[58]. According to the Guidelines for Evaluating and Expressing the Uncertainty of NIST Measurement Results, the following conditions need to be fulfilled in the establishment of repeatability: Same measuring procedure, observer, measuring instrument (used under the same conditions), and location are needed and the repetitions should be done over a short period of time. On the other hand, reproducibility conditions are conditions where test results are obtained with the same method on identical test items in different laboratories with different operators using different equipment.

Table 3.1. Repeatability versus reproducibility according to ISO standard no. 354-1 (international Organization for Standardization, 1995a)

Repeatability	Reproducibility
= Observer	≠ Observer
= Measurement procedure	= Measurement procedure
= Measurement instrument (Under same conditions)	≠ Measurement instrument

In this context, for all experiments the same observer, using the same measurement procedure and a "self-built" and fully engineered CVD device, which has been specifically designed to ensure highly repeatable results and mass production, produced the samples. The size of the chamber is a key factor to produce an elevate number of samples per process and the engineering design of the device guarantees repeatability of the experiments. Veith et al. showed in several studies same coatings obtained with different devices and different observers, which prove also the reproducibility of the coatings.

Biological experiments require a lot of repetitions to ensure good statistical results, therefore such a specifically designed CVD device is more suitable than those ones used previously in a lab scale. For all biological experiments an elevated number of substrates have been required, so the experiments would not have been possible without a large-scale CVD device.

3.2.4 Chemical Vapour Deposition System Design

Generally speaking, every CVD system must fulfil some basic requirements[59-61] :

- To deliver and control all of the precursor gas, carrier gas and the diluent gas into the reaction chamber;

- To provide an energy source to initiate and drive the chemical reaction;

- To remove the by-product exhaust gases from the reaction chamber and to dispose them safely;

- To precisely control the process parameters (temperature, pressure, gas flow rate) automatically so that the quality of deposited products can be maintained from run to run.

For large-scale applications, some other additional requirements should be taken into account. These include the throughput, economy, safety and routine maintenance. Considering these requirements, our CVD system consists of several basic subsystems.
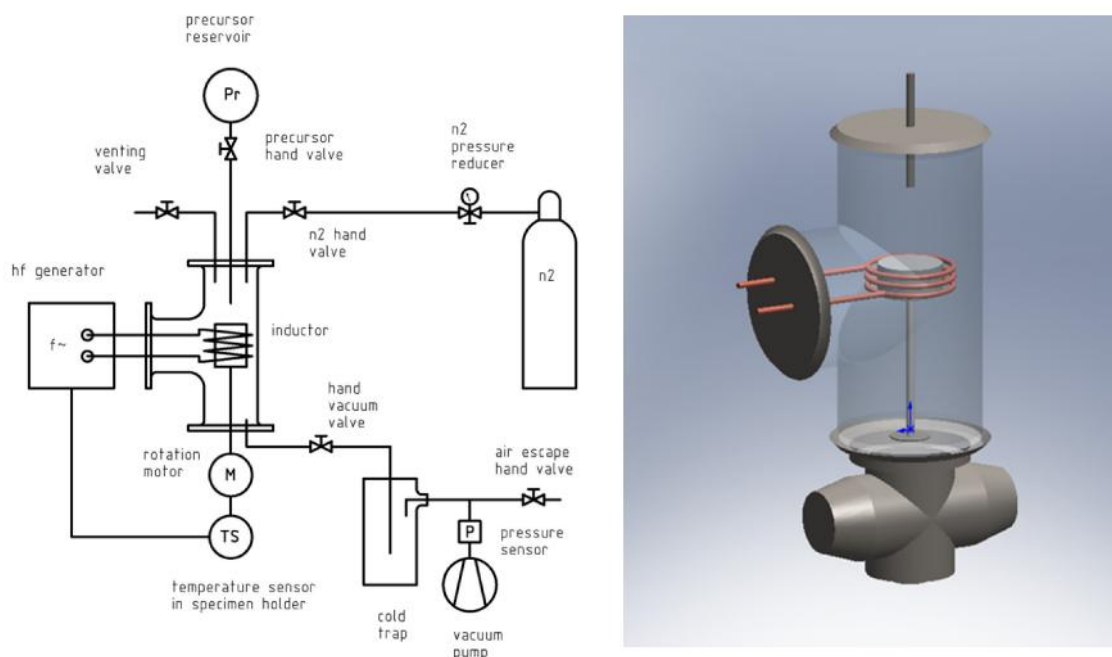
Figure 3.2: General scheme of the CVD system (left) and chamber model (right).

3.2.4.1 Precursor/gas delivery system

This subsystem is used to supply all needed gases into the chamber in a controlled manner. The metallic tube located in the middle of the top flange (figure 3.3 a, tube nº1) drives the precursor inside the chamber. The precursor is solid at room temperature and it volatiles and sublimes when the pressure is below 10^{-2} atm. No heating is needed for precursor sublimation.

Attached to the tube a glass corner with a manual valve was placed (figure 3.3 b). Such a manual valve is used to regulate the flux rate of the precursor into the chamber. During deposition, the precursor flux is regulated with this valve following the feedback of the pressure seen in a display measured by a pressure sensor. Through opening/closing the valve, and checking simultaneously the pressure value in the pressure display the optimal pressure is adjusted. In prior experiments a metallic valve was used but after a few runs it was blocked with precursor impeding further coatings. In order to avoid such problem a glass valve is used. The main advantages of the glass valve compared to the metallic one are:

- Transparency: it permits the observer to detect any material inside the valve.

- Whole size: it is wider than that one in the prior used metallic valve.

- Handling: it is easier to clean and to handle with.
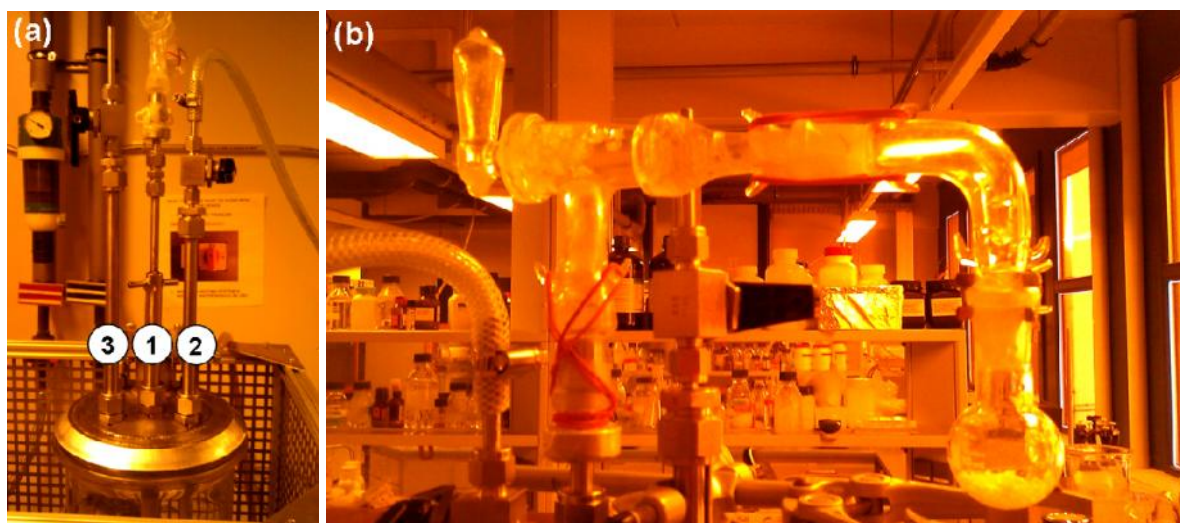
Figure 3.3: (a) Metallic flange located on top of the chamber for precursor/gas delivery. Tube nº1: precursor delivery, tube nº2: nitrogen delivery and tube nº3: ventilation valve (b) Glass corner containing manual valve.

A second metallic tube (figure 3.3 a, tube nº2) is used to inject the inert gas into the chamber. In our experiments gaseous nitrogen is flushed into the chamber several times before every deposition in order to eliminate residual oxygen and water in the apparatus. Gaseous nitrogen is also used to remove/replace the precursor in a save way avoiding moisture decomposition of the precursor. The precursor [^{t}BuOAlH$_2$]$_2$ reacts fast with water and even with atmospheric moisture (damp air) producing smoke containing a white solid of Al(OH)$_3$. The gaseous nitrogen is delivered from a 50 l, 200 bar gas bottle with compressed nitrogen through different valves into the reactor. The gaseous nitrogen was previously purified in order to

avoid any contamination in the chamber. Lastly, a third metallic tube (figure 3.3a, tube nº 3) is used for venting purposes. After decomposition and cooling down of the device to RT the metallic manual valve located in tube nº 3 is opened for ventilation.

3.2.4.2 Reaction chamber (reactor)

This subsystem is a key element, because this is where the reaction takes place. It consists of a vertical cold-wall glass chamber and three metallic flanges (Miethke Laborglass, GmbH). In our cold-wall CVD the susceptor and the substrates are heated by induction while the other parts remain cold. Therefore, the temperature on the walls of the reactor is colder than that one on the substrates. The three flanges are located in the inlet, outlet and inductive heating zone respectively. Through the three tubes of the inlet flange (figure 3.3a) the gases flow into the chamber. This flange is cooled down with a cooling system (in/out pumped water) during the experiment. This avoids high temperatures in the tubes, which may difficult the precursor flow into the chamber. The outlet flange connects the chamber to the other subsystems (cold trap, pipes) and the third flange is connected to the HF generator through a cupper coil responsible of the inductive heating of the susceptor and substrates.
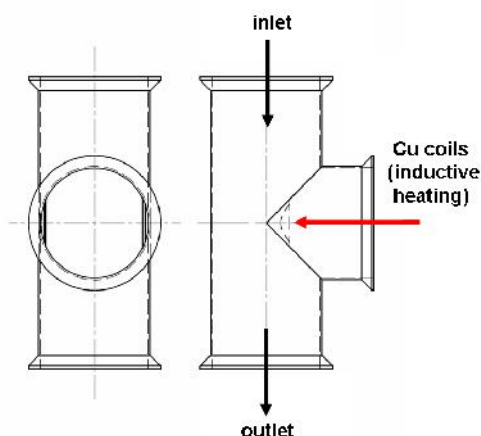
Figure 3.4: Cold-wall reactor

3.2.4.3 Loading/Unloading system

This subsystem is a mechanical system used to load/unload the susceptor and substrates from the inside to the outside of the reaction chamber and *vice versa*. It consists of a manual handle located at the bottom of the devices, which moves a metallic tube up and down through the chamber. In order to ensure a homogenous coating, it is important to place the susceptor with the substrates in the correct position. As it can be seen in the general scheme of the CVD system (figure 3.2), the susceptor is placed inside the chamber, concentric to the walls of the

chamber and to the inductive heating coils. Concerning its height, it is placed in the middle of the chamber between the spiral coils. When uploading the susceptor free particle gloves are used to avoid oil from fingerprints. After every experiment the susceptor is removed from the chamber through this subsystem.

3.2.4.4 Energy system

The functions of this subsystem are to provide the required energy for the precursor to react at elevated temperature, as well as to control and maintain the temperature inside the reaction chamber and on the susceptor and substrates. For this purposes, our system consists of an inductive heating system, several graphite susceptors (specifically designed for every substrate shape), a thermocouple and a temperature regulator. The inductive heating system consists of a high frequency generator (Linn High Term- HTG 1500/0.5, GmbH). Copper coils (cooled with water) are used to transfer the heat to the substrate by induction. Temperature measurement and control have been performed through a thermocouple (Linn High Term GmbH) attached to a temperature regulator (Linn High Term-800P, GmbH). In order to measure the temperature at any time, the thermocouple is introduced in a hole at the backside of the graphite susceptor (figure 3.5). A graphite susceptor was used as sample holder. The word "susceptor" is derived from susceptance, an electrical property of materials that measures their tendency to convert electromagnetic to heat. Some of the advantages of using graphite as susceptor are its low cost, good machining ability and the good heat conductivity.
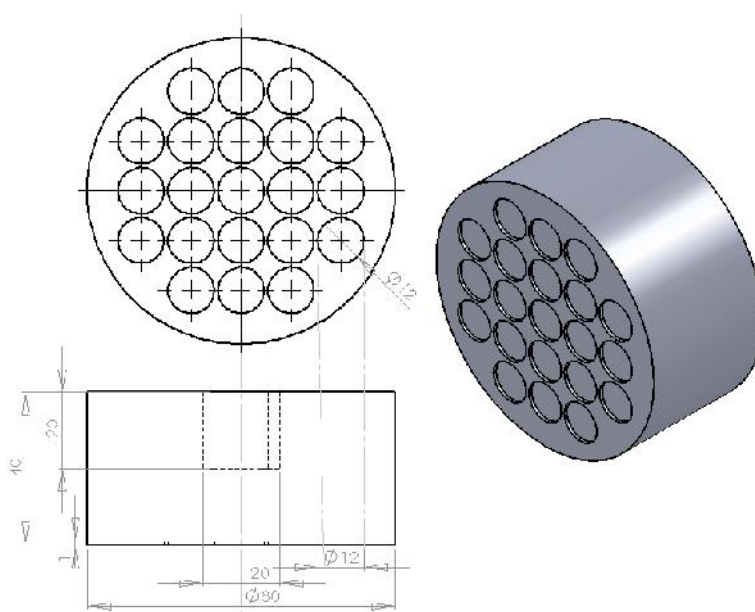
Figure 3.5: Graphite susceptor with 21 holes for samples having a diameter of 12 mm.

As shown in figure 3.5 the susceptor consists on round shaped graphite with a diameter of 8 cm and a thickness of 4 cm. In the frame of this thesis different substrates have been used depending on the experiment requirements, therefore different graphite susceptors have been designed. Figure 3.5 shows a graphite susceptor designed specifically for glass cover slips (Ø = 12 mm). In this case 21 samples can be coated in every experiment. In order to have optimum heat conductivity between the graphite and the substrate it is of high importance to adapt the graphite geometry as much as possible to the substrate shape.

3.2.4.5 Vacuum system

The vacuum system of our system consists mainly of a rotary pump, several pipes, connections and valves, O-rings and a sensitive pressure sensor. All these components are used to evacuate the gases, ensure anaerobic conditions inside the chamber and control the pressure during the reaction. Specifically, a pump (Vacuum Brand- PC3RZ6, GmbH) (table 3.2) has been used, which reaches a pressure after evacuation of 1.1 bar. Such a value ensures anaerobic conditions inside the chamber during deposition. The no-load speed at 50/60 Hz is between 1500 and 1800 revolutions per minute (rpm). Other technical conditions are specified in table 3.2.

Table 3.2 Technical specifications of the rotary vane pump

Technical specifications

Vacuum brand PC3RZ6, GmbH (rotary vane pump)

Maximum permissible inlet/outlet pressure (absolute): 1.1 bar

Permissible ambient temperature operation: +12 - +40 °C

No-load speed 50/60 Hz: 1500/1800 revolutions per minute (rpm)

Additionally, several bends, valves and pipes are used. It is important to minimise the loss coefficient of the flow glass caused by such components, thereby decreasing the residence time of the reactant gases within the reaction chamber and eliminating the undesirable deposition. Three silicon O-rings (DN 150, Miethke Laborglass, GmbH) are placed between the flanges and the vacuum chamber to ensure a good contact between glass and metal and an optimum vacuum. Last but not least, a sensitive pressure senor (ThyrCont USP52MA4) is

placed between lines, connected to a digital pressure reader in order to control the pressure during all the process.

3.2.4.6 Exhaust gas system

During the reaction non-reacted chemical substances and by products may flow into the exhaust lines. In order to release all these effluents safely to the atmosphere the following parts have been introduced into the device:

- A cold trap to condense the non reacted precursors as well as the by products of the reaction.

- A vent to provide fresh air and prevent gases from accumulating and to protect the pump.

The metallic cold trap (figure 3.6a, 1) is placed between the chamber and the pump. The functions of this cryogenic device are condensation and collection of volatile gases. In the frame of this thesis, it is important to remark that the precursor [^{t}BuOAlH$_2$]$_2$ is singular as it does not produce any radicals, which might spoil the apparatus. So H$_2$ and H$_2$C=C(CH$_3$)$_2$ are molecular by products which are easily evacuated. This is quite different from other CVD processes where the by products are worst characterized, and which are multiple. As an example, iso-butene may react further under certain circumstances to polymer or to carbon nanotubes (especially on Ni-surfaces).

The cold trap also cools down the hot exhaust gases from the reaction chamber. Such hot exhaust could increase the temperature of the pump oil, which may decrease its viscosity and therefore reduce the pumping efficiency. As a coolant, liquid nitrogen (-196°C), which is a perfect coolant and widely used in laboratory and industry, has been used. For the safety of the operator it is important to have eyes and skin protected when handling this coolant. A schematic of the cold trap is plotted in figure 3.6b.
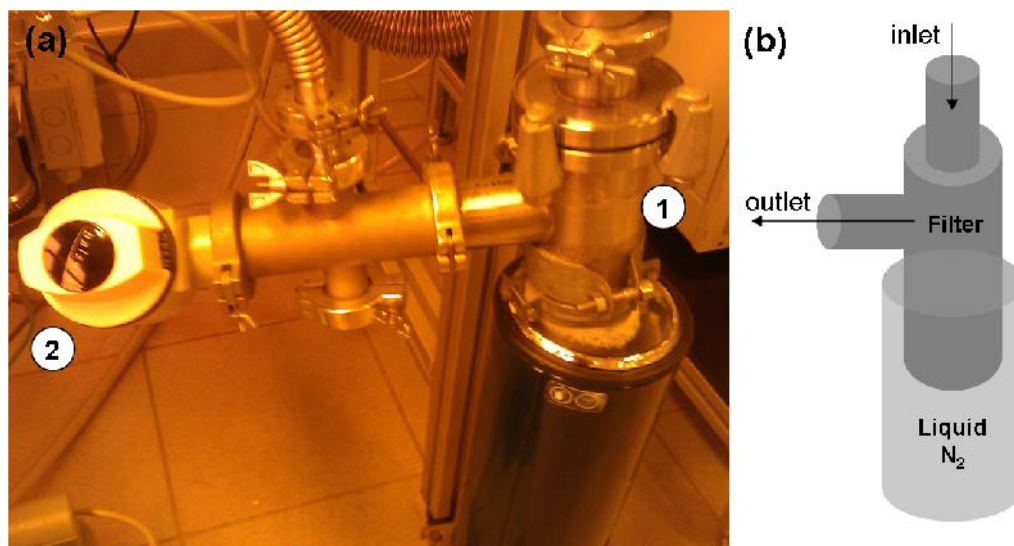
Figure 3.6: (a) Metallic cold trap (1) and manual ventilation valve (2) and (b) schematic of the cold trap.

Additionally, a hand valve is located between the cold trap and the pump for venting purposes and for pump protection (figure 3.6 a, 2). This valve is opened after every experiment allowing undesired gases and traces to go out from the cold trap.

3.2.5 Routine and maintenance of the system

In order to maintain the device under best conditions different routines have been implemented:

- After several runs all glass elements (chamber, corners, precursor valve and precursor reservoir) are removed and are placed in a KOH bath overnight in order to remove possible particles from the chamber and precursor accumulations in the glass valve.

- When the precursor is not subliming anymore, the precursor reservoir is removed under gaseous nitrogen and a new one is placed under same conditions. Low pressure and absence of reaction (no coating) indicates that the precursor is not subliming anymore.

- The metallic parts (cold trap, tubes, and flanges) are removed from time to time for cleaning procedure. These parts are cleaned in an ultrasonic bath and with detergent.

- After several experiments a thin film can be deposited on the graphite susceptor. This may cause bad conduction between substrate and susceptor affecting the homogeneity of the coatings. For precaution, new graphite susceptors are produced periodically.

3.2.6 Deposition of different Al/Al$_2$O$_3$ deposited nanostructures

Veith et al. found in previous studies different Al/Al$_2$O$_3$ deposited nanostructures. Mainly, the different structures where achieved after using different temperatures during the precursor decomposition[50]. In this thesis, the temperature has been fixed at 620°C and deposition time has been the variable parameter.

Prior to deposition, the single source molecular precursor [^{t}BuOAlH$_2$]$_2$ was synthesized under dry N$_2$ following the routes already described in 3.2.1 using standard Schlenk techniques. For deposition of the precursor, the vertical cold-wall chamber described in 3.2.4 was used. The substrates were heated using electromagnetic induction. Subsequently, the precursor [^{t}BuOAlH$_2$]$_2$ was decomposed on the heated substrates. Prior to decomposition the substrates were rinsed with ethanol, dried in the oven for 20 minutes and placed on the graphite holder.
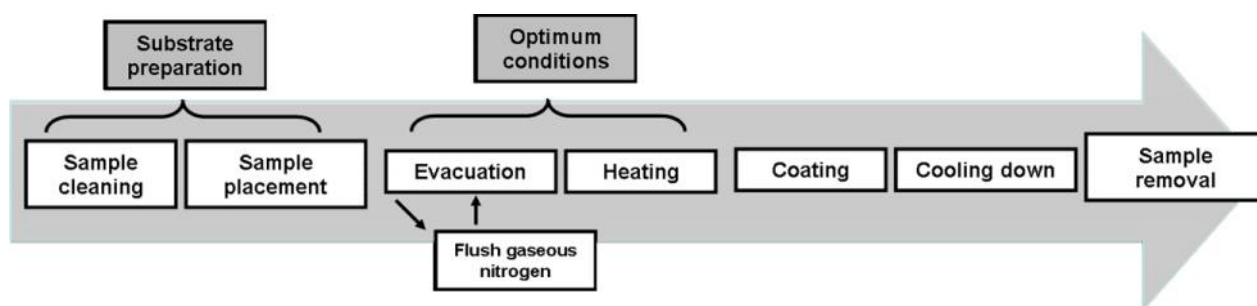
Figure 3.7: CVD process.

Figure 3.7 summarizes the CVD process used to achieve different Al/Al$_2$O$_3$ NWs coatings on the surface of the substrate. Firstly, the CVD chamber was evacuated ($9*10^{-3}$ mbar). Afterwards the chamber was flushed with gaseous N$_2$ several times in order to remove possible organic traces. The substrates were heated up to the working temperature by inductive heating (610-630°C) using an induction coil and a standard high frequency generator. Finally, the gas-phase deposition took place at the precursor subliming pressure ($8-9*10^{-2}$ mbar). The flow rate was controlled manually with a driven valve and a sensitive pressure detector.

Four deposition times were used giving as a result four different nanostructures (LD-NWs = Low density NWs, MD-NWs = Middle density NWs, HD-NWs = High density NWs and UHD-NWs = Ultra high density NWs). After deposition, the precursor valve was closed and the substrates were cooled down to room temperature under vacuum and removed from the chamber.

Table 3.4 Deposited Al/Al$_2$O$_3$ nanostructures depending on the deposition time

Al/Al$_2$O$_3$ deposited NWs	Deposition time (min)
LD-NWs (low density NWs)	5 ± 3
MD-NWs (middle density NWs)	15 ± 3
HD-NWs (high density NWs)	20 ± 3
UHD-NWs (ultra high density NWs)	≥ 30

4

Characterization of Al/Al$_2$O$_3$ NWs

In the previous chapter four different deposited Al/Al$_2$O$_3$ NWs sample types were introduced (LD-NWs, MD-NWs, HD-NWs and UHD-NWs) and defined in terms of nanowire density and deposition time during the CVD synthesis. The aim of this chapter is to define more precisely these sample types from the topographical, optical and chemical point of view. Scanning electron microscopy (SEM) has been performed for a first topographical analysis. Afterwards, Focus ion beam (FIB) nanotomography has been employed to build up a 3D model for every sample type. The 3D reconstruction data set gives a valuable basis for the determination of essential object feature parameters such as porosity, volume density (V_v), specific surface area (S_v), geometric tortuosity (τ), connectivity and Euler number (χ). Aspect ratio and thickness have been estimated using the 2D cross sectional SEM images obtained from FIB nanotomography and 2D porosity has been analysed for every sample type using 2D sectional binary images. In the frame of this work, 3D model reconstruction and quantitative characterization of the Al/Al$_2$O$_3$ NWs is especially interesting to understand the interaction of cells with the surface (chapter 5). Such reconstructions and quantitative analysis have not been presented so far.

Besides, surface properties have been analysed. It is known that surface features like topography and chemistry are influencing factors for cells. In this work, surface chemistry remains same for all samples and only topography changes depending on the deposited Al/Al$_2$O$_3$ nanowire structure. Such a model permits isolate the topography effect and study the cell response to only one of the main influencing factors. In this context, X-ray photoelectron spectroscopy (XPS) has been investigated in order to demonstrate that surface chemistry remains identical for every sample type. Micro and nanoroughness have been measured using profilometry technique and atomic force microscopy (AFM) respectively for topographical characterization. Surface behaviour with water and with glycerin has been studied using contact angle technique. Additionally some optical properties have been measured such has transmission and absorption. Transmission has been measured with a broad band spectrometer for classification of the Al/Al$_2$O$_3$ NW coatings according to their transmittance, and Ultraviolet– Visible spectroscopy (UV-Vis) technique has been used to analyse their absorption.

4.1 Characterization and modelling of Al/Al$_2$O$_3$ NWs using FIB-nanotomography

4.1.1 Introduction

Characterization techniques for materials science are particularly interesting if they are able to reveal the richness of the micro and nanostructure in three dimensions rather than just providing projection views. Nowadays, several three dimensional methods have been developed for the analysis of inorganic materials. For this work Focus Ion Beam (FIB) serial sectioning is chosen due to its characteristics. Very high resolution is needed due to the small diameter of the Al/Al$_2$O$_3$ NWs (20-30 nm). FIB technique has a resolution down to 10 nm, which allows the correct visualization of our nanostructure. Another particularity of FIB-nanotomography is that anisotropic voxel result from the combination of SEM and FIB. Moreover, different contrast methods can be used, which can characterize the crystallographic orientation (Electron Backscatter Diffraction – EBSD)[62] and composition of the phases (Energy Dispersive X-Ray – EDX)[63]. The last methods have not been used in this work. As a disadvantage FIB is a destructive method. The investigated region is almost completely removed, although the rest of the sample remains preserved. Nevertheless, this is not a problem for our study because several samples can be produced at the same time using the CVD technique (chapter 3). As it is shown in figure 4.1 only Transmission Electron Microscopy (TEM) and atom probe techniques can reach higher resolutions than FIB. As a disadvantage, both methods are limited to very small sample volumes and in the case of atom probe technique very special and sophisticated techniques are required for sample preparation[64-65]. X-ray tomography and synchrotron tomography are non destructive but the first has limited chemical sensitivity and the second is used specially for *in situ* observation of the microstructure development during dynamic processes[66], which is not needed for this work. Both techniques work at lower resolutions than FIB, which is not convenient for the visualization of our nanostructure.

On the other hand, in bone tissue engineering, the imaging modality that has been most extensively applied is X-ray tomography. The resolution required for analysing tissue synthesis and vascular ingrowth within porous materials is in the range of 1-30 microns. Micro-CT imagining combined with morphometric analysis algorithms is currently the gold standard for quantifying 3D changes in the volume and morphology of trabecular and cortical bone associated with skeletal fragility[67]. In this context, Bonse et al. computed human cancellous bone using X-ray tomography[68]. Also Guldberg and colleagues reported studies using 3D imaging techniques as a tool to quantify extracellular matrix formation and vascular ingrowth within porous biomaterials[69]. Lately, Bashoor-Zadeh et al. performed a geometric analysis of porous bone substitutes using same technique[70].
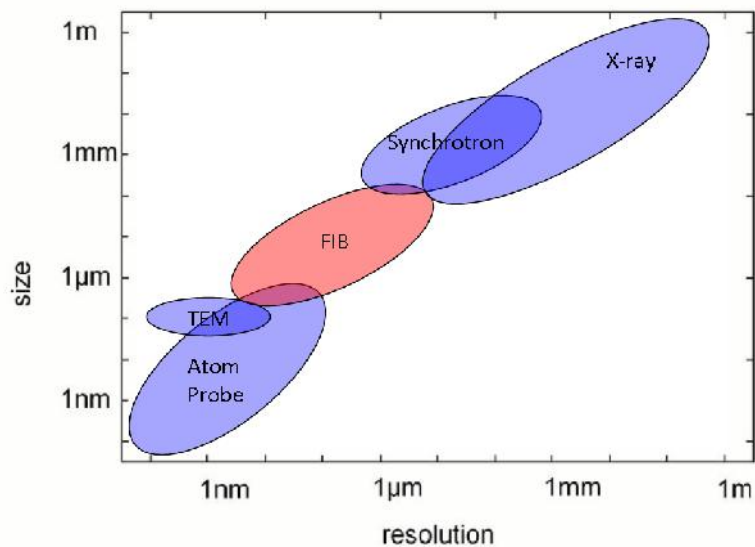
Figure 4.1: length scales of micro and nanotomography techniques showing lateral versus depth resolution ranges for different techniques (adapted from [71]).

In this context, Al/Al$_2$O$_3$ deposited NWs have been analysed and modelled for first time using FIB tomography. FIB tomography, also known as FIB nanotomography or FIB microstructure tomography in the literature, is a technique consisting on serial cutting. Series of slices are milled in situ using the focused ion beam technique and consecutively are imaged by the ion beam itself or by an electron beam in its different contrast mechanisms. The development of the dual beam work stations having scanning electron microscopy combined with a focus ion beam opened the possibilities for more precise serial sectioning tomography. Steiger et al.[72] and Rüdenauser et al.[73] reported in the 1980s the first approaches of 3D analysis of materials using FIB technique. On both studies the serial sectioning took place locating the FIB parallel to the surfaces of analysis. Most of the reported applications concern structural imaging of metallic and ceramic samples[74-78] and the technique has become very popular in the recent years mainly in semiconductor industry[79]. Nevertheless, FIB measurements have also been performed on polymeric samples[80], polymer/clay nanocomposites[81] and biological specimens[79].

4.1.2 Experimental approach

4.1.2.1 Sample preparation

4.1.2.1.1 Synthesis of Al/Al$_2$O$_3$ NWs

For this experiment, stainless steel 316L (Goodfellow, Germany) with a thickness of 0.9 mm and of 15 mm X 15 mm size was used as substrate. In order to remove any residue on the substrate surface,

the substrates were rinsed with isopropanol and dried at 180 °C for 20 minutes. Al/Al$_2$O$_3$ NWs were deposited on the stainless steel plate by CVD technique using the molecular precursor [^{t}BuOAlH$_2$]$_2$. Afterwards, the substrates were placed on the graphite susceptor. For this experiment a flat graphite susceptor was used. The graphite susceptor was placed concentrically to the inductor coil and the CVD process took place as described in chapter 3. After deposition the chamber was cooled down to RT and the samples were removed from the chamber. For every deposited nanostructure around 25 samples were fabricated. A total amount of 100 samples was prepared for this experiment.

4.1.2.1.2 Scanning Electron Microscopy (SEM)

It is essential to make a first topography investigation using Scanning Electron Microscopy (SEM) in order to choose the correct technique and parameters for further 3D reconstruction. For this purpose, the deposited Al/Al$_2$O$_3$ NWs were imaged with a scanning electron microscope (JEOL-JSM-6400F) at accelerating voltage of 15 kV. They were previously coated with gold using PVD sputter (JEOL-JFC-1300 Fine Coater, t = 30 s) to avoid charge on the surface.

4.1.2.1.3 Preparation of the Region of Interest (ROI)

Two main aspects have to be taken into consideration when analysing 3D arrangements. On one hand, the selected volume to analyse has to be large enough to allow the statistically relevant conclusions about the microstructure and to acquire reliable predictions about the calculated material properties. Realistic volumes, which can be analysed with FIB-nanotomogrpahy, vary depending on the used ion beam current from $1 \times 1 \times 1$ µm³ to about $100 \times 100 \times 100$ µm³ [82]. On the other hand, the voxel size (i.e. resolution) has to be small enough to provide exact characterization of the nanostructures [83]. In order to precede with the FIB-tomography investigation of the deposited Al/Al$_2$O$_3$ NWs a Helios Nanolab 600 from FEI was used. A region of interest of a size 5µm x 5µm x 5µm was selected for every analysed sample. Taking into account that the Al/Al$_2$O$_3$ NWs diameter is around 20-30 nm, the chosen volume of the region of interest (ROI) is big enough to obtain a representative model of the structure. The small size of the ROI allows working with almost the maximal resolution possible: the voxel size of the analysed samples is: x = 3.6 nm, z = 4.5 nm and y = 10 nm.

Afterwards, a protective layer of Pt was deposited over the area of investigation as it is seen in figure 4.2a and 4.2b using electron beam induced deposition (EBID). This technique is an *in situ* CVD deposition. A gaseous precursor is introduced in the SEM chamber close to the area of the sample. Absorption takes places on the surface and through the energy delivered by the electrons of the beam; the absorbed gas decomposes and a deposition layer is formed. Such a layer is needed for protection of the sample against further working with ions. It also suppresses the curtaining effects

improving in this way the polishing quality of the cross sections. Between the sample surface and the Pt layer, a sharp edge of the surface is obtained. This sharp edge will be used as reference during the sample alignment afterwards. As it is shown in figure 4.2c, a script (cross) has been FIB-milled into the top surface of the sample. This mark is used for repositioning of the sample after moving the microscope stage between serial-sectioning milling and image-analysis positions[84].
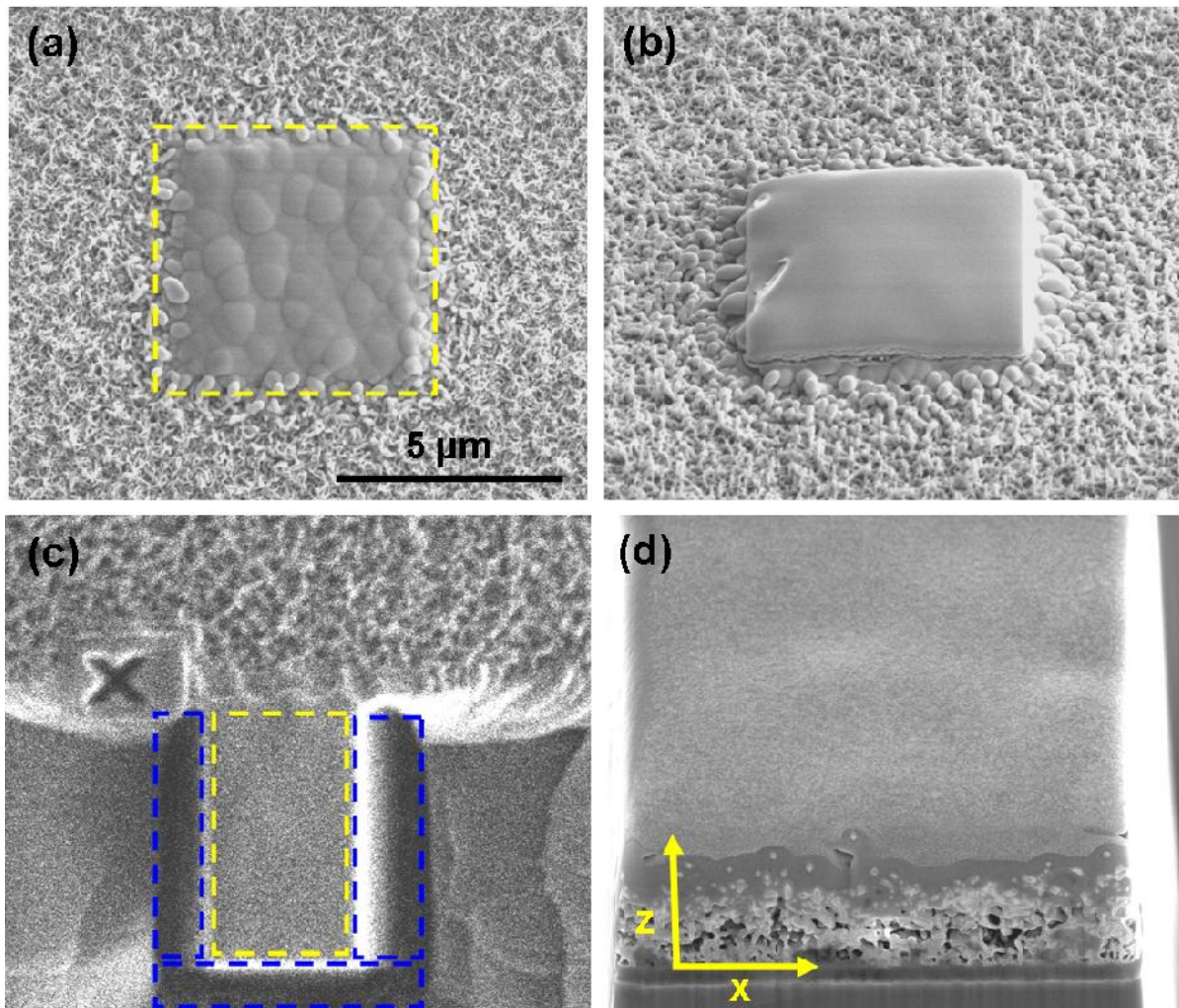
Figure 4.2: Sample preparation for the FIB serial sectioning. (a) Selection of the ROI (yellow area) and Pt deposition on it (b) deposited protective Pt layer on the ROI (c) ion-milled trench (blue rectangles) around the ROI and script (cross) (d) view of the first cross section by SEM technique.

After sample protection with the Pt layer the sample was tilted (surface perpendicular to the ion beam) and some material was removed around the ROI using the ion beam with the highest current available. As a result, three ion milled trenches were obtained (figure 4.2c, blue areas); one in front of the ROI and the other two at the left and right sides. The ion-milled trench in front of the ROI is needed in order to enable a good view of the cross section with the electron beam. This trench has to be deep enough to guarantee a good imaging with the electron beams. The ion-milled trenches at

the right and left sides should be large enough to avoid material redeposition on the sides. This redeposited material could disturb the view of the cross sections. Moreover, the right trench avoids shading effects in the deeper zones of the SEM images. Shading could occur because the secondary electron detector is located at the right side. After removing enough material around the ROI we proceeded with the serial imaging. The first image of the series can be seen in figure 4.2d.

4.1.2.1.4 Serial Sectioning

This technique consists of the milling of thin slices of material with ions. After milling every slice, successive images were obtained with electrons. The angle between the electron and ion beam is 52° as it is shown in figure 4.3a.
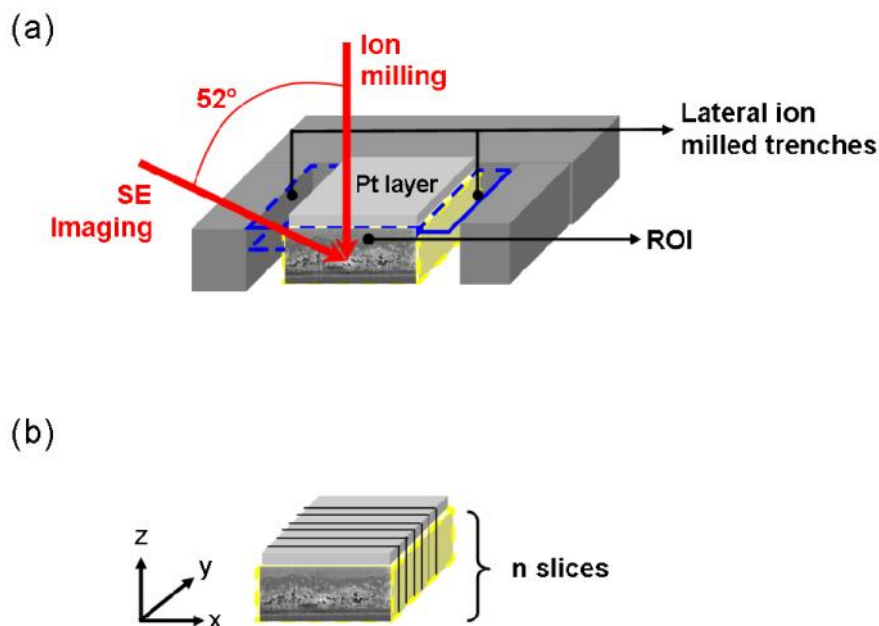
Figure 4.3: (a) Schematic FIB cross section imaging method indicating both the direction of the ion- and e-beams at the edge of the ROI. The angle between the electron and ion beam is 52°. (b) n-slices are obtained along the y-direction.

The ion beam was operating at 30 kV and a current of 27 pA. Small current values are typical for small cross sections as in our case. The script (cross) shown in Fig 4.2c was used in order to control the electron and ion beams and the Auto Slice & View software (FEI Company) was supporting equipment. Milling a slice took between 30 s and 2 minutes depending on the samples and the ion current used and imaging with electrons took between 20 s and 90 s. We obtained around 300 slices per sample. Therefore, the serial sectioning process took between 5 and 10 hours for every examined sample.

4.1.2.1.5 Imaging

For the imaging, a Helios Nanolab 600, from FEI Company was used. It consists of a high-resolution scanning electron microscope (SEM) equipped with a field emission gun and a focused ion beam (FIB). SEM images were acquired at a magnification of 35000 X. Digital resolution of the images depends on the scan velocity and can be calculated from the magnification and image size (1024 x 884 pixels). The dwell time was 30 µs, the acceleration voltage was 5 kV, and a current of 172 pA was applied.

4.1.2.1.6 Image analysis techniques and 3D reconstruction

For every Al/Al$_2$O$_3$ NW structure, the data set was processed using the following pack of software:

- ***Amira:*** Amira is a modular and object-oriented software system. Its basic system components are modules and data objects. Modules are used to visualize data objects or to perform some computational operations on them. Several modules were used in order to convert the 2D data into 3D model.

- ***Modular Algorithms for Volume Images (MAVI):*** MAVI is a software for 3D image processing developed by Fraunhofer ITWM especially for the analysis of volume images of complex microstructures as they can be found in materials like fibre reinforced composites or open and closed all foams. MAVI focuses on the characterization of the complex geometry of microstructures. Volume, surface, integrals of curvature and Euler number are determined for the whole structure or isolated objects. Anisotropies and preferred directions are not only found but their strength is measured, too. This core is complemented by various filters and transforms, techniques for image segmentation and object isolation, and functions for easy handling of huge image data sets. For special applications, several analysis tools are combined into user-friendly modules with few parameters and formatted output. MAVI provides local analysis methods, e.g. for local porosity, thickness or orientation analysis[85]. After reconstruction, some data sets are obtained from Amira software, mainly 2D binary sections. Such data can be operated in the MAVI obtaining as a result several basic field features.

- ***Image J:*** This is an image processing and analysis in Java open source software and it was used for image binarization and quantification of the 2D porosity.

The data sets obtained from FIB-nanotomography were processed with the software described above following the steps:

Alignment of the 2D SEM cross-sections (consecutive slices): After FIB/SEM procedure some SEM images are misaligned relatively to each other. Before a three dimensional model of the sample can be reconstructed the images have to be aligned taking into account translation and rotation. This task was performed manually using the "Align Slices" module[86]. A basic manual alignment was used.

Dimension correction according to the tilt of the electron beam: The absolute dimensions in the x-direction were obtained from a calibrated SEM magnification. Distances in the z-direction were corrected for projection effects taking into account the oblique SEM imaging at an angle of 52º using the relation z real = z SEM image/sin (52°). The y-values correspond to the layer thickness and it was 10 nm.

Crop-out of a sub volume: For further data processing a representative sub volume was defined. Cropping the data is useful if you are interested in only a part of the field. A sub volume was obtained for every Al/Al$_2$O$_3$ NWs nanostructure representing the average structure. This step was done in order to avoid possible deformations on the corners. Furthermore, some operations during segmentation and labelling have been done manually and a small volume simplifies these tasks. The size of all samples was 1 µm x 1 µm on the base and the high varied depending on the thickness of the nanostructure. Fig 4.4 shows a cropped area for one of the samples where a sub volume is selected.

This task was performed using the "Crop" tool from the amira software.
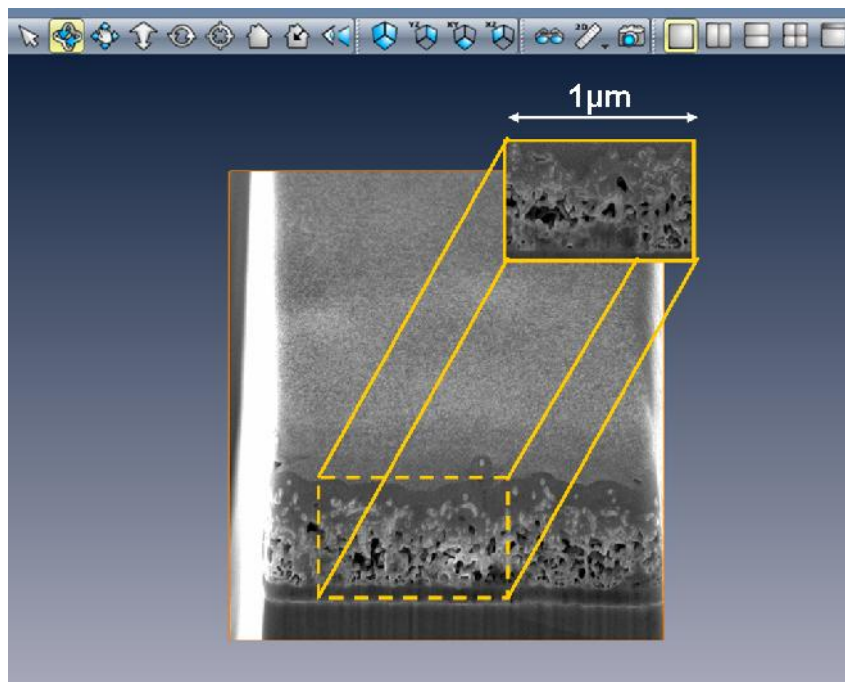
Figure 4.4: Cropped area from one of the samples using amira software system.

Segmentation and labelling of the Al/Al$_2$O$_3$ NWs: In order to distinguish clearly the Al/Al$_2$O$_3$ NWs from the Pt layer and the holes between nanowires segmentation and labelling were performed using the "image segmentation" editor of the amira software. The software offers a large set of segmentation tools from purely manual to fully automatic. Among them, "thresholding" tool was used to select the nanowires as it is shown in figure 4.5.
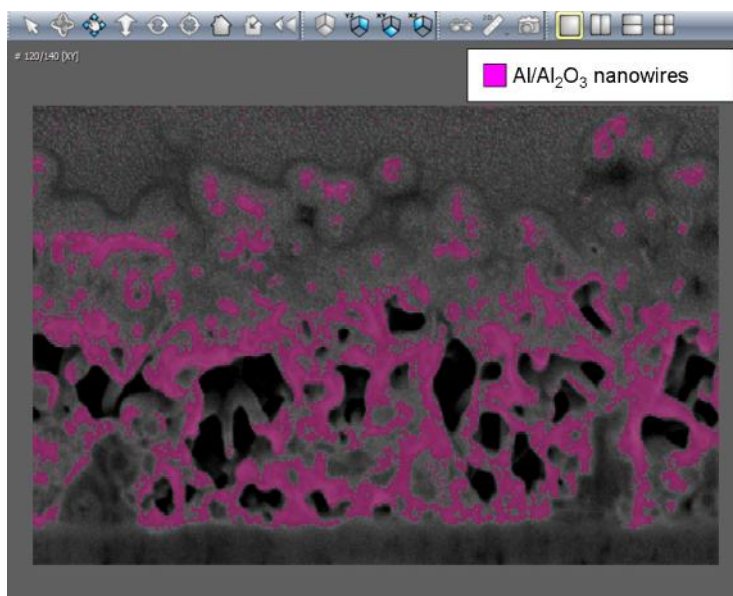
Figure 4.5: Nanowire labelling using amira software system.

The Pt was also segmented using this tool. The selection was done in one slice and automatically interpolated to all other slices. The "Lasso" tool (contouring) was used to select the substrate, and then the selected contour was automatically interpolated to all slices. After thresholding nanowires and Pt and contouring the substrate, still some noise was present and some non-desired areas were selected as nanowires or Pt. In order to correct such errors consequence of the automatic thresholding the segmentation was refined manually slice by slice. Mainly the tools "remove islands" and "magic wand" (region growing) were used. Since the editor does not store contours surrounding regions but region labels, a unique and well-defined classification is guaranteed.

Resampling the data for 3D image generation:

For 3D image data sets, isosurfaces are useful for providing an impression of the 3D shape of an object. An isosurface encloses all parts of a volume that are brighter than some user-defined threshold. Prior, resampling is needed. The resampling process will produce a data set with a coarser resolution. Although this is not necessary for the isosurface tool to work, it decreases computation time and improves rendering performance. The resample module is a computational module.

Quantitative analysis of 3D and 2D images:

After reconstruction with amira software, the three dimensional characterization was carried out with the help of the software system MAVI (Modular Algorithms for Volume Images). The 3D images were processed and analysed. MAVI´s core is complemented by various filters and transformations, techniques for image segmentation and object isolation. In order to perform accurate characterization at the first step, the voxel dimensions was specified and the stack of images was segmented. The object features were determined. The algorithms used in MAVI to perform the measurement of characteristic structure parameters are somewhere else described in detail[87-90].

4.1.2.1.7 Error during FIB-nanotomography

As the method that we are using for modelling the 3D Al/Al$_2$O$_3$ NWs requires several software and computational procedures, it is a fact that exists an error in the measurements. It is still very difficult to quantify the exact error because different techniques and software are used for a single reconstruction; nevertheless, the main sources of error have been detected. It is known that at higher magnifications there are some limitations in resolution and potential errors in thresholding could become visible. Segmentation by simple thresholding is thus one of the largest sources of uncertainty and potential error. More sophisticated methods such as edge-detection procedures and watershed segmentation may be applied in the future to minimize this problem[91]. In the frame of this work, a comparison between different Al/Al$_2$O$_3$ nanostructures has been done. As the methodology used for all samples was same, we assume that the error is same for every reconstruction and analysis.

4.1.3 Results and discussion

4.1.3.1 SEM images/cross sections

The topography of 1D Al$_2$O$_3$ nanostructures prepared by CVD at different deposition times is shown in SEM images in figure 4.7. Concerning the nanowire diameter, it is observed that it remains constant regardless from the deposition time. Previous analysis demonstrated statistical determinations of 20-30 nm[92]. It is well known that, according to the typical vapour liquid solid (VLS) process, the initially deposited catalyst particle defines the final diameter size of the 1D nanostructure[51]. In the so called "catalyst free process" the dimensions of the wires are also defined by the droplet formed at the beginning of the VLS process[93].

In terms of topography, significant differences are detected as deposition time increase. Figure 4.7a and figure 4.7b show LD-NWs deposited nanostructures in high and low magnification respectively. It

is observed a wide interspace between surface features and the nanowires can be considered as isolated from each other. The coverage of the coating is low and homogeneous and the length of the features is about several nm and not much higher than the diameter size. No connection between features is observed in this case. As deposition time increases so does the nanowire density and the connection between features. The nanowire coverage and the length of the features also increase creating an entangled disordered geometry, which reminds of spaghetti morphology. No significant differences are observed between MD-NWs and HD-NWs in the planar views. In both cases a homogeneous, dense and chaotic topography is observed. It can be estimated that HD-NWs are formed by longer and more entangled nanowires than in case of MD-NWs. This hypothesis will be confirmed with the cross section images and the 3D reconstruction.
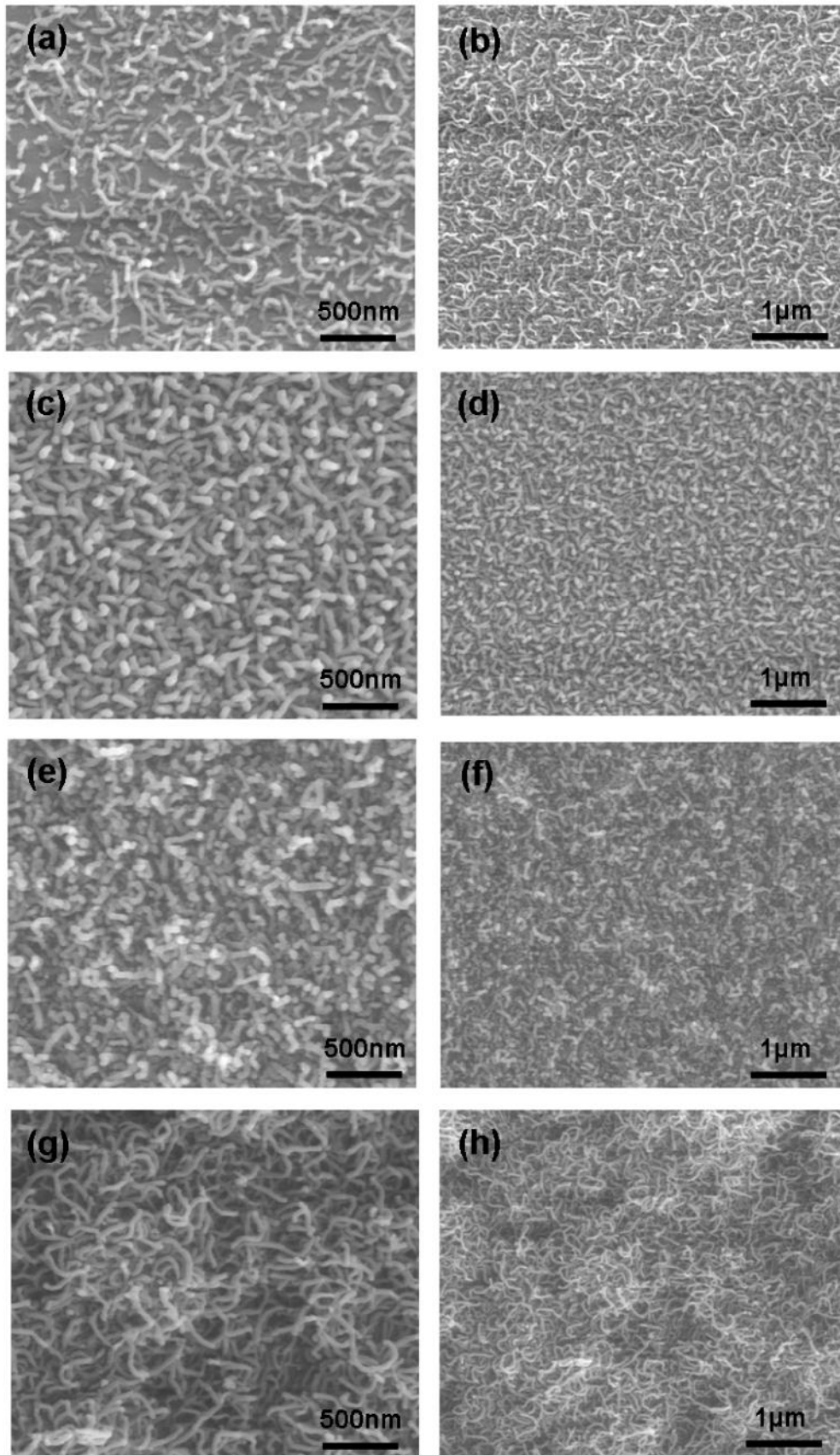
Figure 4.7: SEM images of deposited Al/Al$_2$O$_3$ NWs with high (left) and low magnification (right) of LD-NWs (a, b), MD-NWs (c, d), HD-NWs (e, f) and (g, h) UHD-NWs.

Characteristically, UHD-NWs show a different topography compared to all other deposited nanostructures. Some ball like structures reminding cauliflower morphology are formed at the top of the surface. As it is shown in figure 4.8 the clustered balls have a size between 1-3 µm. Moreover, nanowires are observed as if covering the clusters. It cannot be defined from the planar view if these correspond to tips belonging to the nanowires that started growing in a prior stage, or if they correspond to new grown nanowires on the clusters. This phenomenon was already detected in Eve Sow thesis[94] and it is only observed at very high deposition times. Sow's hypothesis, to explain the phenomenon, was that either the particles have been covered by nanowires or nanowires grow preferentially in spherical shapes. This question will be further discussed when analysing the cross section images within this section.
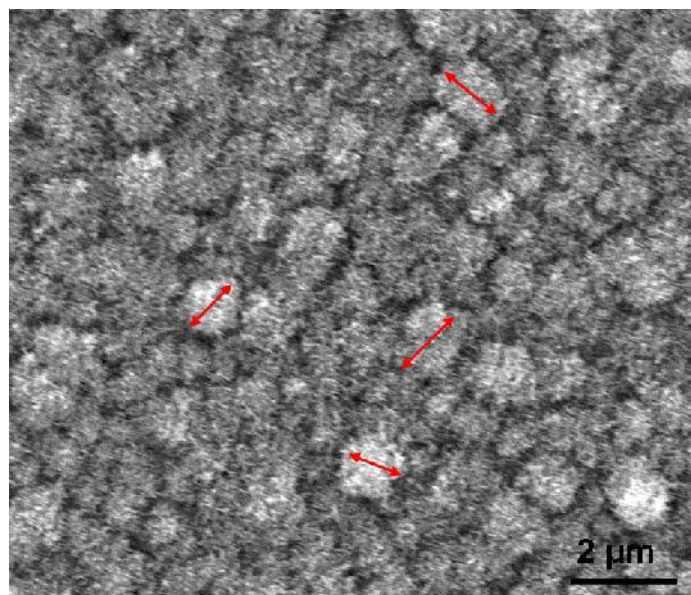
Figure 4.8: SEM images of UHD-NWs with low magnification.

After the milling process with the ion beam, several 2D cross section SEM images were obtained for every deposited 1D Al/Al$_2$O$_3$ structure. These images were used for the posterior 3D reconstruction as well as for thickness and aspect ratio determination.

A first estimation of the coating thickness was obtained with the 2D cross section SEM images. In figure 4.9a, corresponding to low density 1D Al$_2$O$_3$ structures (LD-NWs), it is observed that the vast majority of the features grew up to the same point (~ 100 nm, yellow line), nevertheless, some isolated tips appear at higher positions (yellow circles). All in all, an average thickness of ~ 115 nm was estimated. In figure 4.9b the same phenomenon is observed but in this case the vast majority of the NWs grew up to a slightly higher point (~ 115 nm, yellow line) and consequently the average thickness is higher. Both images, figure 4.9a and figure 4.9b, correspond to different samples of as

deposited LD-NWs. Depending on the sample different average heights were obtained. The reason of this difference is that not all samples are completely identical even same parameters and same device were used. As an example, the heat distribution on the substrate is not totally homogeneous due to the induction technique; therefore there may be a small heat gradient in the graphite susceptor. This may be a result of the inhomogeneous electromagnetic field distribution within the susceptor. It is known that while a solid cylinder is heated by electromagnetic induction, a temperature gradient occurs from the surface to the core of the cylinder[95]. Aktas imaged in his doctoral thesis such local temperature gradients on the substrate with a thermal camera. The local temperature gradients on the surface seem to be the reason for random and highly chaotic arrangement of nanowires[92].
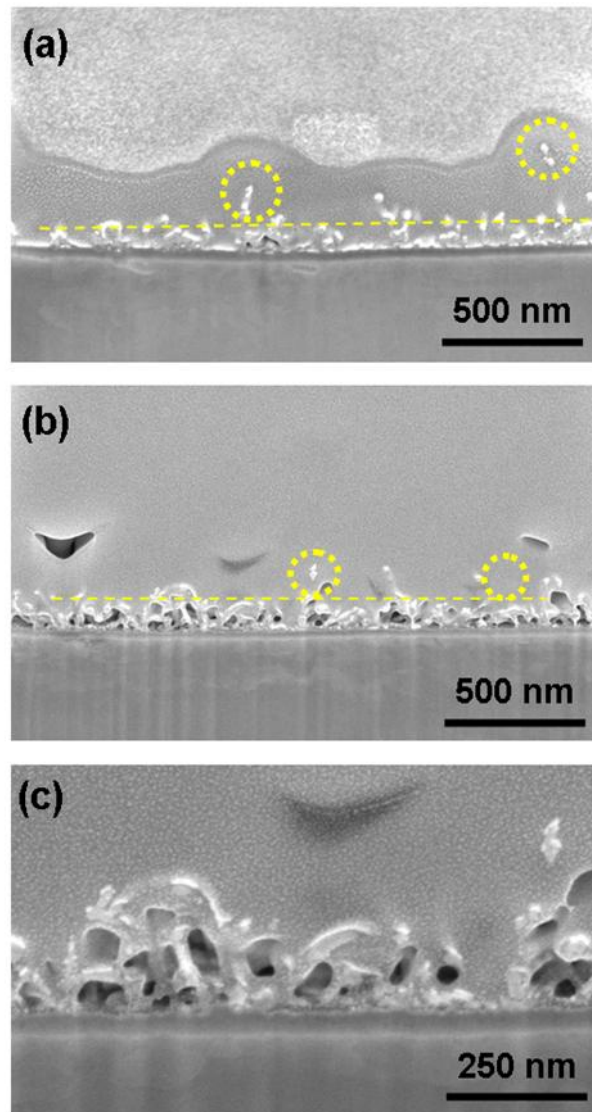
Figure 4.9: Cross section SEM images of Al/Al$_2$O$_3$ NWs of two different samples deposited according to LD-NWs parameters.

Figure 4.9c shows how isolated nanowires can be followed one by one from bottom to top. Almost no connection between the nanowires is observed. Veith et al. showed previously with the support of TEM techinque that these 1D Al$_2$O$_3$ nanostructures actually are composed of an Al core and amorphous Al$_2$O$_3$ shell structure forming co-axial nanowires[50]. The core-shell detail can not be here seen due to magnification.

In case of middle density 1D Al/Al$_2$O$_3$ nanostructures (MD-NWs) different thicknesses were observed depending on the sample in a range between 400 and 500 nm (figure 4.11a and 4.11b). Figure 4.11c shows how similarly than in the previous cases some isolated tips appear at the top of the surface (yellow circles). The nanowires are highly entangled at first stage but less entangled at the surface. Still the single nanowire can be followed one by one but it is more difficult than in LD-NWs because some of the nanowires contact with each other. It cannot be appreciated on the SEM images obtained from the FIB technique the nature of these contacts due to the resolution. For such analysis a technique with more resolution is needed. Sow[94] and Aktas[92] made a deep analysis of the nanowire growth and reported this phenomenon in their doctoral thesis with the support of TEM and HR-TEM techniques. Sow detected some highly crystalline aluminium heads at the top of some nanowires using TEM and XRD techniques. She assumed that those heads were starting points for further nanowires growth. To explain this phenomenon she investigated growth islands at the surface of the nanowire head, the new nanowire can have its soured from these growth island. The branching could come from migration and agglutination of the growth islands. She observed agglomeration of nanoparticles on the nanowire surface, which could be the source of new nanowires growth. She assumed that many growth islands form at the same time (or in a very short time) on the head of the surface; many nanowires could then grow at the same time (or in a very short time). This agglomeration leads to a minimization of the system energy so that this phenomenon tends to be favoured. Her hypothesis could explain the contact of at least one nanowire to the substrate, as well as the branching and the fact that some nanowires display a head and others do not.

Aktas also studied this phenomenon in his doctoral thesis[92]. He explained that the nucleation and growth continue all the time during evaporation since the AlO vapour phase is generated continuously. He supposed that those gaseous species may condensate either on the side surfaces or tips of the former nanowires. He believed that tips containing Al seeds (heads) act as preferred nucleation sites according to the growth mechanism of the nanowires. He suggested that new nuclei may form on the nanowire tips with different crystalline orientations during the growth. In his point of view, this re-nucleation results in the formation of junctions where new branches grow.

Figure 4.10 shows a conceptual schema where the main differences between the concepts "branching" and "contact" are observed. In case of branching, new nanowires grow from an original nanowire while, in case of contact, the nanowires grow independently from each other and contact with each other at some point. It is believed that both phenomenons take place during the CVD deposition.
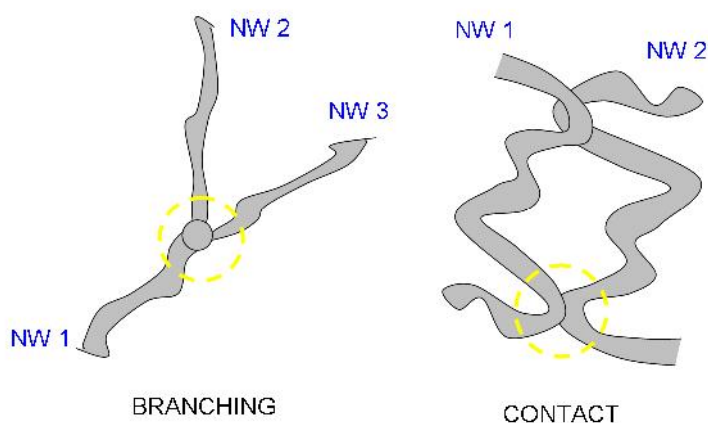
Figure 4.10: Conceptual schema: differences between branching and contact.

The fact that junctions are formed, either as a result of nanowire branching or as a result of nanowire contacts, reveals the existence of connectivity between them. In the frame of this work the connectivity between nanowires is an important parameter, which is believed to influence the properties of the deposited coatings. In the research community, there is a common agreement that bone grafts should have an interconnected porous structure to allow tissue regeneration, vascularization and cell ingrowth[96-101]. Porosity as well as connectivity of the Al/Al$_2$O$_3$ are further analysed within this chapter.
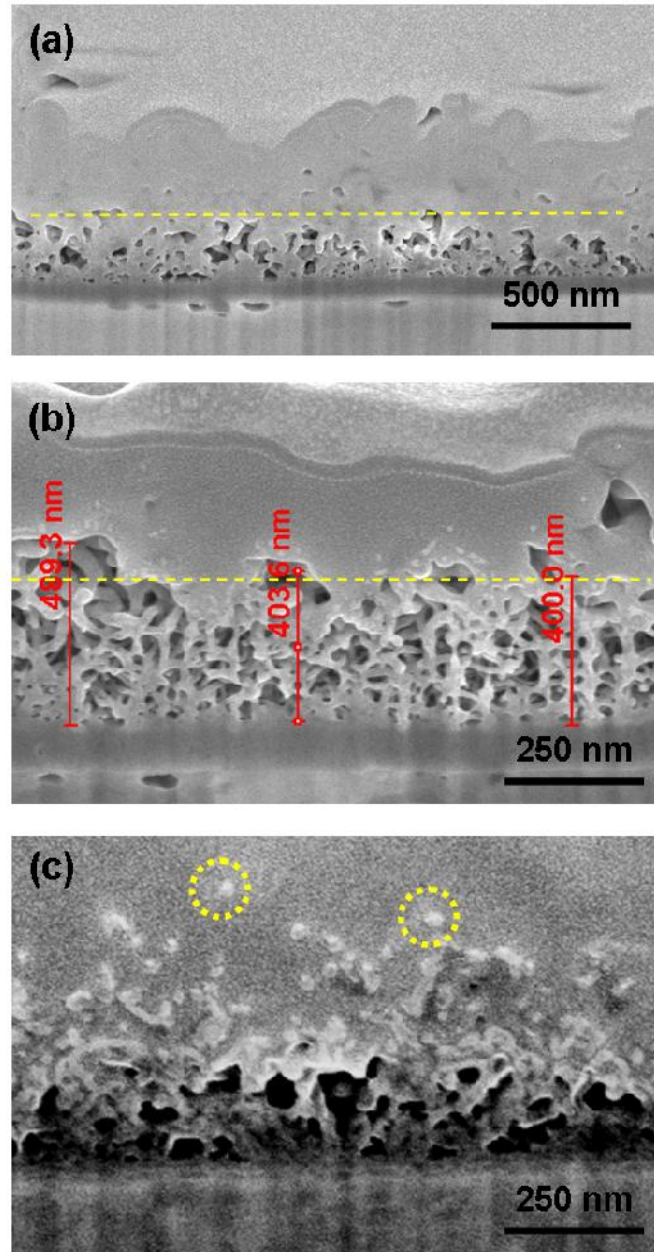
Figure 4.11: Cross section SEM images of Al/Al$_2$O$_3$ NWs of three different samples deposited according to MD-NWs parameters.

Figure 4.12 depicted cross section SEM images corresponding to high density deposited 1D Al$_2$O$_3$ nanostructures (HD-NWs). In comparison with LD-NWs and MD-NWs an average thicker coating is observed. Differently than in the two previous cases less isolated tips are seen. The nanostructures start entangling at first stages and keep entangled till higher points. In this case it is almost impossible to follow single nanowires one by one due to high connectivity and entangling.
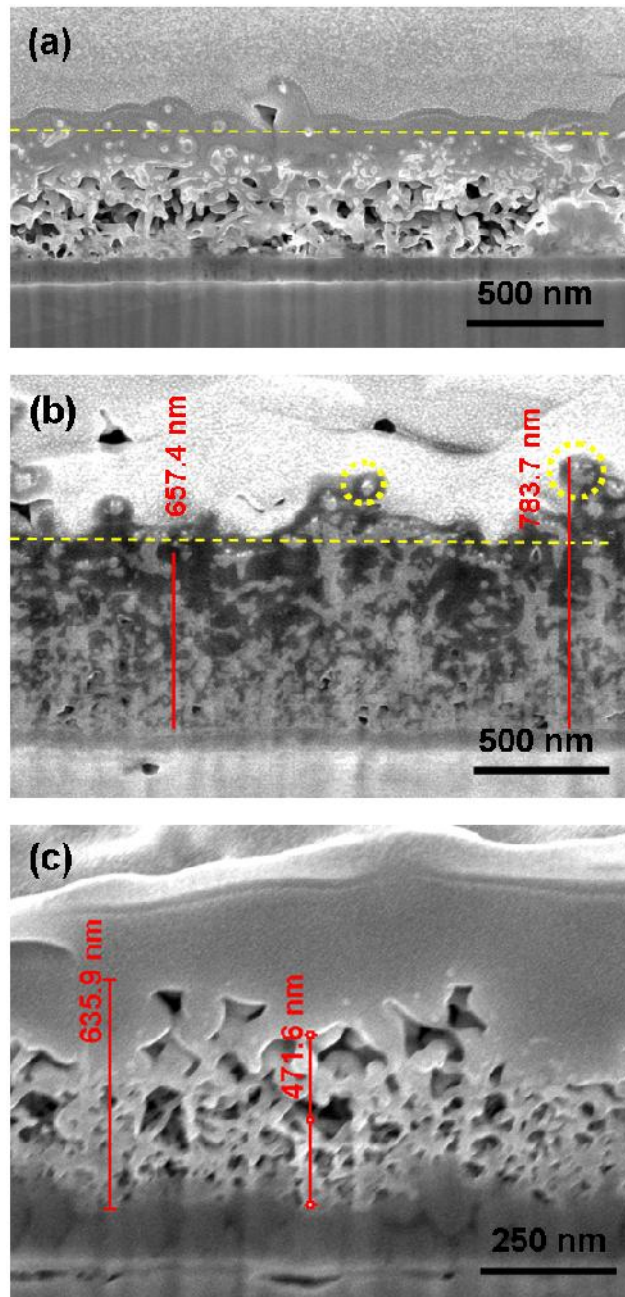
Figure 4.12: Cross section SEM images of Al/Al$_2$O$_3$ NWs of three different samples deposited according to HD-NWs parameters.

In terms of topography figure 4.13 shows an irregular profile formed of hills. A few single tips are observed in this case at the top around the hills. The observed hills correspond to the 1-3 µm balls detected previously on the SEM images. In this case extremely entangled geometry is observed consequence of very high connectivity between nanowires. This confirms that on the top of the ultra high deposited 1D Al$_2$O$_3$ nanostructures (UHD-NWs) micro sized ball shaped clusters are formed. Nevertheless, it is not clearly understood how these clusters are formed with a cross section image. Sow performed a deep structural study of the Al/Al$_2$O$_3$ nanowires and she reported, with the support

of TEM analysis, that the observed agglomerations of clusters on the coating surface could be the source of further nanowires growth[94]. This agglomerations lead to minimization of the system energy so that this phenomenon tends to be favoured.
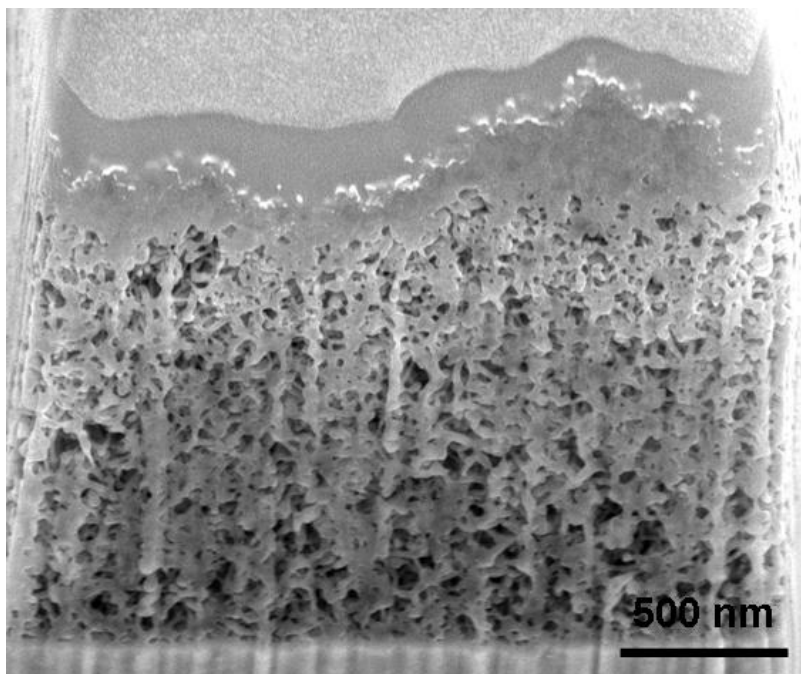
Figure 4.13: Cross section SEM images of Al/Al$_2$O$_3$ deposited according to UHD-NWs parameters.

For thickness determination a tolerance factor of 50 nm was assumed in all cases. Table 4.1 shows that the less dense deposited coating (LD-NWs) exhibits a thickness between 125 and 225 nm. MD-NWs exhibit thicknesses between 400 and 500 nm and for the HD-NWs the thickness range was found between 700 and 800 nm. Those samples having a thickness above 800 nm are defined as UHD-NWs. After 3D reconstruction of all sample types an analysis of the 2D porosity and the NW coverage through the thickness of the substrates is performed within this chapter. This analysis supports and corroborates the present estimation of the thickness.

Table 4.1: Thickness estimation (cross section SEM images)

Sample type	Average thickness range (nm)
LD-NWs	175 ± 50 nm
MD-NWs	450 ± 50 nm
HD-NWs	750 ± 50 nm
UHD-NWs	> 800 nm

Figure 4.14 shows the relationship between thickness and deposition time. Thickness increases as the deposition time is prolonged. The non-fitting of the HD-NWs and the UHD-NWs in the linear tendency may explain the cluster formation shown previously. It is clear that UHD-NWs belong to a different category than LD-NWs, MD-NWs and HD-NWs. HD-NWs could be considered as a category in between the spaghetti-like nanostructure, which presents isolated tips at the top and less connection between nanowires, and those coatings showing a cauliflower-like structure at the top of the layer in which more connectivity and cluster formation is assumed.
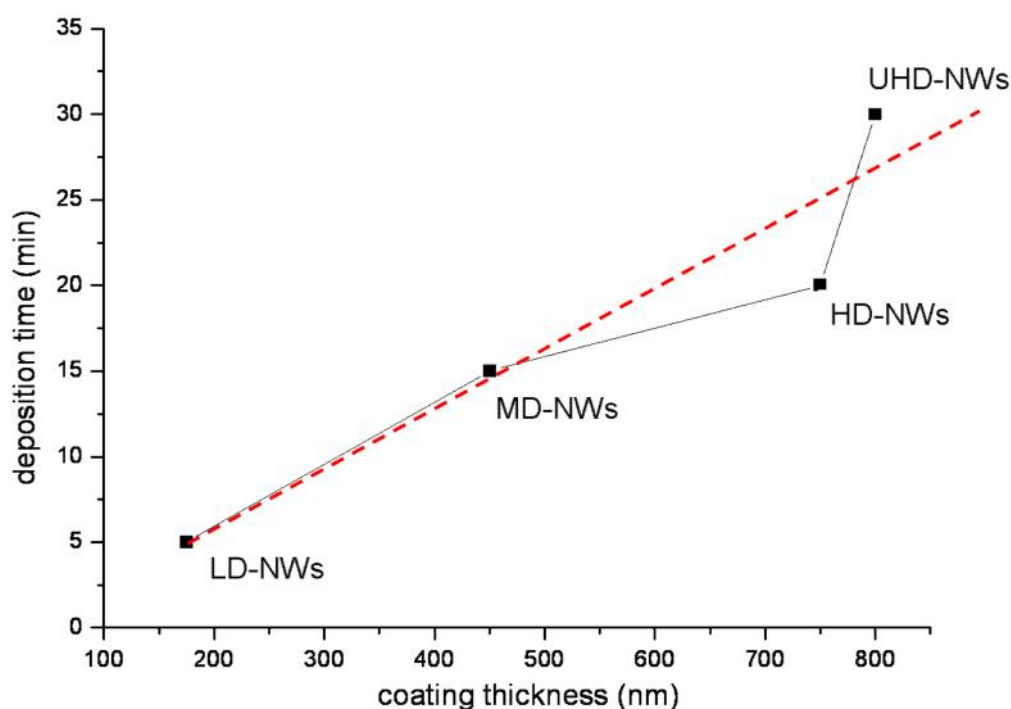
Figure 4.14: Coating thickness of the Al/Al$_2$O$_3$ deposited nanostructures versus deposition time.

As it is observed in fig 4.13, some charge appears in the UHD-NWs cross section SEM images (white area). The sample was sputtered, as usual, with gold in order to provide electrical conductivity and avoid charges during the imaging process. Once inside the chamber, also Pt was deposited *in situ* on the ROI. Nevertheless, in this case still some charge was observed due to the thickness of the sample. The observed charge impedes obtaining sharp 2D SEM images. An additional problem is that it is not possible to differentiate which nanowires are on the first plane and which ones are on a second plane. Therefore, after several attempts, the correct reconstruction of the ROI for the UHD-NWs samples was not successful and consequently no 3D model is available for this sample type. SEM images from top could be obtained and the 2D cross sectional SEM images were used to estimate the thickness and the aspect ratio of this sample.

In order to avoid charge and to obtain sharper images other authors used infiltration techniques [102]. Such techniques consists of infiltration of the porous structure with a low-viscous material, typically a resin or a polymer, at the liquid state. After solidification, this material acts as a supporter for the whole structure. As a result, higher contrast between the sample and the infiltrated material occurs during the imaging process. In our case, silver infiltration was used. Nevertheless, no good contrast was observed between the NWs and the infiltrated silver and no better images were obtained. No further attempts have been performed using this technique.

4.1.3.2 Reconstruction of 3D models

After aligning the 2D SEM images obtained from FIB-nanotomography, cropping representative volumes, segmenting the desired features and recompiling, a reconstructed 3D model is presented for LD-NWs, MD-NWs, and HD-NWs in figure 4.15, figure 4.16 and figure 4.17 respectively. Cross sectional and top views are also shown. The 3D reconstructions reveal more clearly the topography of every structure and provide information for a more precise definition.
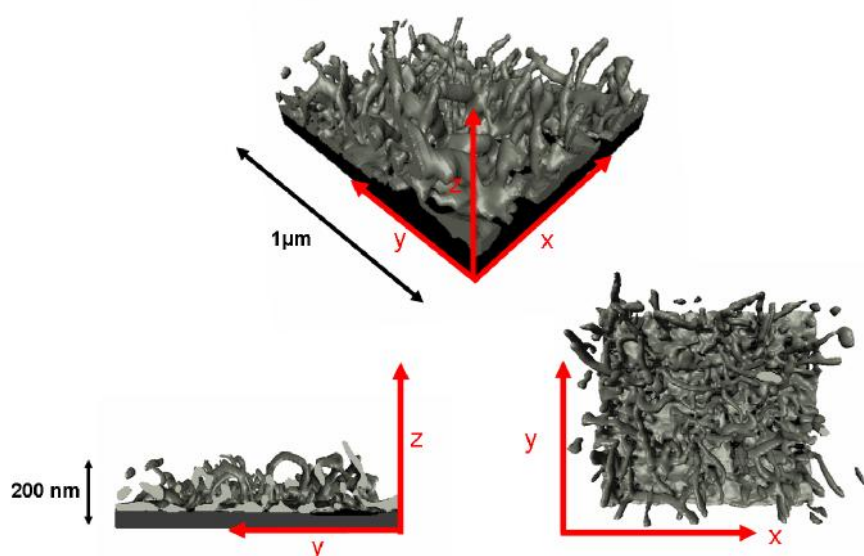
Figure 4.15: 3D reconstructed models of the low density Al/Al$_2$O$_3$ NWs (LD-NWS). Perspective view (top) cross sectional view (left) and top view (right).

The 3D reconstruction of the LD-NWs structure confirmed what already was observed in SEM images and cross sections. This structure consists of single nanowires with low connectivity between them. The distance between features is quite wide and some voids are observed between nanowires. The detected tips which were observed in the cross sectional SEM images correspond mostly to the tips

of some nanowires although some nano "loops" have also been detected. These nano "loops" have been previously shown in Aktas work in SEM images[92]. Concerning the structure conformed by MD-NWs, a clear increase of thickness is observed as expected. Figure 4.16 clearly shows a highly entangled geometry with isolated nanowires and some "loops" on top of the coating. In case of HD-NWs an increase of thickness is again detected. As a peculiarity, fewer loops are observed in this case on top of the surface. Some connected nanowires are observed on top. In all structures exists a porous media with a complex form of disorder. The porosity of the nanostructures will be analysed within this chapter in 2D as well as in 3D.
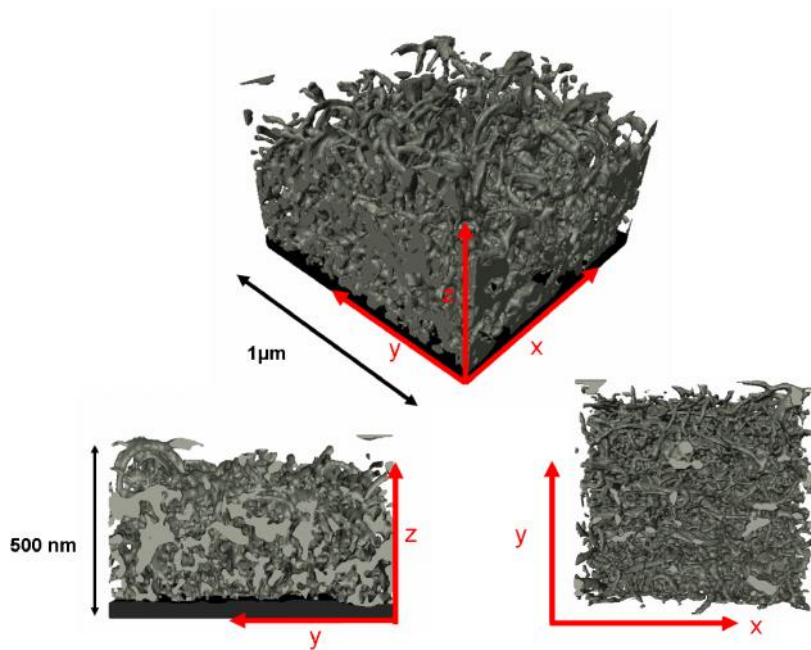
Figure 4.16: 3D reconstructed models of the middle density Al/Al$_2$O$_3$ NWs (MD-NWS). Perspective view (top) cross sectional view (left) and top view (right).

Figure 4.17: 3D reconstructed models of the high density Al/Al$_2$O$_3$ NWs (HD-NWS). Perspective view (top), cross sectional view (left) and top view (right).

4.1.3.3 Analysis of reconstructed 3D models

4.1.3.3.1 2D analysis: NW coverage, 2D porosity and aspect ratio

Analysis of the NW coverage and 2D porosity along z and y directions:

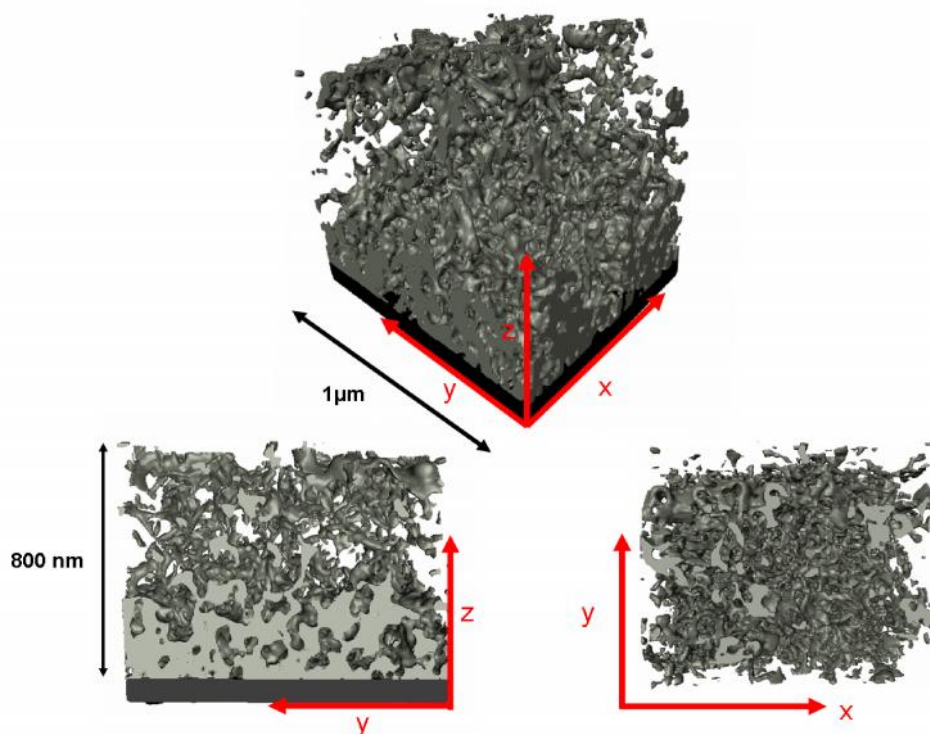For a better understanding of the 1D feature distribution through the sample, 2D analyses have been performed. Every 3D reconstructed block has been sliced through the z and y direction obtaining as a result a set of binary images for every direction. In case of the y direction, the slices resulting from the FIB-nanotomography were used directly. A binary image is a digital image that has only two possible values for each pixel[103] where each pixel is stored as a single bit (0 or 1). Black is the foreground, in our case Al/Al$_2$O$_3$ NWs, and white corresponds to the background. The binary images have been processed with the Image J software and the black/white area percentages, corresponding to the NWs/void ratio, have been calculated and represented in graphs. The aim of this 2D analysis is to understand how the nanostructure evolves along the thickness and the width of the Al/Al$_2$O$_3$ coatings and analyse the differences depending on the direction. In the frame of this work, this information supports the better understanding of the cell surface interaction. It is well known that the first event after implantation is the adsorption of blood proteins on the surface of the implant[104]. In this context, in the cell culture experiments presented in chapter 5, fibroblast and

osteoblast cells are cultured on top of the coating, therefore it is important, not only to know which are the available free spaces between the features at top of the coating, but also to understand how these interspaces evolve through the coating. In this regard, the concept of 2D porosity is introduced in this section.

Figures 4.18, 4.19 and 4.20 show three binary images parallel to the plane x-y for LD-NWs, MD-NWs and HD-NWs respectively. The binary images correspond to slices, which were taken from bottom to top of the sample along the z-direction. Image n°1 corresponds to the bottom, image n°2 illustrates a slice equidistant to bottom and top, and image n°3 corresponds to the top. In case of LD-NWs, figure 4.18 shows that the foreground decreases in z-direction. In image nº1 several black areas are observed (NWs) while in image nº3 only a few black dots very wide from each other are depicted. These small dots correspond to nanowire tips or loops. Isolated features are assumed in this case.
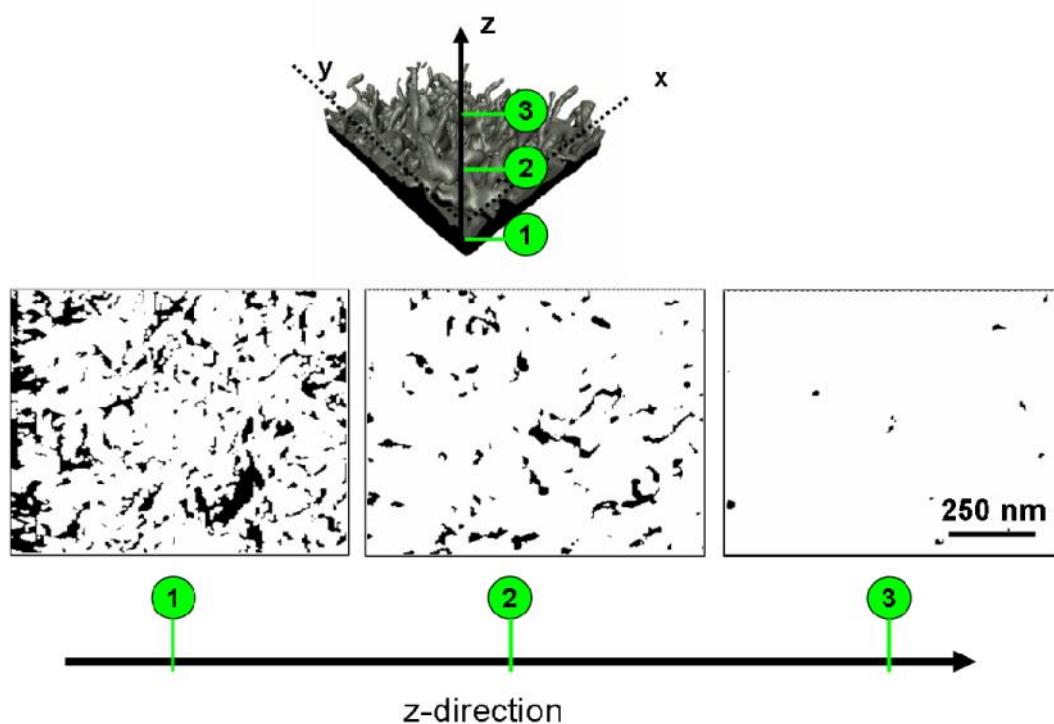
Figure 4.18: Binary images along the z-direction for LD-NWs.

The binary images with red frame from figure 4.19 correspond to three slices of the middle density 1D Al$_2$O$_3$ structures (MD-NWs). It is observed that the fraction of area corresponding to the Al/Al$_2$O$_3$NWs (black area) decreases in z-direction as shown previously for LD-NWs. Compared with LD-NWs, a bigger NW area is observed in image nº2 which indicates higher connectivity between the 1D Al$_2$O$_3$ deposited nanostructures. Similarly than in figure 4.18, the black areas observed in image

47

n°3 revealed the presence of tips or loops. The distance between features in image n°3 is narrower than that one for LD-NWs.
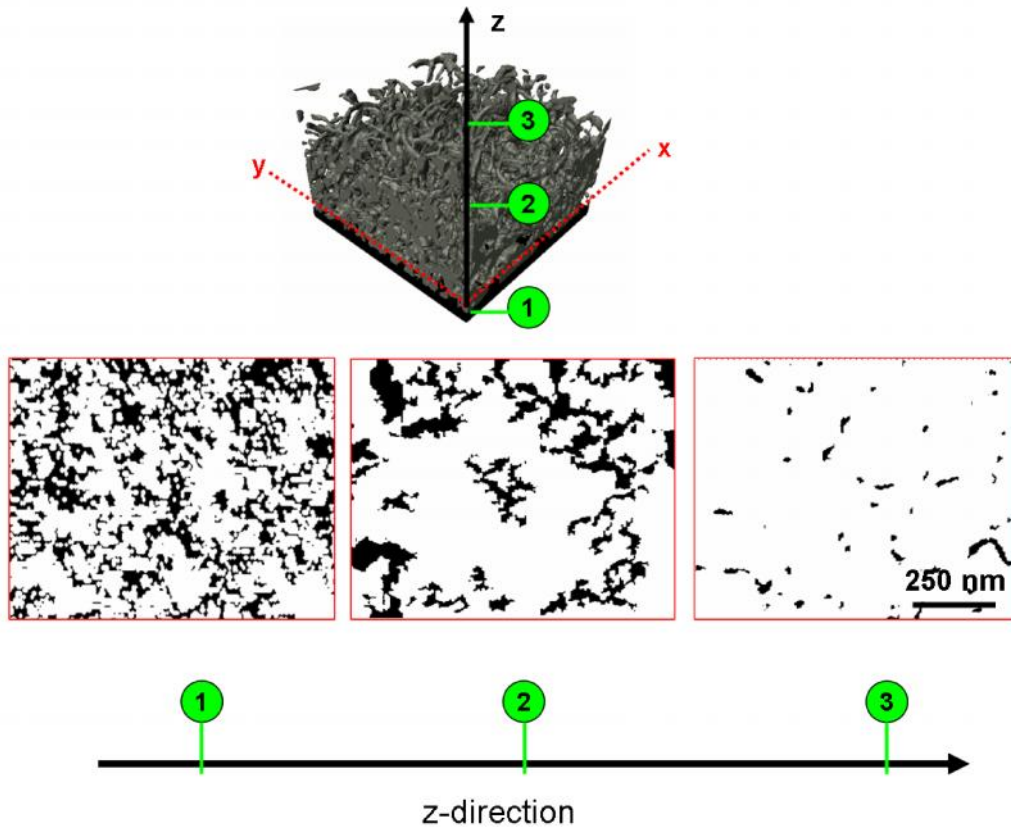
Figure 4.19: Binary images along the z-direction for MD-NWs.

Figure 4.20 shows the evolution of HD-NWs in z-direction. As observed in LD-NWs and MD-NWs, a decrease of the foreground takes place in z-direction. Characteristically, image n°3 shows fewer tips than in prior cases. The absence of tips indicates a denser and more connected structure at the top of the HD-NWs coating. The interspacing between features is less in this case.

All in all, the binary images parallel to x-y plane reveal that in all cases exists a denser layer on the first nanometres of the coating, which probably corresponds to the first deposition minutes. A more extended nanostructure with more or less tips, depending on the deposition time, is observed at the top of the coating.
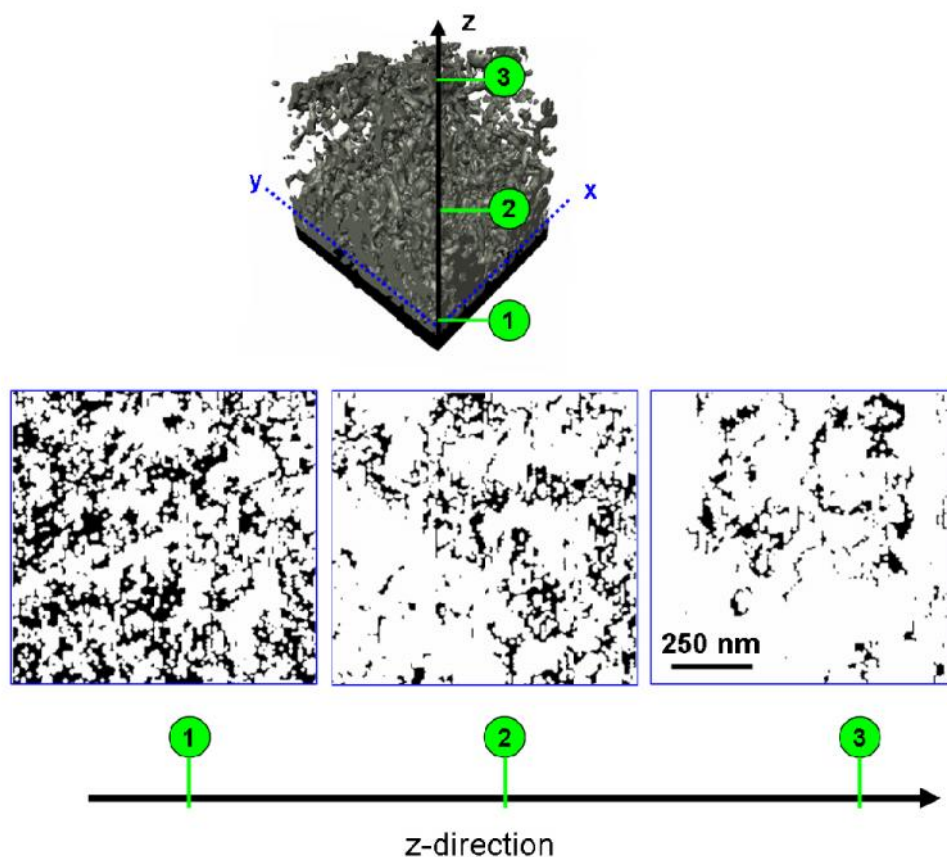
Figure 4.20: Binary images along the z-direction for HD-NWs.

With the percentages obtained from the binary images two graphs have been plotted. Figure 4.21 shows the evolution of the NW coverage (% NWs) through the thickness of the coating in z-direction and figure 4.22 shows the void % along same direction, which is here defined as 2D porosity (%). Generally speaking, porosity is defined as the fraction of the total volume that is taken by the pore (void) space. Taking into account that in this section we are working with 2D data, we used areas instead of volumes in order to obtain the void %.

Figure 4.21 shows that the maximum NW coverage is around 30 % and this is found mainly at the first nanometres of the deposited coating. This amount decreases down to almost 0 % at top of the deposited coating. Nevertheless, some differences are observed depending on the sample type: For LD-NWs (black line) an almost linear decrease is observed from 30 % to 0 % through z-direction. Previously an average thickness of 175 ± 50 nm has been found from cross-section analysis (Figure 4.9) for this sample type. In figure 4.21 is observed that below this point (yellow dot) the NW coverage is less than 5 %. Below this value only single tips or loops have been assumed. In this context, it makes sense to fix the thickness point in a region were the % of the material of interest is found in less than 5 %, therefore the thickness value presented before in this chapter is confirmed.

Such criteria will be also applied for MD-NWs and HD-NWs. The red line plotted the evolution through z-direction for the MD-NWs. From 0 to 100 nm a linear decrease of the NW coverage is observed from 30 % to 18 %. From 100 to 300 nm a non-linear behaviour is observed. The nanowire % increases and decreases indistinctly and maintains a value around 20 %. This tendency reflects the fact that the 1D Al/Al$_2$O$_3$ nanostructures start connecting to each other after a certain deposited thickness. From 300 to 400 nm the nanowire % decreases from 30 % to 10 % and from 400 to 600 nm the coverage decreases from 10 % to almost 0 %. The yellow dot at 450 nm indicates the average thickness, which was found from cross-section analysis previously. Similarly than in the previous case below 5 % only single tips or loops have been observed. Finally, the blue line plotted the evolution through the thickness for the HD-NWs. As in the two previous cases, exists a decrease of the NW coverage at the first nanometre range, concretely; from 0 to 200 nm the nanowire % decreases from 30 % to 20 %. From 200 to 600 nm the NW coverage increases and decreases maintaining its values between 20 % and 30 %. As in MD-NWs high connectivity between features is deduced from this range. From 600 nm to 800 the NW % value decreases down to 5 %. Above this point the NW coverage is maintained between 5 % and 15 % till the top of the coating. The tendency of this last range confirms the presence of fewer tips in this nanostructure. The yellow dot at 800 nm indicates the average thickness that was found from cross-section analysis within this section. Differently than in the previous cases below 5 % not only single tips have been observed.
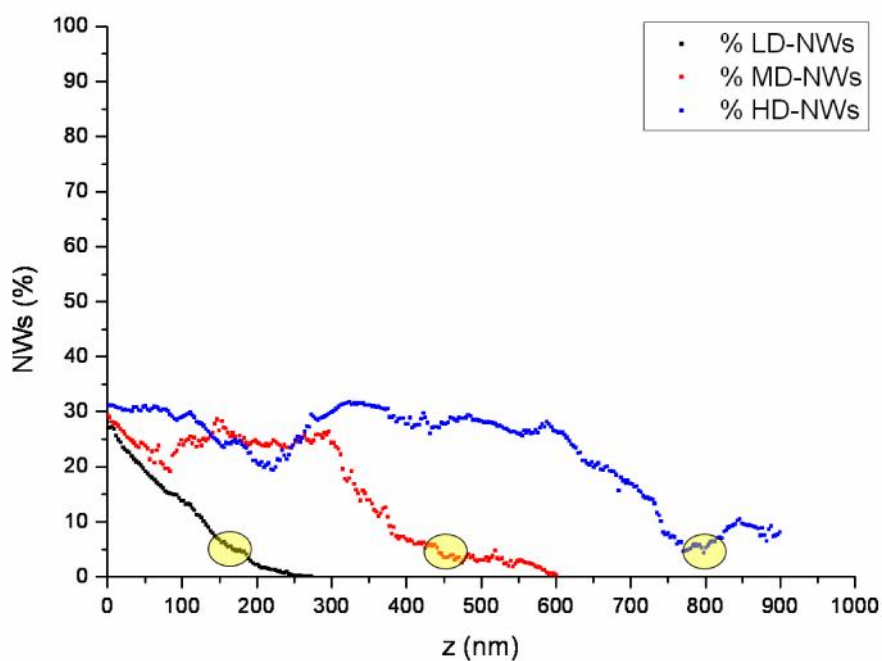
Figure 4.21: NW coverage (% NWs) along z-direction.

In figure 4.22 a graphic plots the 2D porosity % through z-direction. Shape and diameter of the pore are not easy to estimate due to the complexity and highly entangled nanostructure conformed by the 1D Al/Al$_2$O$_3$ NWs, instead, the evolution of the 2D porosity through the thickness and width has been analysed for a better understanding of the distribution of the voids along every nanostructure.

The percentage values are calculated from the same binary images used for NW coverage calculation. Taking into account that only NWs or void are present in the sample, the 2D porosity tendency is reverse to the NW coverage (%) shown in the graphs of figure 4.22.

It is observed that the minimum 2D porosity value is around 70 % mainly at the first nanometres of the coatings and reaches a maximum of almost 100 %. In case of LD-NWs (black line) the 2D porosity increases linearly from 70 to almost 100 %. It reaches a maximum value of almost 100 % at the top of the coating where the tips and loops were observed. For the MD-NWs (red line) the 2D porosity also increases up to almost 100 %. While LD-NWs showed a linear increase, MD-NWs showed an irregular increase due to the higher connectivity between NWs. From 100 nm to 300 nm the % 2D porosity increases and decreases in values ranging from 70 % to 80 %. Till this point a ground layer is assumed. Above this point the 2D porosity increases reaching maximum values. Similarly than observed in MD-NWs, HD-NWs showed an irregular increase of the 2D porosity values. From 0 to 200 nm the 2D porosity increases from 70 % to 80 %. From 200 to 500 nm there is a high connectivity between the nanowires and an irregular curve is observed. As in MD-NWs, a ground layer is assumed up to this point. Above 500 nm the 2D porosity % increases from 70 % to almost 100 %.

In case of MD-NWs and HD-NWs a ground layer has been observed during the first nanometres of the coating. After this ground layer less connection between nanowires is assumed. This point has been found at almost a factor 2 between both coatings. Such behaviour has not been observed in case of LD-NWs.
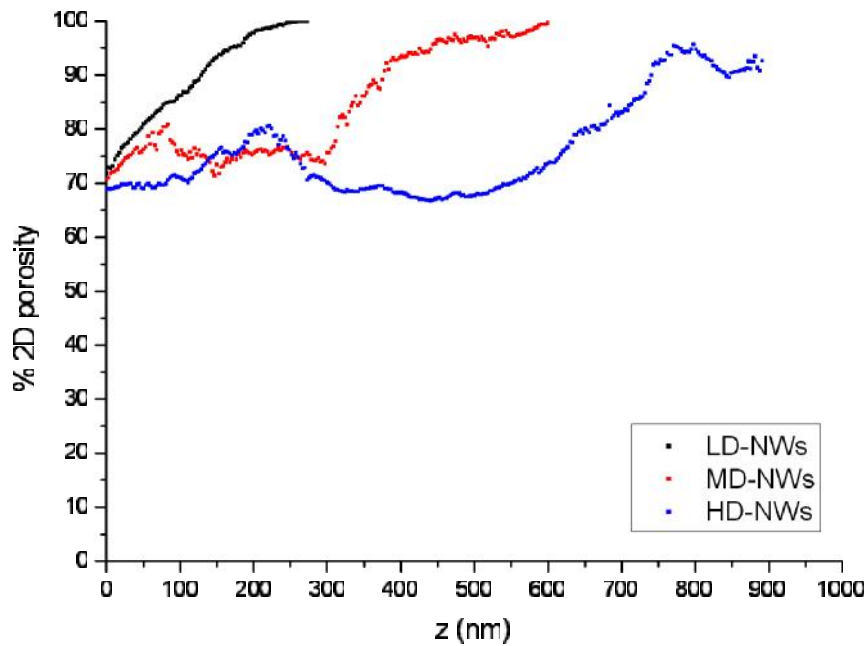
Figure 4.22: 2D porosity (%) along z-direction.

Same investigations have been performed along the y-direction. Figures 4.23, 4.24 and 4.25 show three binary images parallel to the plane x-z for LD-NWs, MD-NWs and HD-NWs respectively. The binary images correspond to the dataset of SEM images obtained from the FIB nanotomography. Image n° 1 corresponds to the first sample wall, image n° 2 illustrates a slice equidistant to the two walls of the sample and image n° 3 corresponds to last sample wall.

While in z-direction big differences were revealed through the coating, no relevant differences have been observed through the width of the sample. Figure 4.23 shows three binary images for LD-NWs. No remarkable differences are observed between image n° 1, 2 and 3. The foreground % remains constant along y-direction. In all images single and isolated NWs are observed. In all images some points are seen at the top of the layer corresponding to NW tips or to NW loops. The three images show a low connectivity between features.
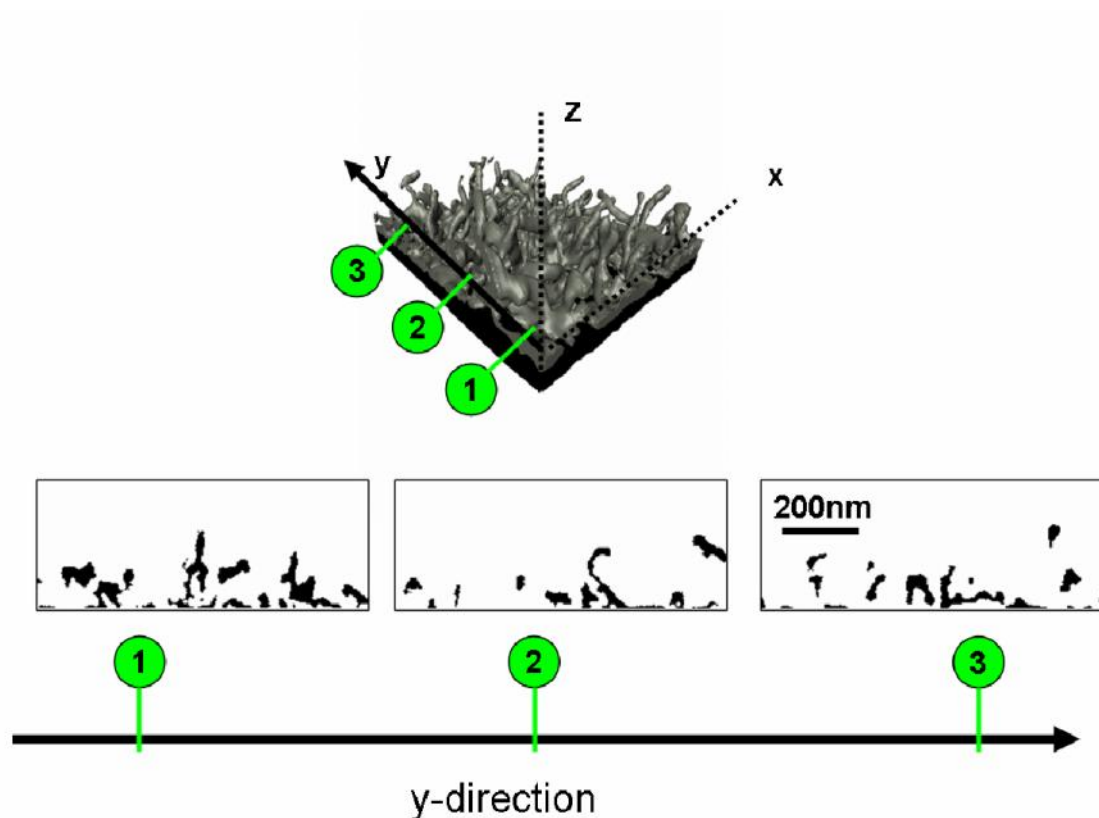
Figure 4.23: Binary images along the y-direction for LD-NWs.

Concerning MD-NWs, the 3 images from figure 4.24 reveal that as in LD-NWs, the NW coverage remains constant along the y-direction. Single NWs are not detected; otherwise high connectivity between features is deduced. Some black isolated areas are observed at top of the images that belong to NW tips or NW loops. For the high density 1D Al$_2$O$_3$ nanostructures also the ratio NW/void remains constant along the y-direction. As in MD-NWs, no single NWs are observed and a high connectivity is assumed.
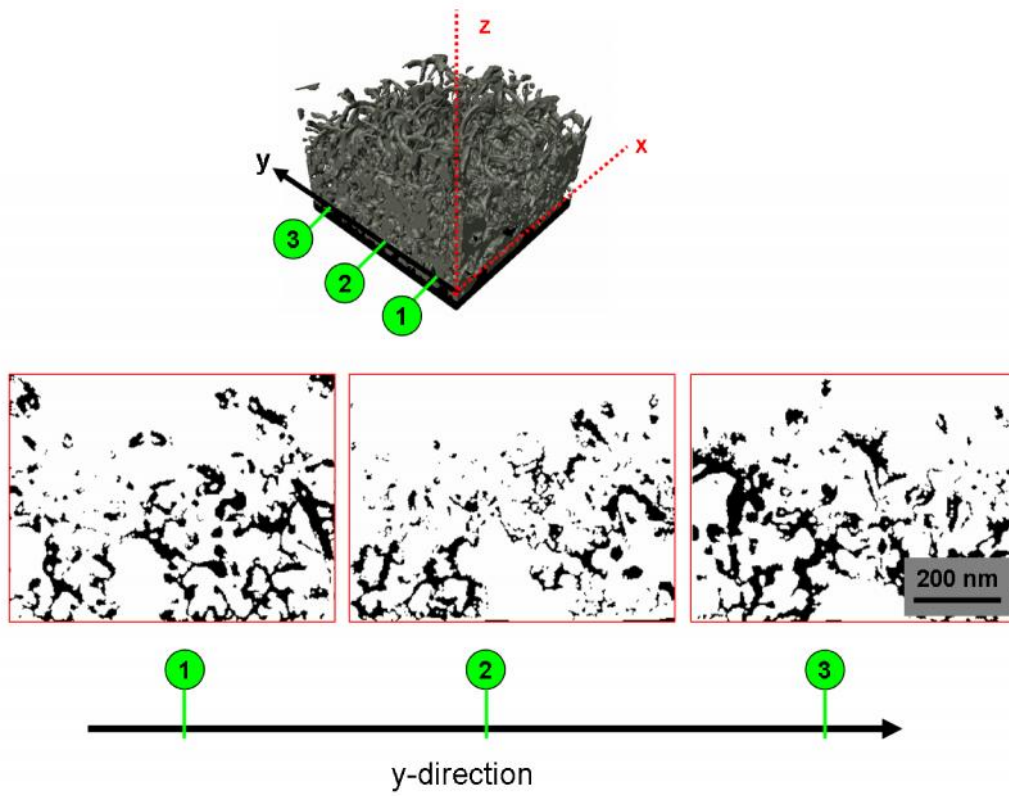
Figure 4.24: Binary images along the y-direction for MD-NWs.
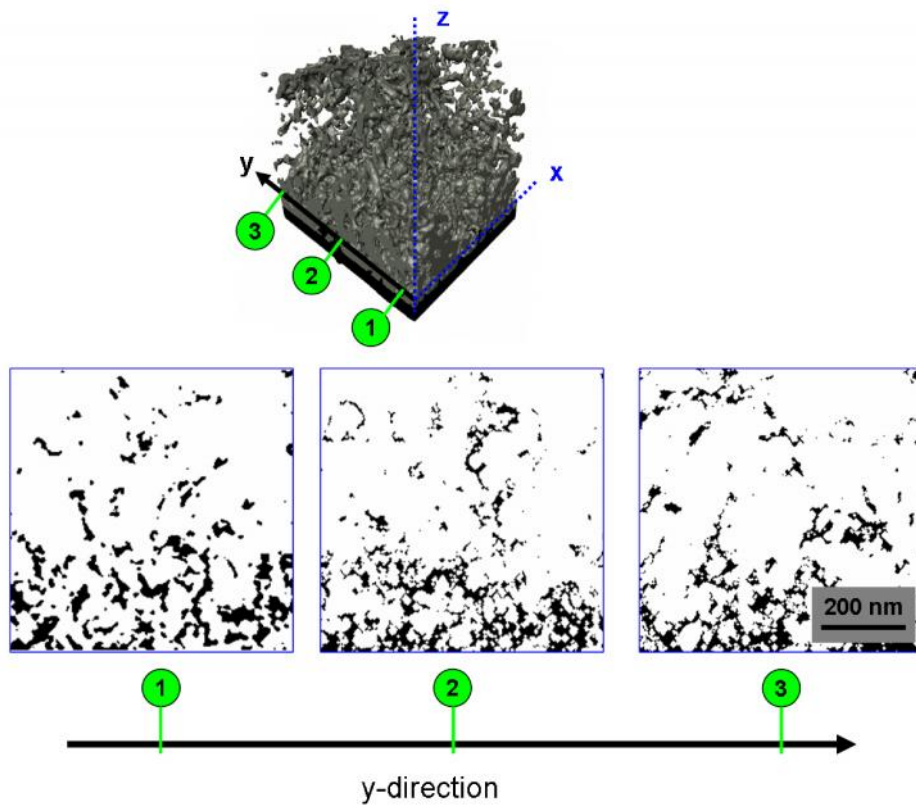
Figure 4.25: Binary images along the y-direction for HD-NWs.

54

Figure 4.26 represents how the NW coverage evolves along the y-direction. NW coverage in a range between 5 and 20 % is observed. LD-NWs showed less coverage than MD-NWs and HD-NWs. The NW percentage in this case increases and decreases around 5 % and 10 %. For MD-NWs the NW coverage fluctuates between 10 and 15 % and for HD-NWs the vast majority of the values are found in a range between 15 % and 20 %. As it was already observed in the binary images, the tendencies of the graphic confirmed that the NW coverage remains constant along the y-direction.
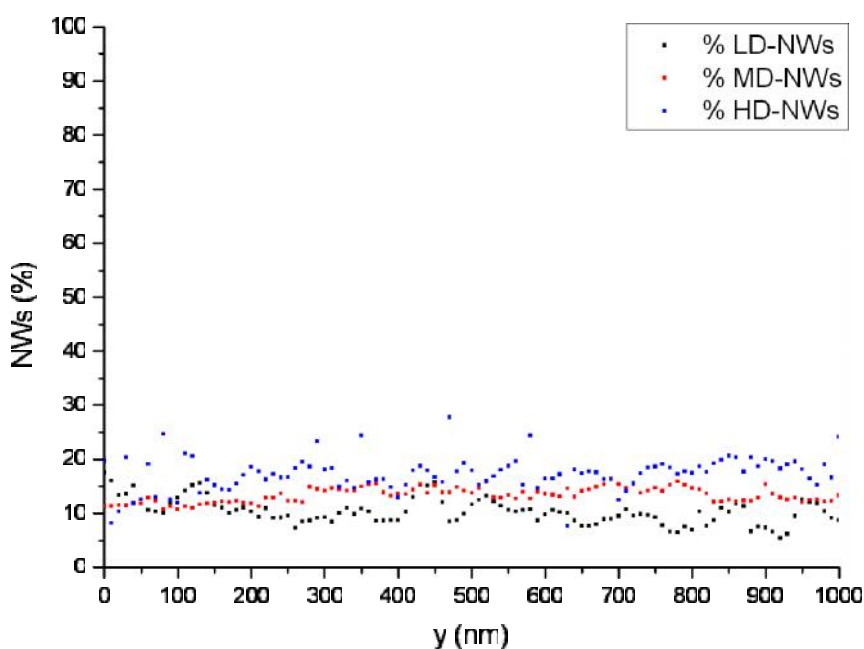
Figure 4.26: NW coverage (% NWs) along y-direction.

Concerning 2D porosity along y-direction it remains constant whereas remarkable differences were observed along the z-direction. The 2D porosity fluctuates between values of 75 % and 95 %. Minimum 2D porosity values are observed for HD-NWs (blue line) and the maximum values for LD-NWs (black line).
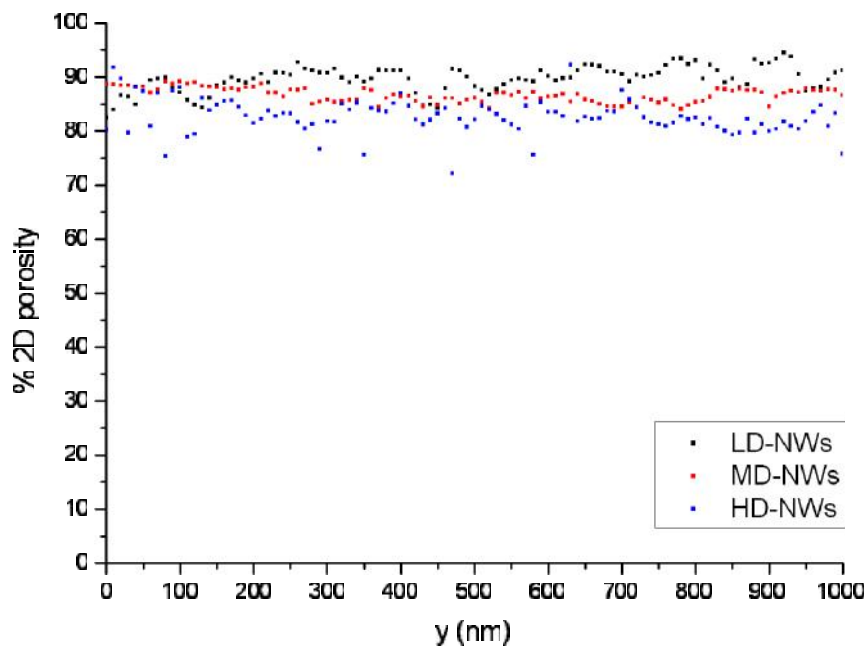
Figure 4.27: 2D porosity (%) along the y-direction.

To sum up:

→ The **NW coverage and the 2D porosity remain constant through the width of all coatings whereas remarkable differences have been observed for both parameters through the thickness of the sample. In this regard, it could be considered that the deposited Al/Al$_2$O$_3$ coatings are formed by multi nanoporous layers, the nanoporosity of which is constant**. For the biological interpretation in chapter 5, it is important to take into account that all **coatings showed higher porosity at the top than at the bottom of the coating**. Previous studies indicated that nanocomposite materials with multi nanoporous layers have higher biocompatibilities[105-108]. The length (x-direction) of the sample has been not analysed. Taking into account the direction of the deposition during the coating (vertical chamber, z-direction) it is assumed that x-direction presents same characteristics as the width (y-direction).

4.1.3.3.2 Analysis of the aspect ratio

The aspect ratio is defined as the length of the major axis divided by the width of the minor axis. Thus, spheres have an aspect ratio of 1. In our case, the aspect ratio was calculated by dividing the length of every 1D nanostructure by its diameter. The length of the nanowires was calculated statistically from several cuts performed with FIB technique.

Murphy et al. defined 1D nanostructures with aspect ratio greater than 20 as nanowires[109]. According to this classification, nanostructures with an aspect ratio between 1 and 20 are defined as nanorods. While LD-NWs nanostructures can be considered as nanorods, the rest of nanostructures can be considered as high-aspect ratio NWs. We observed a significant increase in aspect ratio as deposition time and nanowire density increases (Figure 4.28). The main reason for this increase in the aspect ratio is the highly entangled geometry of the deposited 1D nanostructure. While the length of the nanowires increases (L$_{LD-NWs}$ < L$_{MD-NWs}$ << L$_{HD-NWs}$ <<< L$_{UHD-NWs}$) their diameter remains constant ($\varnothing_{LD-NWs}$ = $\varnothing_{MD-NWs}$ = $\varnothing_{HD-NWs}$ = $\varnothing_{UHD-NWs}$).
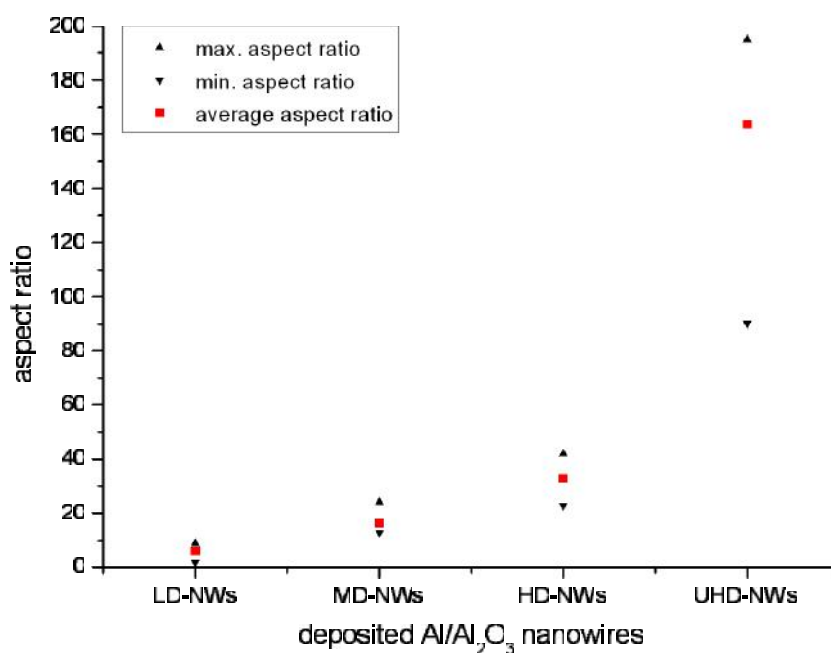
Figure 4.28: Aspect ratio of the deposited Al/Al$_2$O$_3$ NWs.

4.1.3.3.2 3D analysis

4.1.3.3.2.1 Analysis of the volume density (V_v), porosity (Φ), specific surface area (S_v), and specific surface area to volume ratio (SA/V)

It is known that bone porosity plays a key role on the mechanical integrity of the bone-cement interface[110]. However, pores in a metallic implant may lead to a focus for corrosion and loss of metal ions into the tissue. Walpole et al. showed how this problem is diminished by using, as in our approach, a porous coating of ceramic material on a non porous implant also alleviating the problem of the reduced implant strength[9].

Concerning the scale and size of the pores, the optimal value of the pore size is still open to debate. Several studies showed successful results using micro porosity. Hing and colleagues observed that micro porosity enhances bioactivity of synthetic bone graft substitutes[111] and values of ideal pore diameter have been reported between 100 and 500 μm[98-101] due to cell size, migration requirements and transport. On the other hand, nonporous alumina coatings have been also reported for improved bone implant interfaces[112]. In this context, Lavenus et al. showed recently adhesion and osteogenic differentiation of human mesenchymal stem cells on titanium nanopores[113]. Nanoporosity plays a key role at the first stages of tissue formation and especially in the cell-surface interaction phenomenon because the size of the proteins together with the amino acids involved on the early adhesion of the cell is mostly in the nanometre range.

In this work, the specific shape of the pores cannot be clearly defined due to the networking effect of the Al/Al$_2$O$_3$ NWs. Pore size distributions are not suitable parameters for the characterization of networked nanostructures and therefore an open porosity is assumed; nevertheless, the 3D reconstruction of the Al/Al$_2$O$_3$ coatings and the 2D porosity analysis revealed that the porosity is nanoscaled.

Concerning the total porosity (Φ) of the Al/Al$_2$O$_3$ coatings, figure 4.29 shows a value of approximately 80 % in all cases. A small decreasing tendency can be observed as the nanowire density increases. In the previous section, 2D porosity was analysed through thickness and width of the deposited coatings. In that case, the 2D % obtained was in the range between 70 % and almost 100 %.

All in all:

→ **High porosity values (average 80 %) have been found both in 2D analysis and 3D average analysis. It is well known that high porosity (maximal values between 70-90%) confined in small pores (nanoscale) is a characteristic of nanowires, nanofibres and network systems[87].** Our Al/Al$_2$O$_3$ NWs clearly exhibit such a behaviour, which opens up different applications.
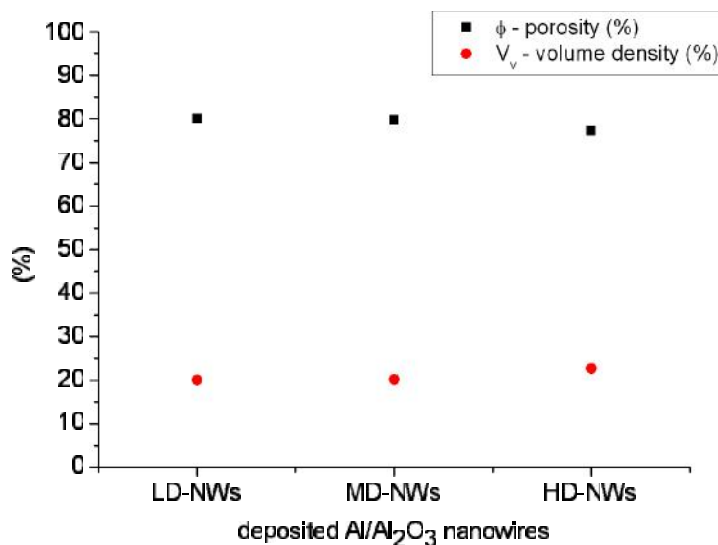
Figure 4.29: Total porosity (Φ) and volume density (V$_v$) depending on the Al/Al$_2$O$_3$ deposited coating.

On the other hand, specific surface area (S$_v$) and volume density (V$_v$) also play an important role. When the length scale of a material decreases from macro to nano, the fraction of surface atoms with respect to the bulk increases and this may substantially affect the properties of the nanostructure[115]. In this context, a proper quantification of the specific surface area of nanoporous materials is necessary for a better understanding of the properties that are affected by the high surface area to volume ratio. Figure 4.29 shows that the volume density of the Al/Al$_2$O$_3$ NWs is around 20 % regardless from the structure type while in the graph in figure 4.30 is observed that the specific surface area increases significantly. The graph from figure 4.30 represents values of 0.061 1/nm specific surface area for LD-NWs, 0.140 1/nm for MD-NWs and 0.147 1/nm for HD-NWs. A clear increase of the specific surface area is observed as the density of the structure increases. The large surface area nature of the Al/Al$_2$O$_3$ NWs leads to a mesh having porosity and an open framework as already seen in the 3D reconstructions.
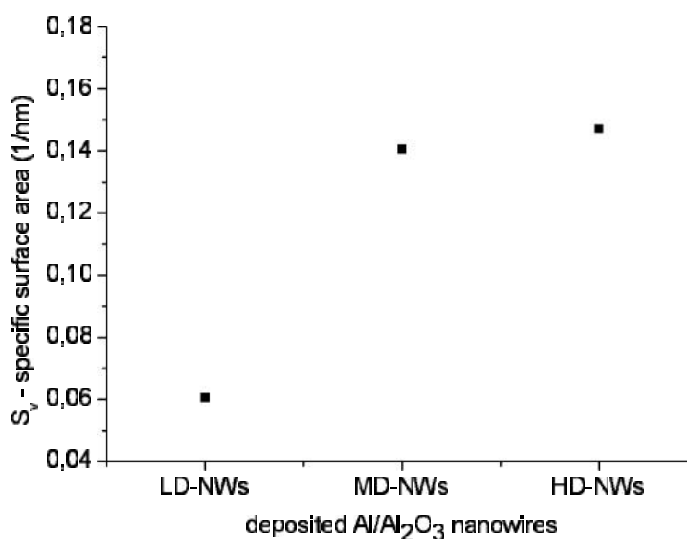
Figure 4.30: Specific Surface area (S$_v$) depending on the Al/Al$_2$O$_3$ deposited coating.

The surface-area-to-volume ratio (SA/V) is the amount of surface area per unit volume of an object. For a given shape, SA/V is inversely proportional to size. In involving a solid material, the SA/V ratio is an important factor for the reactivity. Materials with large surface area to volume ratios (very porous in our case) react at much faster rates than monolithic materials, because more surface area is available to react. Material properties associated with the high surface-area to- volume ratio are relevant for various applications, including catalysts[116-118], electrochemical supercapacitors[122-123], sensors and electrochemical actuators[123-126]. In case of a cube, as the size side increases the SA/V ratio clearly decreases. In this context, in case we had rectangular nanocuboids of any bulk material instead of Al/Al$_2$O$_3$ NWs the SA/V ratio would decrease slightly as it is observed in figure 4.31 (grey blocks). On the other hand, in the presence of Al/Al$_2$O$_3$ NWs the SA/V ratio increases enormously as the nanowire density increases. A SA/V ratio value 0.06 1/nm is observed for the LD-NWs while the SA/V ratio is more than double for HD-NWs.
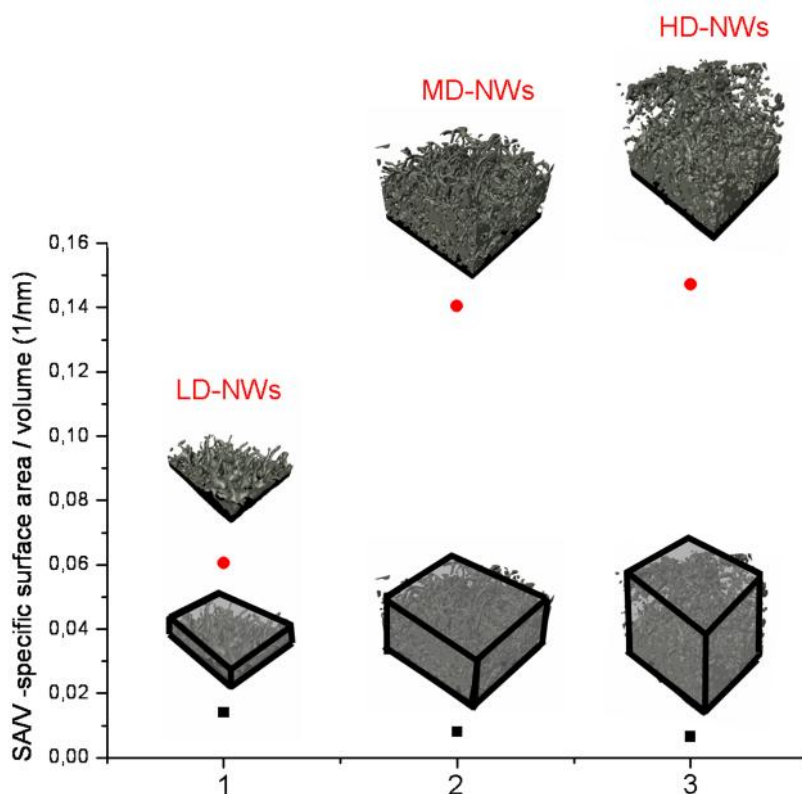
Figure 4.31: Specific Surface area to volume ratio (SA/V) comparison between supposed rectangular cuboids of any bulk material and Al/Al$_2$O$_3$ coatings.

4.1.3.3.2.2 Analysis of the geometric tortuosity (τ)

Tortuosity *(τ)* is one of the key parameters describing the geometry and transport properties of porous media. The concept of tortuosity was introduced by Carman in 1937[125], as a corrective factor needed to model the influence of the tortuousness of the domain available for displacement of a fluid phase. From the biological point of view, Chang et al. considered tortuosity a key factor in optimizing and designing tissue engineering scaffolds, which is known to influence molecules and oxygen diffusion and cell migration rate[126]. Silva et al. reported that aligned channel in both hydrokyapatite (HA) and poly (D,L- lactic acid) scaffolds enhanced cell penetration and infiltration into the central region of the scaffold in comparison with tortuous channels[127]. Recently, Leber et al. showed that tortuous channels had faster osteoblast growth than the control (non tortuous) ones[128].

In this context, tortuosity is the ratio between path length, L$_e$, and the straight length between the ends of the path, L (figure 4.32). In this sense, tortuosity will always be grater than or equal to 1. In this work, tortuosity is viewed as a property of the porous nanostructure that can be measured from the 3D geometry of the pore structure.
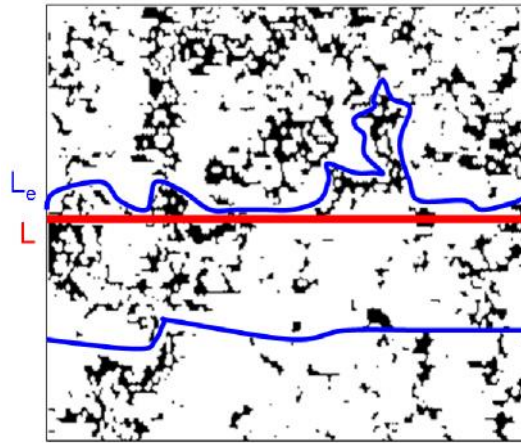
Figure 4.32: Concept of tortuosity on a planar view of Al/Al$_2$O$_3$ NWs.

In this context, the three dimensional nature of the nanotomography examination enabled tortuosity measurement in three directions perpendicular to each other: x, y and z, providing information on possible anisotropy in pore space distribution, as well as fluid flow paths between the nanowires. MAVI software was used, for each coordinate direction, to measure the ratio of the length of the shortest digital path between two foreground pixels located on opposite image borders and the image size in the given direction. The geometric tortuosity is then calculated by averaging over all such ratios[85].

Table 4.2: Geometrical tortuosity of the deposited Al/Al$_2$O$_3$ NWs in all directions

	LD-NWs				MD-NWs				HD-NWs			
	Av	Max	Min	STD	Av	Max	Min	STD	Av	Max	Min	STD
X	1.09	1.26	1.02	0.06	1.07	1.92	1.03	0.02	1.06	1.23	1.03	0.04
Y	1.17	1.62	1.06	0.08	1.19	1.58	1.06	0.08	1.23	1.38	1.23	0.04
Z	1.41	1.98	1.18	0.15	1.58	2.19	1.25	0.17	1.52	3.22	1.20	0.36

Table 4.2 shows the geometrical tortuosity of the deposited 1D Al/Al$_2$O$_3$ nanostructures in x, y and z directions. An average tortuosity value was obtained as well as maximum tortuosity, minimum tortuosity and standard deviations from the average values. In all cases the average connections in all directions are quite rectilinear (similar to 1) in x and y directions and more complex in z-direction. It is also observed that complexity in z-direction increases as the deposition time increases, especially for the maximum tortuosity values. In x-direction tortuosity remains rectilinear regardless to deposition time, while it increases for y-direction. The geometrical tortuosity is one of the parameters to take into account in nanofluidics. It is well known that nanofluidics have had a

significant impact in biotechnology; medicine and clinical diagnostics with the development of lab-on-a-chip devices for PCR related techniques[129]. In the frame of this work, the geometrical tortuosity is a parameter to take into account because the cell culture experiments made *in vitro* are done in fluid environments. A possible coated implant would be in contact with biofluids and blood, therefore characterizing the geometrical tortuosity of biomaterials could be interesting.

4.1.3.3.2.3 Analysis of the connectivity: Euler number (χ)

Odgaard et al. studied the quantification of connectivity in cancellous bone, with special emphasis on 3D reconstructions[130]. He presented that generally speaking, given a network consisting of nods and branches (points connected by lines), the network is said to be simply connected if only one path from any node to any other node exists (figure 4.33a). Such a network is known in topology as a tree and has by definition connectivity 0. If an additional branch is added between two nodes (discontinuous red line) some nodes connect by more than a single path, and the structure is multiply connected (figure 4.33b). If a branch in a tree is broken, the structure will fall apart, but in a multiply connected structure some branches may be cut without separating the structure into isolated parts. Connectivity is defined as a measure of the degree to which a structure is multiply connected, and hence, for a network, reports the maximal number of branches that can be broken before the structure is separated into two parts. As an example, figure 4.33a shows a simply connected node-and-branch network (tree). Only one path exists between any to nodes (e.g., from P1 to P2). Figure 4.33b shows a multiply connected network by the addition of a single branch (from P3 to P4). In this case there are two paths between P1 and P2. It is important to highlight that in our case the nanowires can connect with each other or branch creating connection points and high connectivity.
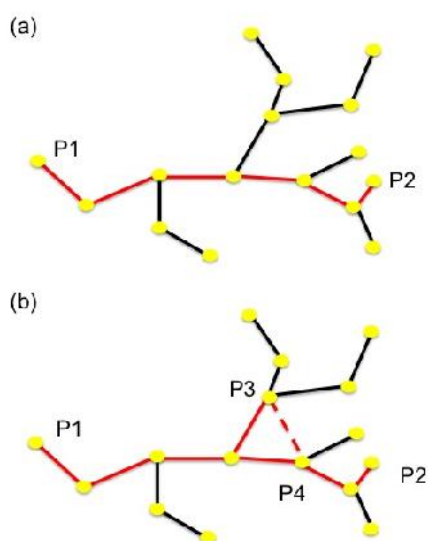
Figure 4.33: Concept of connectivity (Adapted from[130]).

In the medical field, osteoporosis ("porous bones") is a disease of bones that leads to an increase risk of fracture[131]. The main problems are that the bone mineral density (BMD) is reduced, the bone architecture deteriorates and the amount and variety of proteins in bone are altered. Focusing on the structural alterations, a loss of trabecular connectivity has been implicated in increased propensity for fracture. In this context, it is of high importance for the researchers developing biomimetic implants to consider connectivity of the implant material as a key parameter. Figure 4.32 shows the morphology of a healthy bone compared to that one of an osteoporotic bone. It is clearly seen that the trabeculas are thinner and less connected in case of the osteoporotic bone.

Figure 4.34: Osteoporosis problem. Left: Healthy bone, Right: Osteoporotic bone (image copyright from[132]).

In this contest, the Euler characteristic is known to have relation with connectivity; therefore it will be used for the connectivity determination in this work. The connectivity of the pixels depends on the chosen neighbourhood[89]. In this context, the used software MAVI uses 4 different neighbourhoods, or adjacency systems, for defining connectivity in the image. Neighbouring foreground pixels belong to the same object. If an adjacency system for the foreground is chosen, MAVI uses the complementary adjacency system for the background. Here, complementarity means that the corresponding estimators for the Euler number are consistent[89]. The Euler number (χ) is a topological characteristic, which describes the spatial connectivity and is calculated in the 3D space following the equation 4.1[133]:
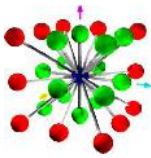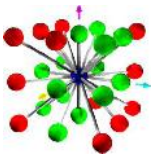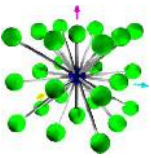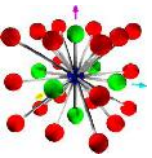
$$\chi = N - C = N_{holes} - N_{tunnels} \quad (4.1)$$

Where,

- N = particle number.
- C = connectivity.
- N_{holes} = amount of holes, which are connected components of the matrix and correspond to concave surface elements
- $N_{tunnels}$ = number of tunnels associated with saddle surface elements.

Table 4.3 shows the results of the 4 different neighbourhoods and Euler number. The Euler numbers as well as the neighbourhood values for all the Al/Al$_2$O$_3$ types are negative, which means that the Al/Al$_2$O$_3$ NWs form a well-connected network of pores. It is deduced from equation (7) that the more the Euler number is negative, the higher is the connectivity.

Table 4.3 Measured Euler number for different neighbourhoods and Euler number (χ)

	Neighbourhoods				Euler number (χ)
	14.1	14.2	26	6	
LD-NWs	-1892	-5037	-1736	-1932	**-1892**
MD-NWs	-2057	-5327	-1887	-2075	**-2057**
HD-NWs	-3676	-10194	-4667	-2237	**-3676**

In such porous structures, pore interconnections act as path-ways for tissue growth and formation[96-97]. In this regards, Odgaard et al. performed a 3D reconstruction of cancellous bone and calculated the Euler characteristics using similar procedures as the ones here described. The Euler numbers were -219.75 for non-purified bone and -650.5 for purified bone[130]. As well as in porosity, the optimum interconnection size and Euler numbers are still open to debate.

4.2 Surface characterization of the Al/Al$_2$O$_3$ NWs

4.2.1 Introduction

The study of the surface characteristics of biomaterials, specifically, implant materials is of essential importance. The nature and conformation of proteins on the implant are regulated by surface properties, in particular chemical composition, wettability and micro- and nanotopography[134-135]. It has been shown that nanotopography does not only control protein adsorption but also cell morphology and adhesion[136-137]. In this context, the surface topography must be analysed not only at the cell scale but also at the scale below the cell scale. Topography and chemistry are known to be key factors for cells. In our approach, a model is used where chemistry remains same but topography varies. In this section, the surface characteristics are analysed.

4.2.2 Experimental approach

4.2.2.1 CVD deposition on glass

Glass coverslips (Ø = 12 mm, Roth, Germany) were used as substrates in this experiment. Al/Al$_2$O$_3$ NWs were deposited on the glass coverslips by CVD technique using the molecular precursor [^{t}BuOAlH$_2$]$_2$ as explained in chapter 3. For this experiment a specific graphite susceptor was designed in order to adapt the graphite geometry as much as possible to the sample size. For this purpose, 21 holes (Ø$_{hole}$ = 12 mm) were perforated on the graphite. This geometry allowed us to coat 21 samples at the same time under identical conditions. For every density type several samples were fabricated for characterization purposes. An approximate number of 50 samples were produced. In total, 200 samples were produced.

4.2.2.2 Transmission

Transparency is defined in the field of optics as the physical property of allowing light to pass through a material. The opposite property is opacity. The transparency of the coated samples dealt in this thesis has been measured with a broad band spectrometer (Baki Spek, Latarum, Turkey) using a halogen lamp as light source. A bare glass coverslip was used as background.

4.2.2.3 Ultraviolet–Visible spectroscopy (UV-Vis)

Ultraviolet–visible spectroscopy (UV-Vis) is the measurement of absorption or emission after the light passes through a sample or reflects from a sample surface. Its range covers far UV to near-IR (190-900 nm). As UV and Vis light photons are energetic enough to promote outer electrons to higher energy levels, UV-Vis spectroscopy is usually applied to molecules or inorganic complexes. The UV-Vis spectra often have broad features that are of limited use for sample identification but are very useful for quantitative measurements. For this work, optical absorption measurements were

carried out with a standard spectrophotometer (Carry Varian 5000 UV-VIS-NIR) operating with a spectral resolution of 2 nm at room temperature, with a deuterium lamp for UV and a tungsten halogen lamp for the visible region. The spectrophotometer is equipped with an integrating sphere to collect diffuse or total reflection.

4.2.2.4 X-ray photoelectronspectroscopy (XPS)

In this work we used XPS to demonstrate that in the four different nanostructures formed by 1D Al$_2$O$_3$ NWs (LD-NWs, MD-NWs, HD-NW, and UHD-NWs) the surface chemical state is not changing. The surface composition was analysed using a PHI 5600 XPS employing a monochromatic AlKα X-rays prior to cell-culture experiments.

4.2.2.5 Roughness (profilometer and AFM)

In order to investigate the nano and the micro roughness two techniques were used. A profilometer (3D profilometer ZEISS Surfcom 1500 SD3) equipped with a diamond stylus, which is moved at a constant rate across the surface was used in order to study the micro roughness. The rise and fall of the stylus is detected electronically, amplified and recorded on a strip chart, or processed electronically to produce readings for a meter. For nanoroughness investigations atomic force microscopy (AFM) technique was used. AFM is a very-high resolution type of scanning probe microscopy and its resolution is of fractions of a nanometre. In AFM a sharp probe is scanned across the surface and the tip/sample interactions are monitored. In the frame of this work an AFM (Nanowizard 3, JPK instruments, Germany) was used in tapping mode.

4.2.2.6 Contact angle

The contact angles of water and glycerin with the Al/Al$_2$O$_3$ surface were measured by goniometry using a semi automated contact angle meter (G2 Krüss, Germany). The samples were placed on a flat stage and a drop of distilled water was placed on the surface. Also contact angle with glycerin was measured. The surface tension of the distilled water was 72.8 mN/m (used for surface energy calculation). For each sample type, at least 5 measurements were determined for every liquid.

4.2.3 Results

4.2.3.1 Transmission measurements

After eye inspection of the deposited Al/Al$_2$O$_3$ it is observed that the transparency of the coating decreases as the deposition time in the CVD chamber increase. The colour of the sample changes from grey to deep black and the opacity increases. In figure 4.32 it can be appreciated how the sample LD, corresponding to low density nanowires (LD-NWs), is quite transparent. The INM logo can be clearly seen through the sample. On the other hand, it is observed that the UHD sample,

corresponding to ultra high density nanowires (HD-NWs), is totally black. The INM logo is not readable in this case. Sample MD, corresponding to MD-NWs, is more opaque than sample LD but still a high transparency is observed. Sample HD, corresponding to HD-NWs, showed high opacity but still parts of the INM logo are seen through the sample.

Figure 4.35: Optical images of the Al/Al$_2$O$_3$ NW samples.

In order to quantify the transparency of the sample, transmission measurements were performed. Transmission is defined in the field of optics as the physical property of allowing light to pass through a material. The opposite property is opacity. Upon interacting with a sample, incident light of intensity (I_0) may be partly reflected at optical interfaces (I_R), it may be scattered (I_S) and absorbed in the sample (I_A), the remaining part will be transmitted (I_T) as shown in figure 4.36[138].
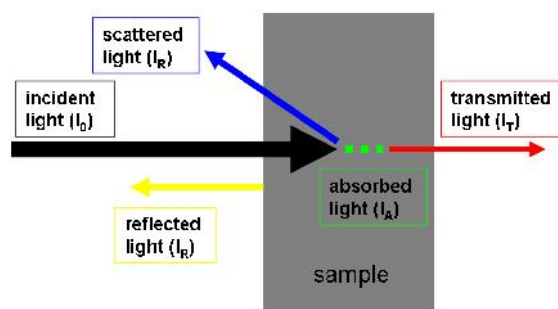
Figure 4.36: Energy balance of incident light upon interaction with sample (Adapted from[138]).

According to the law of conservation of energy, the energy balance for the incident light may be written as:

$$I_0 = I_R + I_S + I_A + I_T \quad (4.2)$$

In the frame of this work transmission (I_T) has been measured using a broadband spectrometer and as a result the intensity spectra shown in figure 4.37a was obtained. It is observed that glass has the highest transmission intensity (yellow line). The maximum point reaches almost 90 %. Concerning the deposited Al/Al$_2$O$_3$ it is observed that as the density increases the % of transmission intensity

decreases. LD-NWs and MD-NWs show transmission intensities bigger than 50 % while HD-NWs and UHD-NWs % of transmission intensity is below 20 %.
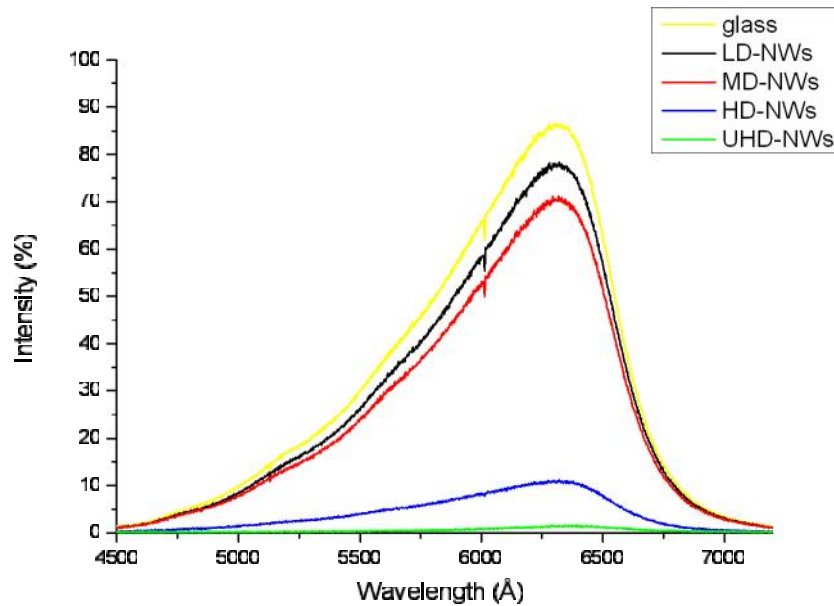
Figure 4.37a: Transmission intensity of the incoming light for every Al/Al$_2$O$_3$ deposited density.

An average value of transmission was measured for every Al/Al$_2$O$_3$ sample type. Table 4.4 shows the obtained values. While the transmission for LD-NWs is around 90 %, for UHD-NWs is almost 1 %.

Table 4.4: Transmission measurements:

	LD-NWs	MD-NWs	HD-NWs	UHD-NWs
Transmission (%)	89.52	74.15	15.52	1.34
Standard deviation	4.48	4.73	2.78	0.74

As it is observed in Figure 4.37b, the relationship between transmission (%) and deposition time (min) is not linear. It has been shown in the previous section of this chapter that neither the thickness of the coating follows a linear tendency in relation with the coating time. Similarly than in this case, the non-linearities were observed for HD-NWs and UHD-NWs. All in all, it can be concluded that as the deposition time increases the thickness of the coating is thicker and the transmission (%) decreases. The fact that the HD-NWs and the UHD-NWs present a more entangled nature would explain the non-linear behaviour.
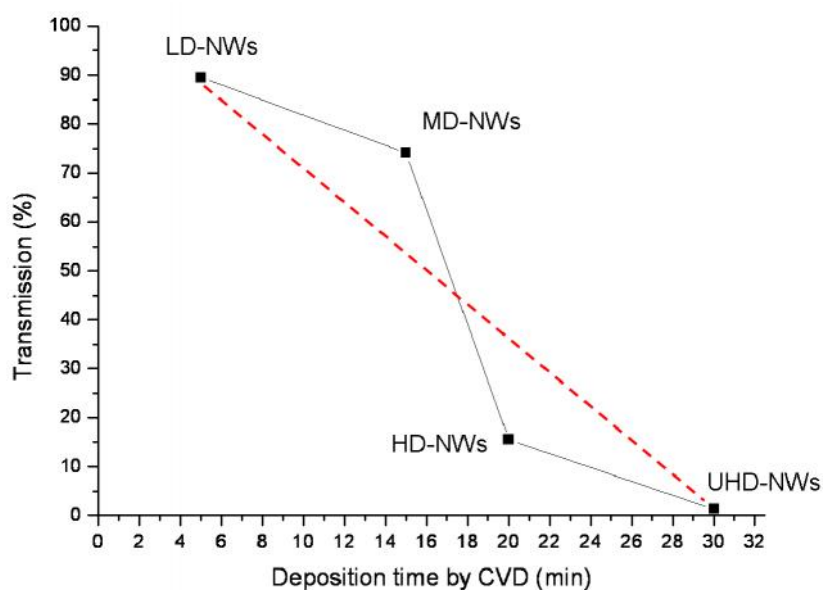
Figure 4.37b: Relationship between transmission (%) and deposition time (min) for every sample type.

4.2.3.2 UV-VIS

Figure 4.38 shows the UV-Vis spectra of Al/Al$_2$O$_3$ NWs. The most characteristic peak in the spectra for all three densities is a narrow and sharp peak that can be seen at about 250 nm. This peak could be qualified to the dipolar mode of the surface plasmon resonance of Al cores encapsulated by the dielectric Al$_2$O$_3$ shells. The spectrophotomer has some limitations, and this is why there is some noise in the spectra at 200 nm. Due to bulk plasma resonance a strong increase in the UV region is seen. It is known that down to a wavelength of 200 nm Al has low absorption because of its free-electron-like character and high bulk-Plasmon frequency. Elkinci et al. showed that Al spherical nanoparticles with diameters of 40 nm exhibited two distinct resonances in the UV region one at 250 nm and the other one at 190 nm. The first one is due to the dipolar plasmon resonance while the second peak is formed from the quadrupolar mode according to Mie's theory.
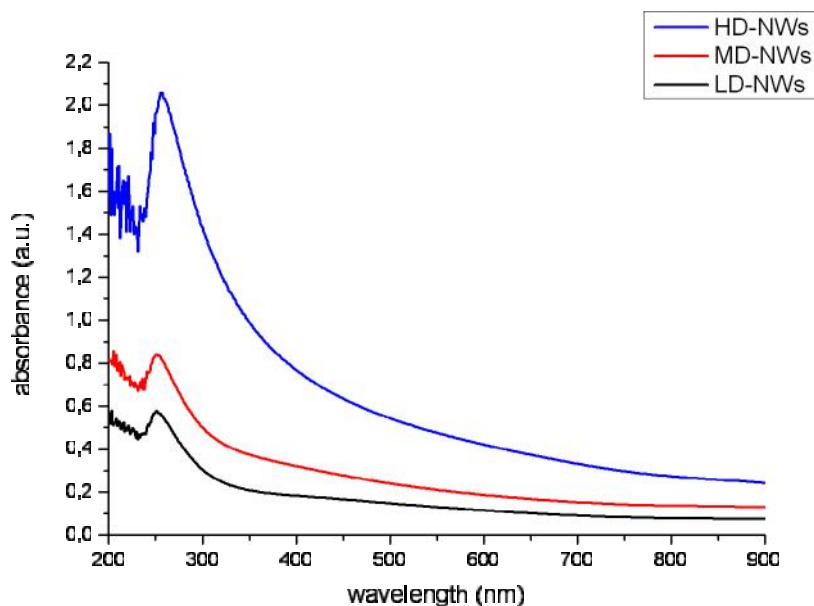
Figure 4.38: UV-VIS-NIR spectra of Al$_2$O$_3$ NWs.

As the density increases, the intensity of the peak at 250 nm becomes more intense than in lower densities. The peak for the HD-NWs spectra of Al/Al$_2$O$_3$ NWs has some particularities. In first place, this is higher than the peaks for MD-NWs and LD-NWs, and in second place, its spectrum shows a red shift and broadening out due to retardation effects and emergence of higher order plasmon modes. Elkinci[139] explained that the red shift of the plasmon peaks and observation of high-order plasmon modes are relatively significant for Al nanoparticles compared with Au and Ag nanoparticles of similar dimensions.

4.2.3.3 XPS

Figure 4.39b shows the XPS spectra of Al/Al$_2$O$_3$ NWs obtained by the decomposition of [^{t}BuOAlH$_2$]$_2$. In all deposited coatings (LD-NWs, MD-NWs, HD-NWs and UHD-NWs) the spectra appeared the same, which proves that all the studied nanostructures have the same surface chemistry. Some characteristic peaks can be detected. As this was probed[142] the carbon 1s binding energy (BE = 284.6 eV) peak was used as reference. Also we can observe the broad scan for Aluminium oxide. The peaks identified on those figures are Al 2p, Al 2s, C 1s and O 1s. The presence of carbon is mainly due to contamination from the ambient environment after deposition.
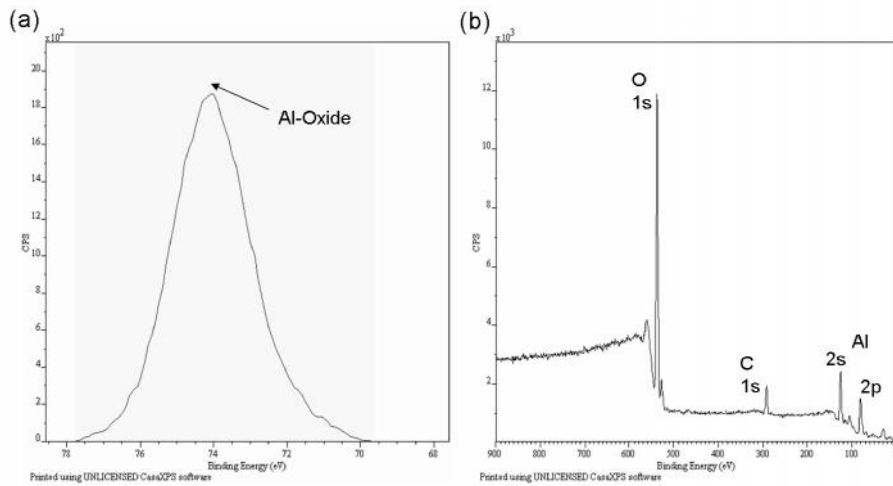
Figure 4.39: (a) Al (2p) spectra for all densities (b) XPS spectra of Al/Al$_2$O$_3$ NWs for all densities.

Figure 4.39a shows the XPS spectra of Al (2p) of our Al/Al$_2$O$_3$ nanowire coated samples. It is know from the literatures[140] that the core level XPS spectra of Al (2p) reveals that the binding energy of aluminium is 74.5 eV, which corresponds to Al^{3+} state (Al 2p spin-orbit components). Symmetric nature of core level XPS spectra of Al (2p) clearly reveals that no other sub oxides of Al are present in the coating.

4.2.3.4 Roughness analysis with AFM and profilometer

Roughness is one of the surface characteristics, which scientifically influences cell differentiation, local factor production and consequently, bone growth and osseointegration[141-144]. As shown in figure 4.40, micro and sub-micro scale roughness exhibit feature sizes comparable to those of resorption pits and cell dimensions which leads to enhanced osteoblast differentiation and local factor production *in vitro*[145-146], increased bone-to-implant contact *in vivo*[147-148] and improved clinical rates of wound healing[149-150]. On the other hand, surface nanoscale roughness plays also a key role because it directly corresponds to the sizes of proteins and cell membrane receptors, which affect osteoblast differentiation and tissue regeneration. During the last ten years the interest increased and several research groups studied the effect of nanoscale roughness on osteoblast response[153-154].
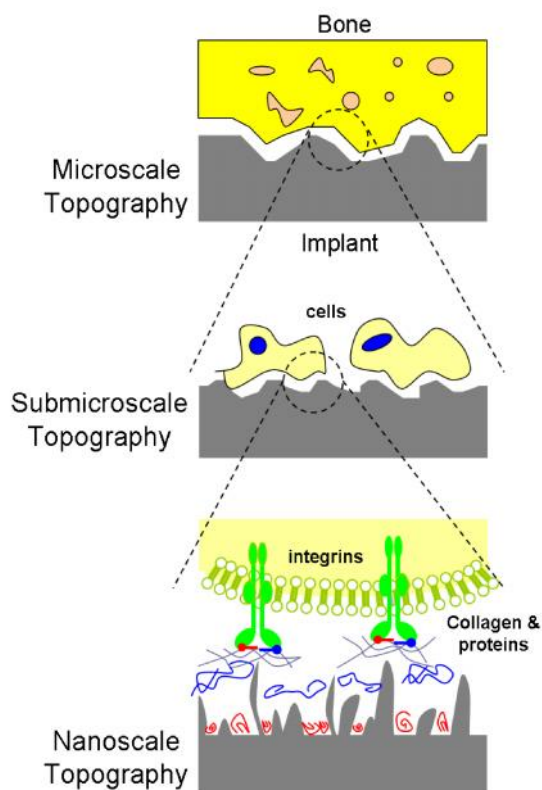
Figure 4.40: Schematic of the interactions between bone and implant surface at different topographical scales (Adapted from[155]).

In this context, roughness has been measured using an AFM apparatus and a profilometer at different scan ranges. As a result, the arithmetic mean (R$_a$) and root mean square (RMS) values have been obtained as well as images for all deposited nanostructures.

Ponche et al. showed that in all roughness measurements, the surface amplitude defined by z is given by a function of z = f(x) for a profile recording and z = f(x,y) for a surface recording. The first important remark is that it is impossible for any apparatus used for surface topography characterisation to record surface when the roughness is composed of caverns or more precisely when z = f(x,y) is not a unique for a fixed (x,y). Actually, all apparatus give the value of z = Sup [f(x,y)][6]. Figure 4.41 illustrates this problem; the red line represents z = Sup [f(x,y)] on a cross view of the Al/Al$_2$O$_3$ 3D models. This red line will be, conceptually, the measured roughness. Nowadays, no non-destructive techniques exist that can be used to verify that no caverns are present on the surface topography. In the frame of this work, FIB-nanotomography, which is a destructive technique, has been used in order to perform a better observation of the pores and cavities (section 4.1).
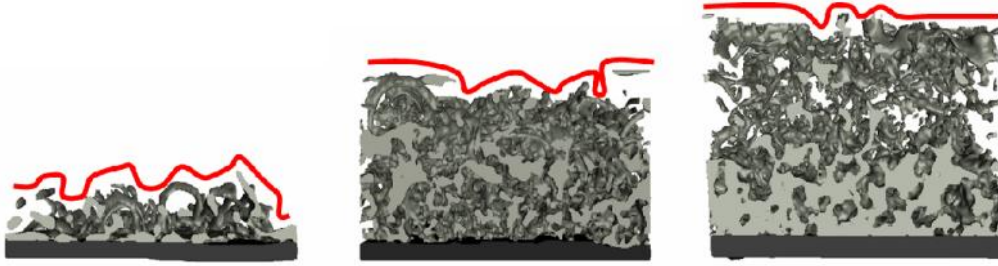
Figure 4.41: Example of limited aggregation structure on our Al/Al$_2$O$_3$ modelled nanowires.

Another problem is that in most cases the tip is not sharp enough to describe the surface features correctly. The AFM image is the result of the interaction between the tip and the sample surface. The dilatation phenomenon tends to smooth the sharp features and fill the holes[156]. The studied Al/Al$_2$O$_3$ NWs present a complex structure plenty of holes and sharp features; consequently, this phenomenon is observed in our results. Nevertheless, AFM offers an incomparable resolution and is the ideal tool to describe topography at the submicron scale.

Figures 4.42 and 4.43 show planar images recorded using AFM for all deposited nanostructures in areas of 4 µm x 4 µm and 2 µm x 2 µm respectively. In figure 4.42 clear differences are observed between the deposited Al/Al$_2$O$_3$ nanostructures: LD-NWs (figure 4.42a) showed a quite rough and homogeneous profile. The clearer areas correspond to the higher points of the coating, which are nanowire tips and loops. Tips and loops cannot be differentiated due to the measurement mechanism (figure 4.41). No further detail can be observed due to the dilatation phenomenon previously described. In case of MD-NWs (figure 4.42b), round shaped particles are detected, which again correspond to the tips and loops found at the top of this layer. In figure 4.42c, corresponding to high density 1D Al/Al$_2$O$_3$ NWs HD-NWs, a rougher profile is assumed. While a homogeneous roughness was observed for LD-NWS and MD-NWS, some clusters are observed in HD-NWs (figure 4.42c). Some agglomerations are clearly visible at the top of the surface. In case of UHD-NWs, a cauliflower morphology formed by micro balls with nanowires over them was detected after SEM and cross section analysis. The present results corroborate this morphology. The image from figure 4.42d shows more clusters than in the other deposited structures. Some nanowires are observed on top of the clusters.

All in all, it is clear that **the nanoroughness increases as the Al/Al$_2$O$_3$ density increases, especially due to the cluster formations in HD-NWs and UHD-NWs. While LD-NWs and MD-NWs are more uniform, images corresponding to HD-NWs and UHD-NWs show µm-structures and clustering**.
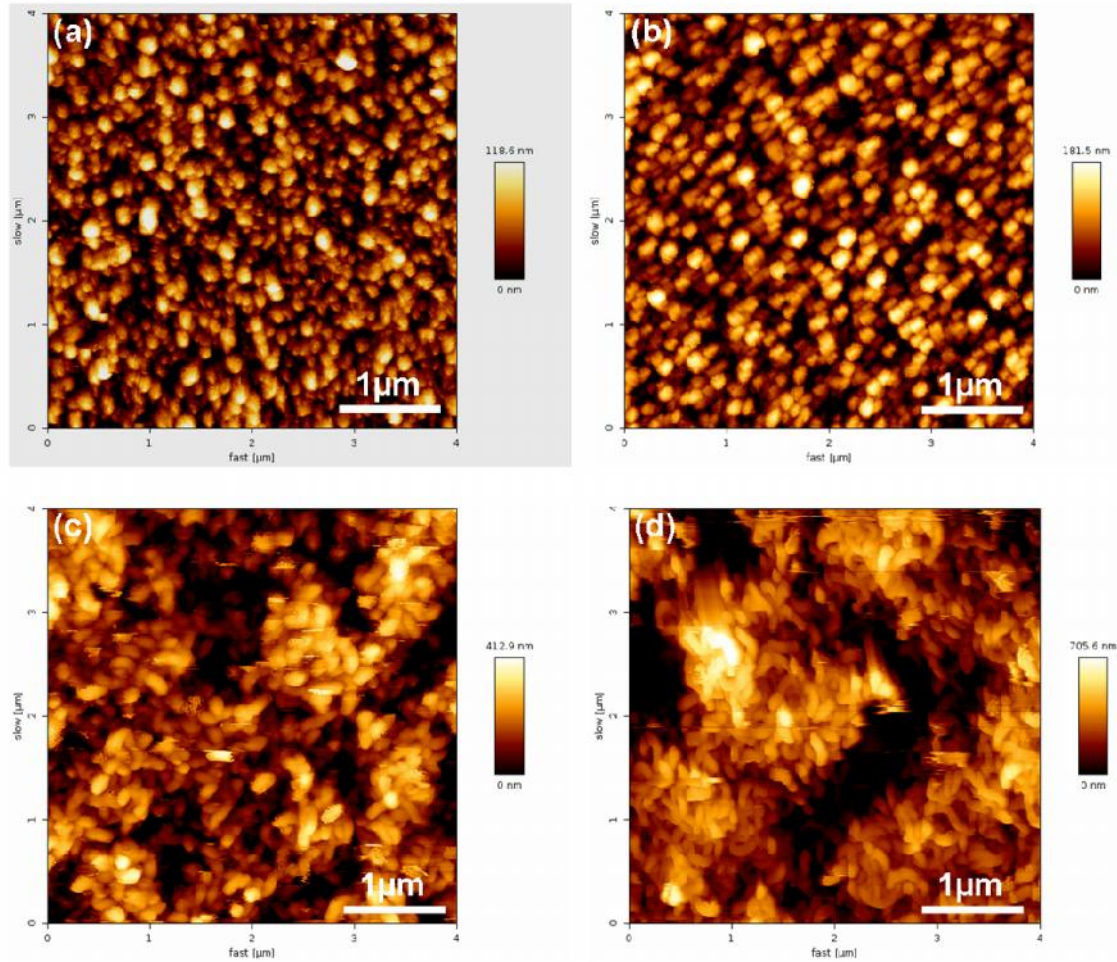
Figure 4.42: AFM images (4µm scan range) for (a) LD-NWs, (b) MD-NWs, (c) HD-NWs and (d) UHD-NWs.

In figure 4.43 a smaller scanning range was investigated during the measurements and therefore, the Al/Al$_2$O$_3$ NWs can be analysed in more detail. It is observed that the quality of the images is not optimal due to the dilatation phenomena explained previously. As a consequence the nanowire tips are seen as balls and their sharpness is not detected. However, it can be observed, similarly than before, that as the Al/Al$_2$O$_3$ density is increased the surface becomes rougher due to the presence of µm structures. Once more, the clearest differences concerning topography are observed between LD-NWs and UHD-NWs. Less differences are observed between LD-NWs and MD-NWS. HD-NWs can be considered as an intermediate structure between the less dense nanostructures, which showed a chaotic and spaghetti-like topography, and the denser coating, which showed a cauliflower-like structure.
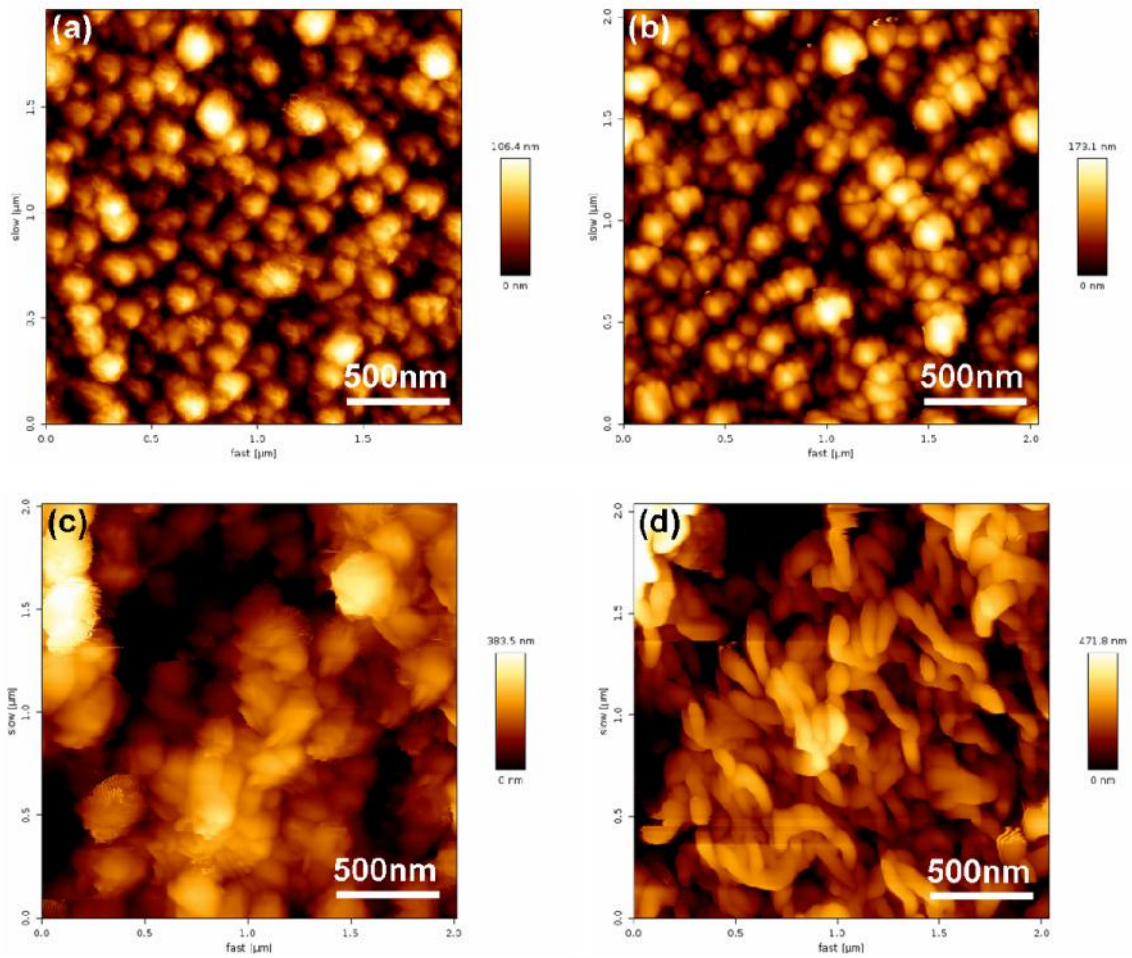
Figure 4.43: AFM images (2µm scan range) for (a) LD-NWs, (b) MD-NWs, (c) HD-NWs and (d) UHD-NWs.

Concerning the numerical values, average roughness (R$_a$) and root mean-square (RMS) were measured by AFM using scan ranges of 4 µm and 2 µm. An additional measurement was performed by profilometry with a scan range of 2 mm.

R$_a$ is one of the most common parameter for surface texture. R$_a$ is calculated by an algorithm that measures the average length between the peaks and valleys and the deviation from the mean line on the entire surface within the sampling length using the formula from figure 4.44. R$_a$ averages all peaks and valleys of the roughness profile, and then neutralizes the few outlying points so that the extreme points have no significant impact on the final results[157]. RMS is an average between the height deviations and the mean line/surface, taken over the evaluation length/area.

$$R_a = \frac{1}{L} \int_0^L |f(x)| \, dx$$

$$RMS = \sqrt{\frac{1}{L} \int_0^L f^2(x) \, dx}$$
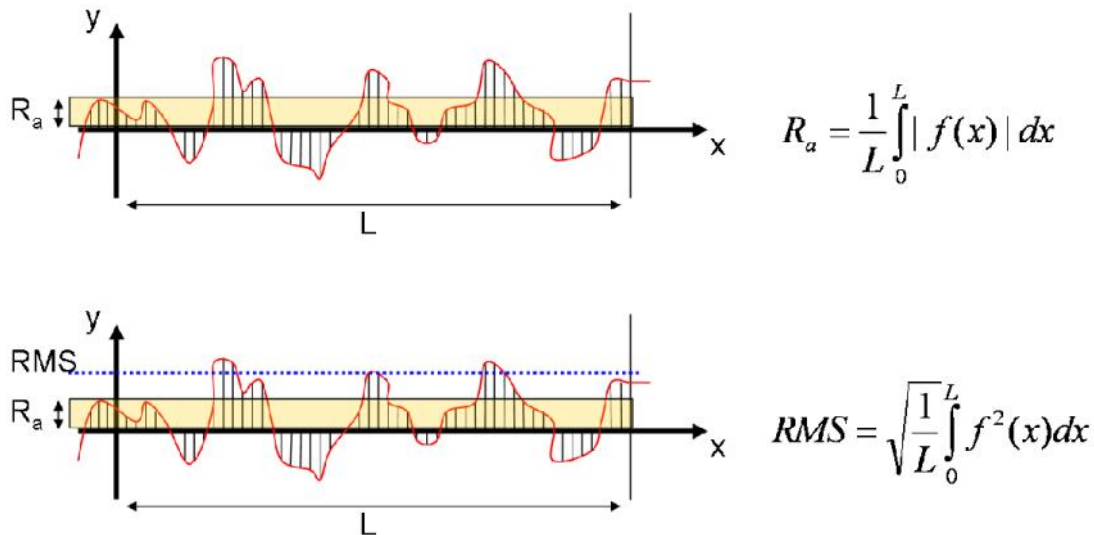
Figure 4.44: Concept and formula for R$_a$ and RMS.

The graphs represented in figure 4.45 show the tendencies of R$_a$ and RMS depending on the Al/Al$_2$O$_3$ deposited nanostructure. For every measurement, the tendency of three different scanning areas has been depicted. The roughness values for 2µm X 2µm and 4µm X 4µm scanning areas have been measured with AFM while the roughness values for 2mm x 2mm scanning areas have been measured using profilometry techniques.

The measurements made with profilometry showed no big changes between densities. In this regard, a flat tendency is observed in both graphs from figure 4.45 for the profilometry measurements (black dots). The values for all deposited nanostructures were around 7 nm for R$_a$ and 10 nm for RMS.

On the other hand, the measurements performed with AFM showed significant differences between the four 1D Al/Al$_2$O$_3$ deposited nanostructures. It is clearly observed that the R$_a$ and RMS values increase, as the Al/Al$_2$O$_3$ coating is denser. In case of LD-NWs, MD-NWs and HD-NWs almost no differences are observed on the R$_a$ and the RMS values performed at different scanning ranges. On the contrary, the differences between the measurements performed with a scanning range of 4 µm (blue triangles) and with a scanning range of 2 µm (red triangles) are very abrupt in case of UHD-NWs. This is due to the clusters formed at top of this nanostructure. These clusters have sizes between 1 and 3 µm and therefore at a scan range of 2 µm they cannot be scanned completely while at a scan range of 4µm at least a whole cluster can be scanned.

To sum up:

→ **The roughness values lead to the conclusion that in a <u>high microscale (mm)</u> all Al/Al$_2$O$_3$ deposited nanostructures showed same behaviour, while in a <u>lower microscale</u> and nanoscale roughness increase as the deposition time increase. These results show clearly that the <u>roughness values change immensely depending on the scanning range</u>.**
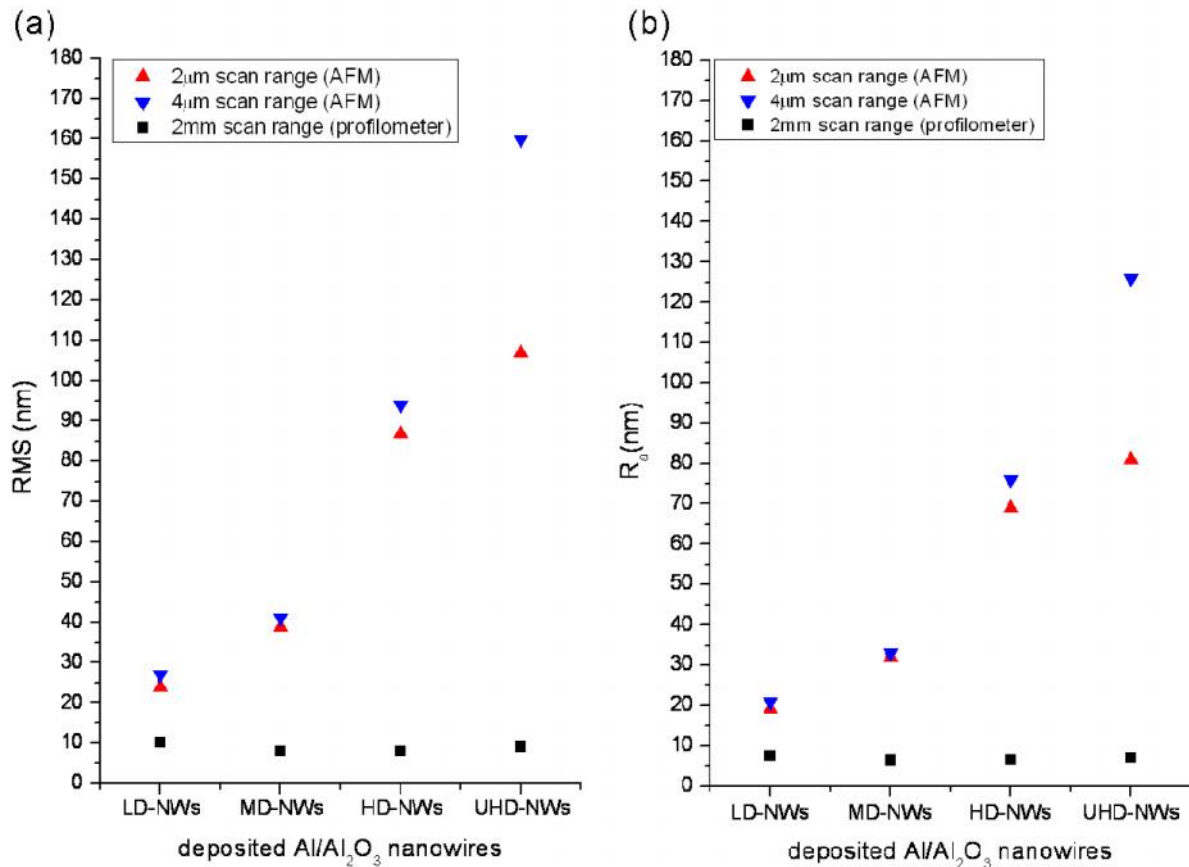
Figure 4.45: Roughness values for all deposited Al/Al$_2$O$_3$ NWs measured at different scanning ranges (a) RMS and (b) R$_a$.

The graphs in figure 4.46 represent the aspect ratio versus the R$_a$ values of the deposited Al/Al$_2$O$_3$ nanostructures for nano and micro roughness. The aspect ratio was obtained using the cross section images from the FIB experiments (section 4.1). While the aspect ratio shows an exponential increasing tendency as the coating density increases, the nano roughness (R$_a$) shows a less abrupt increasing tendency (figure 4.46a). On the other hand, the micro roughness (figure 4.46b) remains constant regardless of the density type. The main reason is the highly entangled nature of the as deposited Al/Al$_2$O$_3$ nanostructures. Such an entanglement cannot be detected by means of surface measurement.
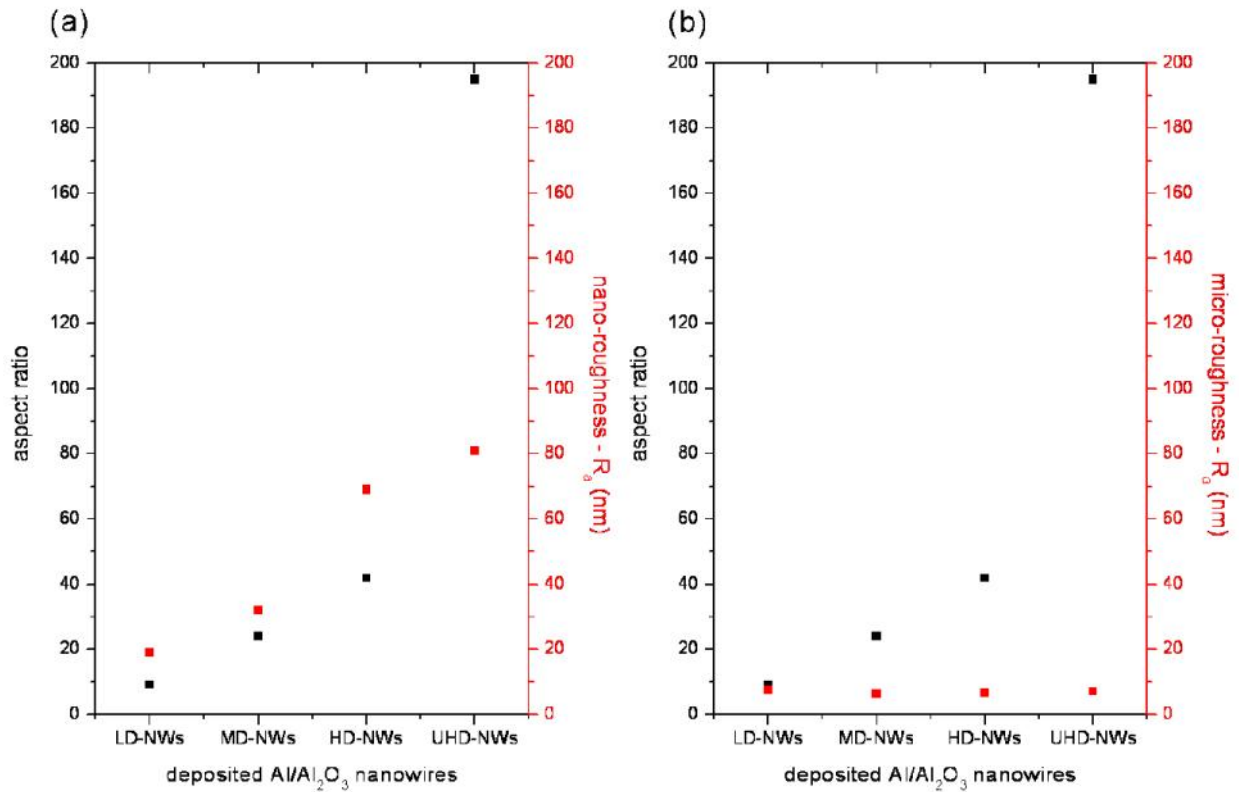
Figure 4.46: Aspect ratio versus (a) nano-roughness and (b) micro-roughness.

4.2.3.5 Wetting

As blood contains a high percentage of water, the research that relates surface wettability to biocompatibility is of high interest. Even though the contact angle itself is not an indicator of biocompatibility of materials, some possible correlations have been found between the protein absorption behaviour and the wetting angle of material surfaces[158]. It is widely observed that cell adhesion and subsequent activity are generally better on hydrophilic surfaces. Therefore, is not surprising that materials able to integrate with bone, for example, titanium and hydroxyapatite, are to a greater or lesser degree, hydrophilic[159]. In terms of nanotechnology, nanomaterials can also play a role in increasing wettability. For example, Balasundaram and Webster demonstrated that aqueous contact angles were three times smaller (more wettable) when alumina grain size was decreased from 167 to 24 nm[159]. They also reported that the adsorption of vitronectin, which simulates osteoblast adhesion, increased on nanophase ceramics with greater wettability.

The behaviour of a water drop was firstly described by Young[160]. He used the following relationship:

$$x_{sf} - x_{sl} - x_{lf} \cos \theta_x = 0 \qquad (4.3)$$

Where,

- x_{lf} = Surface free energy of liquid/fluid

- x_{sl} = Surface free energy of solid/liquid

- x_{sf} = Surface free energy of solid/fluid

- θ_x = Young angle

Nevertheless, this relation is only applicable on surfaces that are physically smooth and chemically homogeneous. Several studies demonstrated that roughness, as well as chemical heterogeneities, influence on contact angle values. Several models have been proposed to define the relationship between roughness and wettability. During the 30s Wenzel analysed the resistance of solid surfaces to wetting water[161]. During the 40s Cassie and Baxter studied the wettability of porous surfaces and proposed their well-known model[162]. In this context, de Genes et al. proposed that there could be at least three regimes for the contact area of the drops on rough surfaces[163]: the Wenzel regime (figure 4.47a), where the solid/liquid interface exactly follows the solid roughness, the air pocket regime (figure 4.47b), where air patches are confined below the drop and the penetration regime (figure 4.47c), where an area surrounding the drop is impregnated by a liquid film. During the same decade, Shuttleworth et al. modelled the spreading of a liquid over a rough solid[164] and later in the 80s Cazabat and colleagues analysed the dynamics of wetting and the specific effects of the surface roughness[165]. Similarly, de Genes et al. made a deep study on statistics and dynamics of wetting[163]. During the last ten years "superhydrophobic" and "superhydrophilic" behaviours have been intensely studied by numerous authors and a lot of efforts have been done on structures surfaces bearing well ordered micro –to nanoscale patterns.
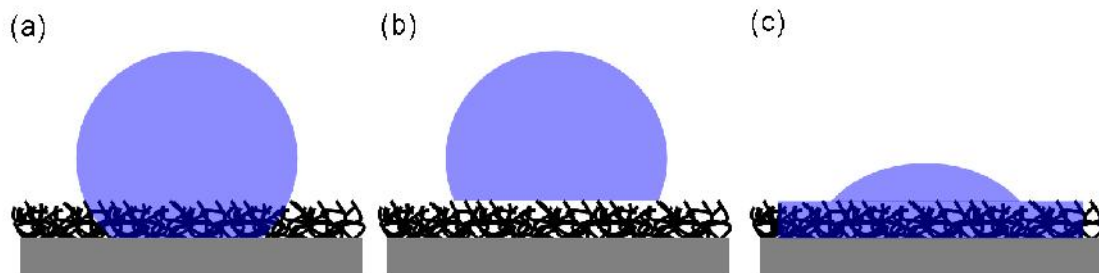
Figure 4.47: Three regimes: (a) Wenzel regime, (b) Cassie-Baxter, air pocket regime and (c) Cassie-Baxter, penetration regime.

The Wenzel regime:

The Wenzel model[161] of wetting on rough surfaces uses the ratio r between the actual surface area supposed to be fully wetted by liquid, and the projected planar area to describe the relation-ship between the apparent equilibrium contact angle measured on the rough surface (θ_w), and the Young angle (θ_x) of the smooth surface,

$$\cos(\theta_w) = r\cos(\theta_x) \quad (4.4)$$

Cassie and Baxter extended this model, which applies only when there is no gas entrapped beneath the drop. It is believed that the Cassie and Baxter model is more suitable to describe the wetting behaviour of nanoporous surfaces.

The Cassie-Baxter regime:

In the Cassie-Baxter model, the wettability of a chemical patchwork is described. Such patchwork is composed of two materials of respective proportions f_1 and f_2 ($f_2 = 1-f_1$) and of Young contact angles θ_1 and θ_2. The apparent contact angle is given by

$$\cos\theta^{**} = f_1\cos\theta_1 + f_2\cos\theta_2 \quad (4.5)$$

The Cassie-Baxter model can be applied to the air-pocket regime (AP) (figure 4.47b). In this case, the material is a composite made of solid and air. Namely, we have $\theta_1 = \theta$ and $\theta_2 = \pi$ (corresponding to the "contact angle" of a drop on air). Tacking into account that $f_1 + f_2 = 1$ we find that

$$\cos\theta_{AP} = W_S(\cos\theta + 1) - 1 \quad (4.6)$$

Being W_S the solid surface fraction wet by the liquid.

The Cassie-Baxter model also describes the penetration regime (P) (figure 4.47c), for which the substrate is a composite of solid and liquid. A liquid penetration into the nanopores could be driven by capillarity (Laplace's Law). In this case, $\theta_1 = \theta$ and $\theta_2 = 0$ (the "contact angle" of a liquid on itself), $f_1 = W_S$, and $f_2 = 1 - W_S$, which yields,

$$\cos\theta_P = W_S(\cos\theta - 1) + 1 \quad (4.7)$$

In figure 4.48a it is observed that the water contact angle for the Al/Al$_2$O$_3$ nanosized coated samples is in all cases < 10°. Interestingly if the Al/Al$_2$O$_3$ surface becomes globular (balls) in the nm-regime, the surface becomes ultra-hydrophobic[166]. 1D Al/Al$_2$O$_3$ NWs enhance hydrophilicity and showed higher hydrophilic behaviour than the glass coverslips used as substrate (~35°). There is no difference between the four Al/Al$_2$O$_3$ densities, which drives us to the conclusion that the Al/Al$_2$O$_3$ coated surfaces studied in this work are hydrophilic independently from the deposited nanostructure. From the biological point of view, it is known that vitronectin and fibronectin, which are involved in bone formation, are hydrophilic proteins[167].
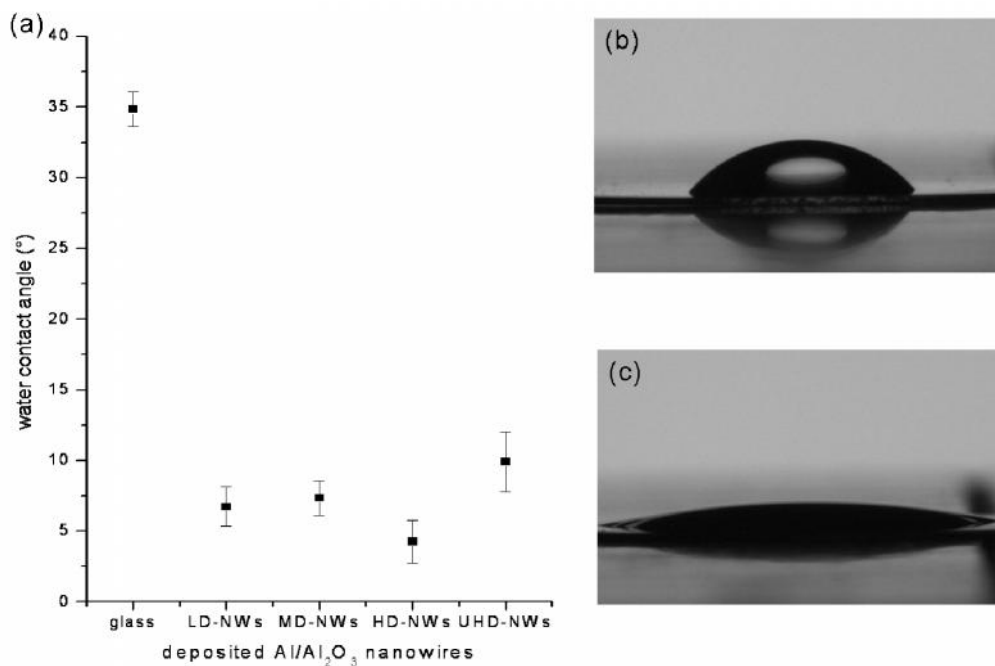
Figure 4.48: Contact angle of the Al/Al$_2$O$_3$ deposited nanowires with water. (a) Graphic (b) water drop on glass and (c) water drop on Al/Al$_2$O$_3$ deposited nanowires.

Additionally, the surface energy of the Al/Al$_2$O$_3$ nanowire surfaces has been calculated using the following relation[168]:

$$E_s = E_{lv} \cos \theta \quad (4.8)$$

Where,

- E_s = Surface energy of the contacting surface
- E_{lv} = Surface energy between the water and air under ambient conditions (MJ/m^2)
- θ = Static contact angle

Figure 4.49 shows how the calculated surface energy of the Al/Al$_2$O$_3$ NWs decreases as the density of the deposited 1D nanostructure increases. As may be noticed the overall surface energy is a very rough parameter to understand phenomena as wetting angles. Nevertheless, a tendency is observed: the contact angle remains constant for all densities due to μm effect of the surface. On the other hand, the surface energy decreases as the deposited density increases as a consequence of the nm effect of the surface.
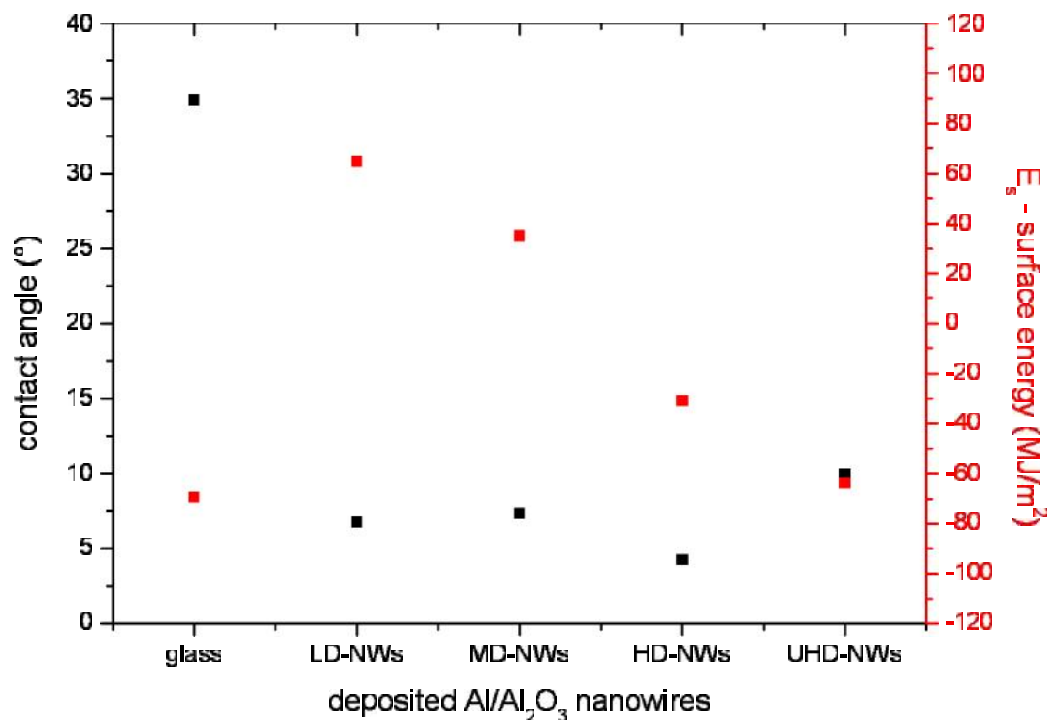
Figure 4.49: Calculated surface energy versus contact angle with water depending on the density of the deposited Al/Al$_2$O$_3$ NWs.

In figure 4.50 the behaviours of the different deposited Al/Al$_2$O$_3$ NWs in contact with oil and water are compared. For this experiment, the contact angles of glycerin and water with the surface of all deposited coatings were measured. Glycerin is a simple polyol compound. It is a colourless, odourless, viscous liquid that is widely used in pharmaceutical formulations. It has three hydroxyl groups that are responsible for its solubility in water and its hygroscopic nature. While the Al/Al$_2$O$_3$ NWs remain hydrophilic regardless of their density, they increase steadily their oleophilicity. For LD-NWs the contact angle with glycerin is almost 100° and for UHD-NWs is around 30°. A big gap has been observed between MD-NWs and HD-NWs. A difference of 40° has been observed in this case. It could be that the cauliflower structure observed in UHD-NWs enhances oleophilicity. These results lead to conclude that a main difference between the less dense coatings (LD-NWs and MD-NWs) and

the denser ones (HD-NWs and UHD-NWs) is the oleophilic behaviour of the second ones. The oleophilic behaviour of the Al/Al$_2$O$_3$ NWs has not been presented so far and could be promising in fields dealing with oil/water separation and oil sorbents.
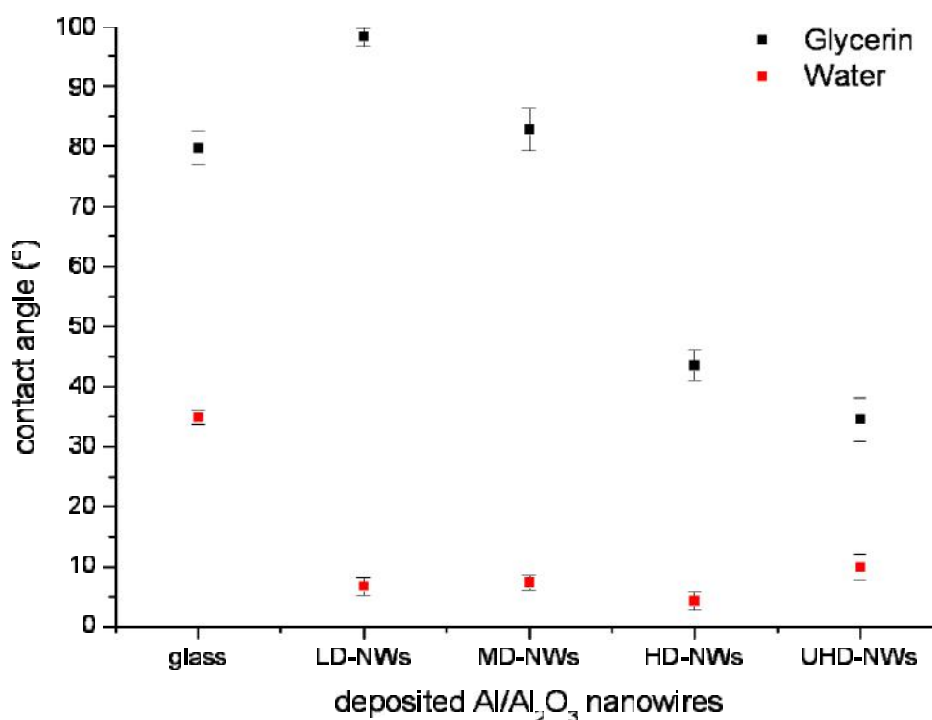
Figure 4.50: Contact angle with water and glycerin of the different deposited Al/Al$_2$O$_3$ NWs.

Last but not least, roughness and contact angles were plotted in order to find a correlation between them. As seen previously, the contact angle with water showed that the deposited Al/Al$_2$O$_3$ nanostructures exhibit hydrophilic behaviour. Figure 4.51a showed that the water contact angle remains constant while the nanoroughness (R$_a$) increases as the Al/Al$_2$O$_3$ nanostructure are denser. In figure 4.51b both, water contact angle and micro roughness, remain constant regardless of the density type. We did not observe a clear correlation between roughness and wettability of the as deposited Al/Al$_2$O$_3$ coatings.
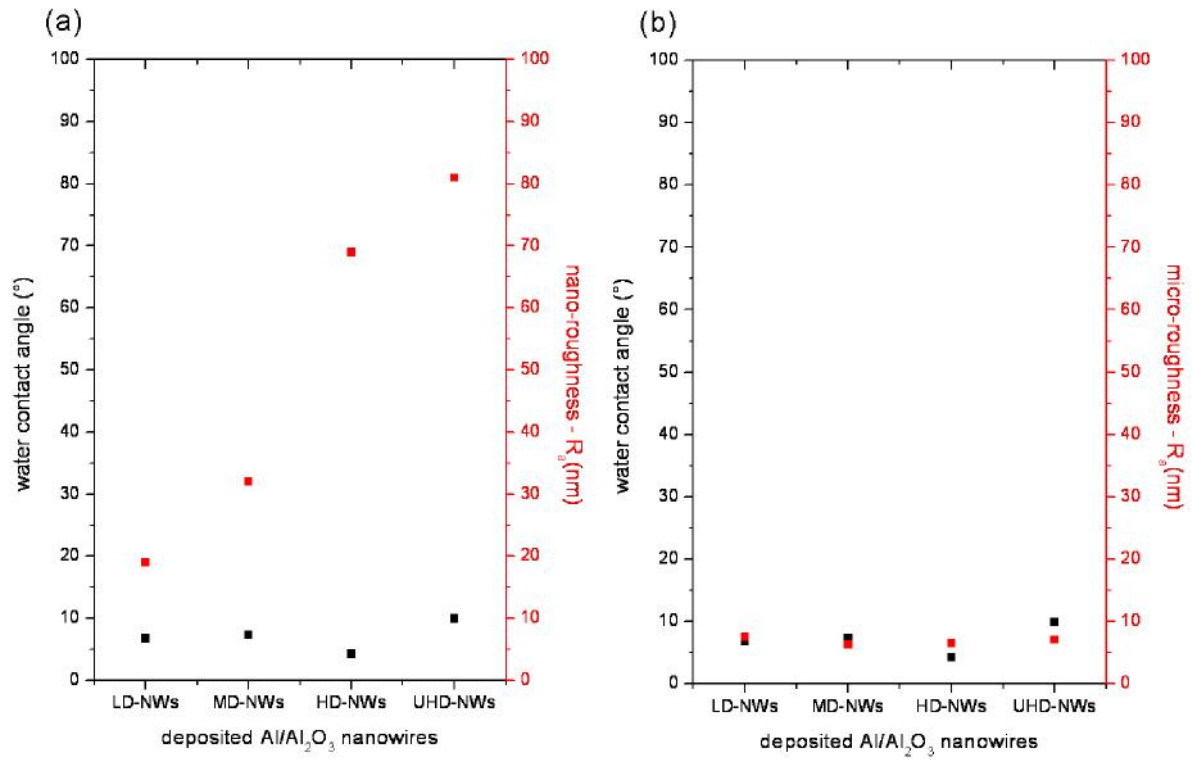
Figure 4.51: Correlation between water contact angle and roughness (R$_a$) depending on the deposited Al/Al$_2$O$_3$ nanostructure for (a) nano-roughness and (b) micro-roughness.

5

Interactions of Cells with Al/Al$_2$O$_3$ NWs Prepared by CVD

For several decades alumina ceramics have been used for implants and prostheses because of its excellent biocompatibility, good mechanical properties and log-term durability[169]. The surface topography of alumina implants has been reported to be a key factor when enhancing the implant performance[159]. In this context, Price et al. reported that modified surfaces have a higher early level of cell attachment than untreated alumina surfaces[27]. Understanding how the cells interact with the materials is of high importance in areas such as biomaterials and tissue engineering, however, such event is still not clear. A lot of factors on both, cellular and material sides influence these interactions and must be controlled systematically during the experiments.

In this chapter cell interaction of human osteoblasts (HOB) and normal dermal human fibroblast (NHDF) with the previously defined 1D Al/Al$_2$O$_3$ nanostructures is studied. A general introduction is given paying special attention to the mechanisms involved in cell-surface interactions. It is presented a background of biocompatibility studies on alumina surfaces, either from other groups working with alumina, and from the Al/Al$_2$O$_3$ NWs synthesised in the AK Veith. The behaviour of osteoblast and fibroblast cells after culture on the four synthesised Al/Al$_2$O$_3$ densities of nanowires is investigated. In order to give to the implant material an advantage over current implants, a selective adhesion of cells during the initial stages of cellular interaction is an option. For this purpose, more osteoblast and less fibroblast adhesion are required. Additionally, the effect of surface topography on changes in osteogenic gene expression of osteoblast was investigated. Such analysis may provide information into the regulatory mechanisms behind bone formation at the bone-implant interface. Last but not least, "Cell Monolayer Rheology" (CMR) technique was used in order to determine cell-mechanical properties of fibroblast cells cultured on our prepared Al/Al$_2$O$_3$ NWs.

5.1 Introduction

5.1.1 Interactions between an implant and a host tissue

The main factors influencing the interactions between an implant material and the host tissue are shown in figure 5.1.
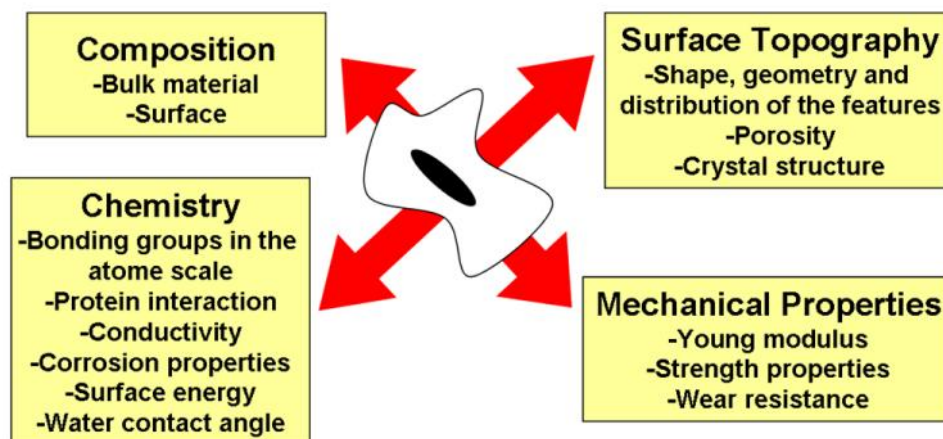
Figure 5.1: Factors that influence the interactions between an implant and a host tissue.

The composition of the bulk material and the surface is of great importance because it influences the cell viability[170]. Some components of biomaterials may be toxic on cells or cause allergic reactions creating problems on the implant[171]. In this work, the studied coatings are made of Al/Al$_2$O$_3$, which is an inert material and does not create the mentioned reactions. Chemistry also plays a key role. The chemical interaction by bonding in the atome scale is of great importance during protein adsorption. The corrosion properties decide weather components of the bulk material are released in the surrounding tissue. The isoelectrical point and the charge distribution on the surface influence the outcome of protein interactions. Surface energy and the contact angle with water influence the spreading of the cells on the surface through protein adsorption[172].

Another key set of parameters is the topography of an implant. In this work a special emphasis is given to the topography. The parameters related with topography influence nearly all steps of biological interaction with an implant surface including protein adsorption, thrombogenicity, cell recognition, adhesion and ingrowth of cells and tissue components in the surface topographies. The surface topography is one of the most important fields for nanotechnology to create biomimetic implants. In a sintered implant or an implant surface the porosity is a key parameter to receive an ingrowth of bone material in the surface. In this work, not only the total porosity has been calculated but also how the porosity and interspacing distribution changes through the coatings (chapter 4).

Finally, the mechanical properties derive from the crystal structure and grain size of metallic and ceramic biomaterials but have not been analysed in detail in this work[172].

5.1.2 Interface between the biomaterial and the biological system: mechanisms involved in cell-surface interactions

Tissue forming cells adhere to an extracellular matrix (ECM) in organs. In bone tissue, bone forming osteoblasts and bone degrading osteoclasts adhere and grow on extracellular matrix composed of proteins and proteoglycans associated with calcium phosphate minerals. 90 % of these proteins are collagen and 10 % other proteins[173]. *In vitro*, these cells can survive only if they can adhere to a surface and thus only after this adhesion is achieved they can grow and differentiate. *In vitro*, as well as *in vivo*, the first interaction between the cell and the surface will determine the quality of the cell-implant and tissue-implant interfaces. A few milliseconds after the surface contacts with the biological fluids e.g. cell culture medium, interstitial fluids or blood, a biolayer consisting of water, proteins and other biomolecules from the physiological liquids are formed on the material surface. Due to stimulation by cytokines and growth factors in the biolayer the cells from the surrounding tissue immediately migrate to the area around the implant. Through this biolayer the interaction between implant surface and the cells is mediated. The implanted biomaterial contacts different proteins containing biological fluids, cells, and tissue, which change over the time (Vroman-effect)[174] as the contact time proceeds (figure 5.2). The questions, which decide the outcome of the implantation, are the kind of interacting components and the way of interaction[173]. Patient specific influence like bone quality (osteoporosis) or concomitant diseases (diabetes) also play a big role.
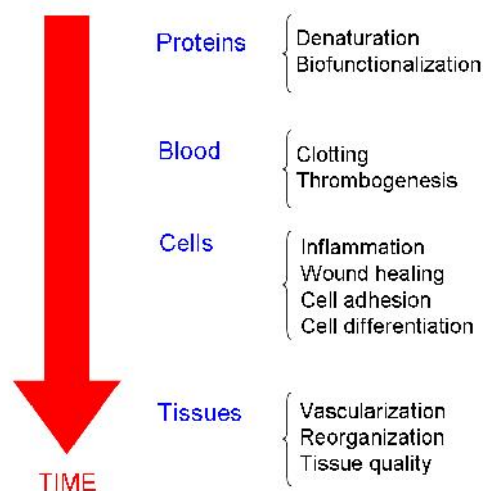
Figure 5.2: Behaviour of biological systems interacting with a biomaterial after implantation (adapted from[172]).

The first component that contacts the material is water. In this contact, orientation of the water molecules and the interaction strength with a material influence the conformation of the proteins which arrive later. It is important that the proteins remain in their native conformation to keep their functionality and avoid defense reactions of the immune system[174].

Integrins are the transmembrane molecules, which mediate the interactions with the extracellular matrix. These molecules are the cells surface receptors and are of high importance. Integrins are heterodimers that consist of one alpha and one beta subunit that can be combined to form receptors specific for amino-acid sequences such as the arginine-glycine-aspartie sequence (RGD) recognition motif present in many extracellular matrix proteins[175].

5.1.3 Protein interaction with a biomaterial

The properties of the substrate and the biomolecule are determinant during the interaction of proteins with biomaterials. In this context, the protein properties that affect this interaction are size, charge, structure and structural stability. Concerning the biomaterial properties, topography, charge and charge distribution as well as chemical composition influence the protein adsorption. The initial protein interactions might lead to cell recognition of an implant. For this reason many investigators are paying close attention to manipulation of initial protein adsorption events[172]. In this context, the proteins that are recognized from cells and to which cells react with a specific bonding are collagen fibres and other adhesion molecules. The proteins that direct cell differentiation and maturation towards physiological tissue remodelling are growth factors. In the frame of this work it is important to highlight that the diameter size of some of the proteins involved in the wound healing are nanoscaled. As shown in table 5.1 the size of the proteins interacting with biomaterials ranges between 1 nm and 500 nm, which means that some of them are small enough to flow through the Al/Al$_2$O$_3$ NWs[172].

Table 5.1 Size of chosen proteins interacting with biomaterials

Protein	Fibre diameter [nm]
Albumin	7
Collagen molecules	1
Collagen fibers	150 - 500 (depending on Cell Type)
Fibrin	300
Fibronectin	2-3
Elastin	12

5.1.4 Bone composition and formation

It is well known that bone is a connective tissue, which forms the skeleton of most vertebrates, protects and supports the internal organs and provides attachment for muscles. It is a uniquely designed composite of complex mineral within a soft organic matrix. About 20-30 % (by weight) of cortical bone is organic, 10 % is water and the rest is composed of minerals. The organic matrix consists of various nonocollagenous proteins mostly glycoproteins (osteocalcin, alkaline phosphatase, osteonectin, fibronectin, thrombospondin, vitronectin, bone sialoprotein) and proteoglycans (decorin and biblycan) [176]. Nevertheless, collagen is the most important bone protein. Phosphate and calcium are the most found minerals, but there are other minerals like citrate, carbonate, magnesium, sodium, fluoride, hydroxyl and other ions. Bone mineral consists of a microcrystalline and structurally imperfect structure of hydroxyapatite (HA)(Ca$_{10}$ (PO$_4$)$_6$(OH)$_2$) which provides the bone the capacity of being a reactive material which satisfies the need of normal resorption, redisposition as well as the growth and the repair[177].

Concerning the bone formation, two primary processes occur; intermembranous and endochondral processes[178]. The first one takes place in the craniofacial bones, while in the rest of bones the second one occurs. In the intermembranous bone formation process mesenchymal cells condense and differentiate directly into osteoblasts, while in the endochondral bone formation process mesenchymal cells condense to form a cartilage matrix. This cartilage matrix will be afterwards like a scaffold for the osteoblast invasion.

There are different cell types associated with the bone[179] and especially three of them; osteoblasts, osteocytes and osteoclasts have important roles in the bone formation. In both processes of bone formation (intermembranous and endochondral), osteoblasts are responsible for bone matrix (osteoid) deposition. Osteoblast cells are categorized in a presumed linear sequence progressing from osteoprogenitors to pre-osteoblasts to osteoblasts and finally to osteocytes[180]. The osteoblast becomes an osteocyte when this is surrounded by bone matrix. The function of osteocytes is not clearly established but they are possibly responsible for the exchange of ions with the bone matrix and the rapid release of calcium and phosphorous from mineralized bone. These cells have the capacity not only to synthesize, but also to resorb matrix to a limited extent[179].

5.1.5 Background of biocompatibility studies on nanostructured alumina

Alumina micro fibres have been used for mechanical applications since 1980s. Especially, alumina-whiskers- reinforced ceramic, metal and polymer composites are accepted as structural materials for high performance applications due to their excellent properties, such as low density, high strength and toughness. It is known that alumina fibres have a high melting point, high strength, light weight and good wear resistances[181]. In order to increase the flexibility, strength and high temperature resistance of the matrix material, such fibres were added to ceramics, metals and polymers to obtain ceramic matrix composites, metal matrix composites and polymer matrix composites respectively. Several methods have been used to produce such fibres, for instance different sol-gel and colloidal synthesis. In these approaches the main problem was the control of size, shape and porosity within the fibre or whisker. Alumina is also extensively used as template for synthesising of 1D nano and micro structures. Anodic porous alumina is an ideal template for the controlled fabrication of nanostructures beyond the limit of the current lithographic techniques. Porous alumina has been used as a template to synthesize carbon nanotubes[182]. In the other way around, carbon nanotubes were used as templates to prepare different types of nanotubes of nanowires of Al$_2$O$_3$ [20]. The use of a porous anodic alumina membrane with ordered nanopores is known as one of the simplest methods to generate 1D Al$_2$O$_3$ nanostructures[21]. Other methods are also developed to synthesize 1D Al$_2$O$_3$ and metal-Al$_2$O$_3$ composite structures for instance lithography based top-down processes and bottom-up chemical approaches such as for instance thermal evaporation, catalyst supported CVD or carbothermal reactions.

5.1.6 Background of biocompatibility studies on surfaces prepared by CVD of [^{t}BuOAlH$_2$]$_2$

During the last years several students and researchers from Prof. Veith group studied the cell compatibility of the surfaces prepared by CVD of [^{t}BuOAlH$_2$]$_2$ for diverse biological applications.
Petersen reported the first biocompatibility studies on the Al/Al$_2$O$_3$ 1D nanostrucutures in his doctoral thesis under the supervision of Prof. Veith[183]. Two different materials were synthesized in terms of morphology and composition: micro hill-like HAlO and Al/Al$_2$O$_3$ NWs. Whereas fibroblast cells cultured on HAlO showed a similar behaviour to those fibroblast cells cultured on Si-wafers in terms of general cell compatibility, adhesion, proliferation and cell differentiation, fibroblast cell culture on Al/Al$_2$O$_3$ resulted in poor cell adhesion and proliferation[184]. After Petersen, Aktas continued the cell compatibility studies on surfaces prepared by CVD of [^{t}BuOAlH$_2$]$_2$[92]. In his doctoral thesis he conducted a more detailed work on the cell compatibility of the Al/Al$_2$O$_3$ NWs with a better control of the morphology. Firstly, his main intention was given to the morphology and topography

effects on the cell interaction without a chemical surface modification. Different types of cells including cell lines and primary cells were employed to understand if the responses of the cells are specific for one cell type or not. In addition to basic fibrous Al/Al$_2$O$_3$ structures, different morphologies prepared by the laser treatment of Al/Al$_2$O$_3$ NWs were tested in terms of the cell compatibility. Depending on the laser intensity and pulse numbers various structures composed of both nano and micro features were produced.

Veith et al. reported a study about the adhesion of fibroblasts on micro- and nanostructured surfaces prepared by chemical vapour deposition and pulsed laser treatment [185]. The goal of that work was to develop a biocompatible Al$_2$O$_3$-surface which could be used as a coating material for medical implants exhibiting a cell selective response because of its specific physical landscape and especially because it promotes the adhesion of osteoblasts while minimizing the adhesion of fibroblasts. It was observed that while the cells cultivated on Al/Al$_2$O$_3$ bi-phasic nanowires showed an unusual morphology, cells cultivated on nanowires treated with one and two laser pulses exhibited morphologies similar to those observed on the control substrate. The cell compatibility of osteoblast on Al/Al$_2$O$_3$ NWs was not shown.

In this context, the present work is a step forward on the research lines which have been already introduced. In this thesis a detailed work is conducted on the selective adhesion of osteoblast and fibroblast cells on Al/Al$_2$O$_3$ NWs for possible bone implant applications. For the first time, the cell compatibility of the Al/Al$_2$O$_3$ NWs with osteoblast cells is here studied. The determination of cell compatibility in *in vitro* cell culture experiments was done in the department of trauma, hand and reconstructive surgery of Saarland University. In addition to cell culture analysis, a qRT-PCR (quantitative real-time polymerase chain reaction) analysis of osteogenic gene expression during cultivation on the different Al/Al$_2$O$_3$ NWs has been studied in collaboration with the department of trauma, hand and reconstructive surgery and the AO foundation and the AO Research Institute Davos in Switzerland for the very first time on Al/Al$_2$O$_3$ NWs. Increasing osteoblast adsorption and human osteoblast (HOB) osteogenic differentiation would lead to a better and faster osseointegration. Last but not least, the rheological properties of fibroblast cells were studied using the "cell monolayer rheology" (CMR) technique with the aim to understand the cell-mechanical properties. The rheology experiments have been performed in the Biological Experimental Physics department of Saarland University.

Al/Al$_2$O$_3$ NWs were also studied for other biological applications. Lee focused his master thesis on the study of neuronal growth on Al/Al$_2$O$_3$ NWs. We reported a preliminary study on neurons which showed that 1D Al/Al$_2$O$_3$ nanostructures provide an enhanced cellular adhesion and growth. In addition such 1D Al/Al$_2$O$_3$ nanostructures can be used to study the cellular communication and neural signalling[186]. Lately, Lee et al. reported new results about cell alligment on Al/Al$_2$O$_3$ NWs treated by laser interference lithography technique (LIL). Regular patterns were created on the Al/Al$_2$O$_3$ coatings. We showed that axons of dorsal root ganglion (DRG) neurons grew along the direction of the patterned Al/Al$_2$O$_3$ NWs while they showed random outgrowth on non-patterned Al/Al$_2$O$_3$ NWs. The morphology of smooth muscle cells changed drastically from poly- to linear shapes and strong alignment was observed on the patterned Al/Al$_2$O$_3$ NWs while endothelial and osteoblast cells showed similar behaviour on both surfaces. Our results demonstrated that the topography effect on the cell guidance is independent from the surface chemistry[187].

Last year our group reported an approach to improve the material design for stent coatings through the selective adhesion between human umbilical vein endothelial cells (HUVEC) and human umbilical vein smooth muscle cells (HUVSMC) [188]. In that work we investigated the effect of the micro and nanotopography on vascular cell-surface interaction using nano and microstructured Al$_2$O$_3$ as model substrate. A clear diverging response of endothelial and smooth muscle cells was observed on these nano and microstructured surfaces. Low density Al/Al$_2$O$_3$ NWs seem to enhance the proliferation of endothelial cells selectively. In the same context, Aktas et al. reported improved endothelisation on nanostructured Al/Al$_2$O$_3$ surfaces[189]. Lately, Haidar focused his master thesis on highlighting the effect of structured Al/Al$_2$O$_3$ NWs on endothelial and smooth cell behaviour. For that purpose, Al/Al$_2$O$_3$ NWs were treated using laser interference lithography technique forming regular patterns with well-defined dimensions[190]. Haidar observed clear differences in proliferation and morphological behaviour between both cell types on the patterned surfaces: while smooth muscle cells grew chaotically on control glass samples, they were aligned on laser patterned samples following the defined patterned lines. On the other hand highly stretched endothelial cells were observed on the same treated samples. Furthermore proliferation of endothelial cells was favoured over smooth muscle cells on these treated samples.

5.2 Selective adhesion of Osteoblast and Fibroblast on Al/Al$_2$O$_3$ NWs

The aim of this section is to study the different behaviour of osteoblast and fibroblast cells after culturing them on the four Al/Al$_2$O$_3$ nanowire densities presented and characterized in the previous chapters. It would be suitable for use in orthopaedic and dental implants to increase osteoblast

adhesion and decrease fibroblast adhesion in order to minimize the risk of a fibrous encapsulation of an implant followed by micro-movements and finally aseptic loosening. A selective adhesion during the initial stages of cellular interaction may give the material an advantage over current implant materials. More osteoblast and less fibroblast adhesion could lead to faster integration of the bone to the implant surface *in vivo*. The cell experiments of this section were performed by the medical students Benedikt Schwab (osteoblast cells), and Lisa Schimmelpfennig (fibroblast cells) at the department of trauma, hand and reconstructive surgery of Saarland University under the supervision of Dr. Wolfgang Metzger.

5.2.1 Experimental approach

5.2.1.1 Synthesis of Al/Al$_2$O$_3$ NWs

As cells typically have low optical contrast, transmission optical microscopy in the phase contrast mode is normally used for observation. For this reason, glass coverslips ($\emptyset$ = 12 mm, Roth, Germany) were used as substrate in this experiment. Al/Al$_2$O$_3$ NWs were deposited on the glass coverslips following the deposition technique explained in chapter 3. For every density type several samples were fabricated. Taking into account that 2 different types of cells were investigated, the number of samples was doubled. For this experiment an approximate number of 500 samples were produced. The performed experiments for every cell type were: n = 5 (cell density, cell area, fluorescence images), n = 2 (SEM images) and n = 1 (WST-1 test).

5.2.1.2 Cell experiments

Prior to cultivation, all samples were sterilized and incubated. For sterilization, the substrates were rinsed three times with sterile phosphate buffered saline (PBS) and for incubation ethanol (70 volume percent (vol %) was used for at least 20 min. Afterwards, two additional rinsing steps with sterile PBS took place. Human osteoblasts (HOB) derived from a knee biopsy (Promocell, Heidelberg, Germany) were incubated and cultured in Dubelcco´s modified eagle medium (DMEM, PAA, Pasching, Austria), supplemented with 15 % fetal calf serum (FCS, PAA) and 1 % penicillin/streptomycin (P/S) under standard cell culture conditions (37°C, and 5 % CO$_2$/ 95 % air humidification) in culture flasks (Greiner Bio-One, Frickenhausen, Germany). Similarly, normal human dermal fibroblast (NHDF) (Promocell, Heidelberg, Germany) were cultivated in Quantum 333 medium (Q333, PAA-laboratories) in 75 cm^2 tissue flasks (Greiner BioOne) until they reached near-confluence. Q333 does not require the addition of serum because is a complete medium for the culture of fibroblasts. It is supplemented with selected serum components and growth factors. In order to detach the cells from the bottom of the flasks standard cell culture procedures were used using trypsin. A hemocytometer was used to count the cells for standardized seeding. Osteoblast cells

were seeded at a density of 100 cells/mm^2 onto the substrates of interest in multiwell plates (12-well, Greiner, Bio One) and fibroblasts cells at a density of 63 cells/mm^2. The incubation time was 2 days and early adhesion was 6 h for both cell types. The cell morphology and the cell density were imaged by optical phase contrast microscopy daily.

Fluorescence labelling

Due to the opacity of the substrates the cells were stained for visualization. The Cell Tracker^{TM}-dye for living cells was used for staining to visualize cell morphology by fluorescence microscopy. This Cell Tacker^{TM} reagent can be loaded into cells by adding the reagent to the culture medium and then washing the cells briefly with fresh medium before analysis. The reagent passes freely through cell membranes and is encymatically transformed into a cell impermeant fluorescentdye-thioether adduct that can be fixed, permitting long-term sample storage. We used the green fluorescent dye Cell Tracker^{TM} 5-chloromethylfluoresceindiacetate (CMFDA, Invitrogen) with an absorption maximum at 492 nm and an emission maximum at 517 nm. In contrast to other Cell Tracker^{TM} dyes CMFDA is colorless and nonflourescent until the acetate groups are cleaved by intracellular esterases (Fig 5.3).
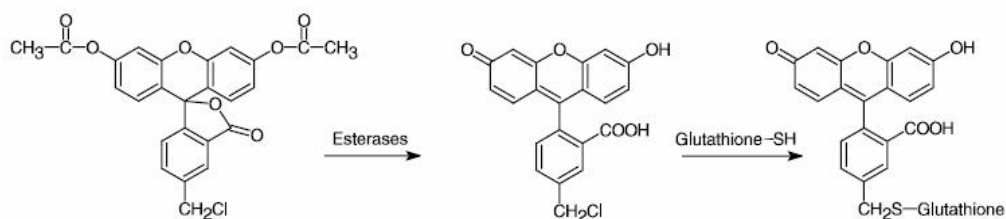
Figure 5.3: Enzymatic cleavage of CMFDA resulting in the fluorescent CellTracker™-dye (Invitrogen)[191].

10nM of a solution of 50 µg of CMFDA dissolved into 10.76 µl dimethylsulfoxide (DMSO) were stored at -20°C until the staining procedure. A 2.5 µM working dilution was obtained by dilution in serum-free DMEM. The cells were washed with PBS (37°C) one time after removing the medium. In every well 2 ml of staining medium were used. Osteoblast and fibroblast cells were incubated for 30 min at 37°C. After removing the staining mediums, osteoblasts and fibroblasts were rinsed twice with PBS. Fresh culture medium was added followed by a second incubation at 37°C for 30 min. The fixation was done by incubation in ice cold methanol (-20°C) for at least 10 min. The substrates were dried with air and fixed on standard microscopic slides in order to facilitate the microscopic analysis. Osteoblasts and fibroblast cells were covered with mounting medium containing 4',6-diamidino-2-phenylindole (DAPI) for nuclear counterstaining (Vectashield, Vector Laboratories). The slides were stored until the microscopic analysis at 4°C.

WST (Water soluble tetrazolium) – 1 test

In order to analyse the overall metabolic activity of the cells growing on the Al/Al$_2$O$_3$ coatings the WST-1 test (Roche, Mannheim, Germany) was performed. Proliferation and viability were obtained. The principle of the test is the conversion of the WST-1 tetrazolium salt by cellular enzymes to the dark red formazan, which absorbs light between 420 and 480 nm. The medium was removed and 1.5 ml of the WST-1 medium (DMEM: WST-1 solution = 10:1) were added. Afterwards the cells were incubated for 4 h under standard cell culture conditions. The cell culture experiment was performed three times. The supernatants were mixed and 100 µl were transferred to 96 well plates. The absorption (λ = 434 nm) was measured against a negative control using a TECAN Infinite®M200 microplate reader (Tecan Group Ltd, Männedorf, Suisse). Seeding densities and incubation times in WST varied between oseoblasts and fibroblasts.
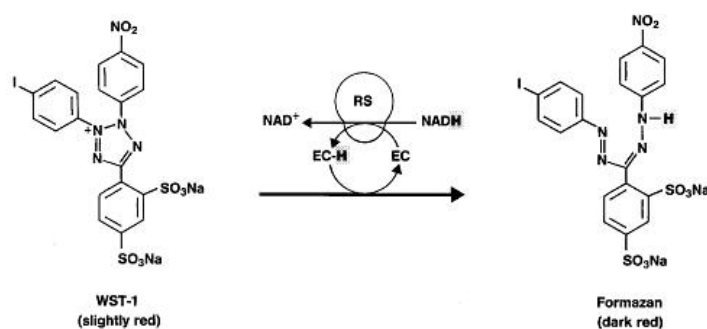
Figure 5.4: WST-1 principle[192].

5.2.1.3 Microscopic analysis of the cells

An Axioskop microscope (Carl Zeiss, Jena, Germany) with the Axiovision software were used for microscopic analysis. The measuring module of the Axiovision software was used to determine the number of nuclei and the overall cell area determined automatically in 10 visual fields. Cell density and cell area results were tested in terms of significance ($p < 0.05$) by applying a one-way repeated measurement ANOVA with post-hoc analysis (Holm-Sidak).

Fixation and labelling of the cells for SEM analysis

Osteoblast and fibroblast cells were cultivated on the substrates as described previously. The cell culture medium was removed rinsing the substrates twice with PBS (37°C). For fixation 2 % glutardialdehyde in 0.15 M cacodylate buffer at RT (room temperature) under movement (2 x 30 min) was used. After fixation the samples were incubated in osmium tetroxide (1 % in 0.2 cacodylate buffer) for 1h under movement in the dark at RT to increase the contrast. Afterwards, the substrates

were rinsed 3 times with dH$_2$O at RT. The substrates were washed twice in an ethanol series under movement at 4°C for 2 x 5 min (30 %, 50 %, 70 %, 80 % and 90 %) for water removal. Dehydrating procedure was finished by washing twice in ethanol (100 %) for 10 min under movement at 4°C. After dehydratation the samples were dried by Critical-Point-Drying (Polaron CPD 7501, Quorom Technologies) and were sputtered with gold-palladium (Polaron, Sputte rCoater). The analysis was performed in a FEI XL 30 ESEM FEG SEM device (Hilsboro).

5.2.2 Results and discussion

5.2.2.1 Cell fluorescence images

It is known that osteoblast cells are attachment-dependent cells[4], which means that before producing and mineralizing their extracellular matrix they must attach to the surface. Attachment, in the cell culture context, indicates how many cells are adhering to the surface with respect to the number of cells that had the opportunity to attach. On the other hand, adhesion refers to the relative strength of the attachment. It gives an idea about how difficult it is to dislodge the cell from the surface. In this context, the fluorescence images shown in this section give us an idea about the late adhesion (48 h) of fibroblast and osteoblast cells on glass and on all the Al/Al$_2$O$_3$ nanowire densities. In figure 5.5 it is observed that the tendency of cells to adhere on the control (glass) after 48h is similar for both cell types. A similar density of fibroblast (figure 5.5a) and osteoblast (figure 5.5b) cells is observed.
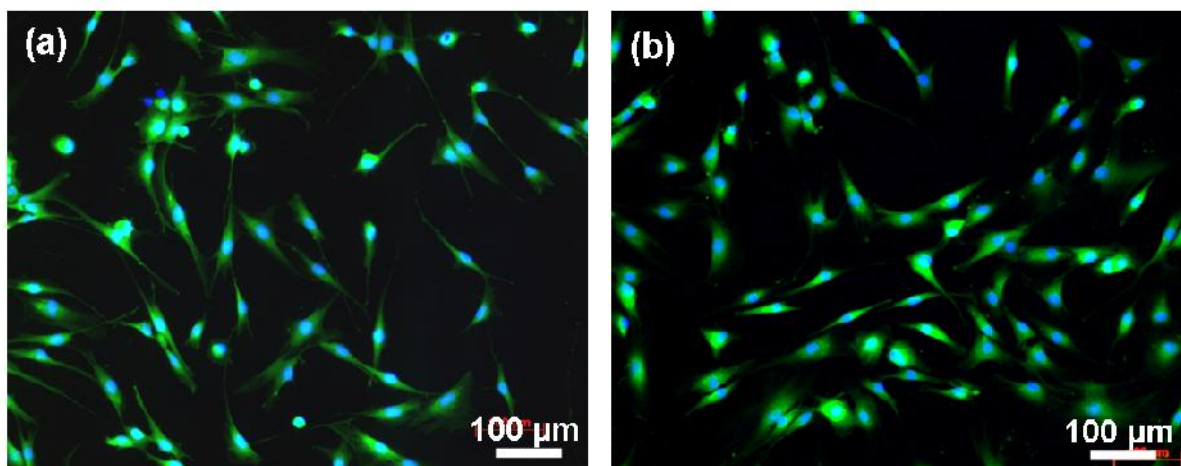
Figure 5.5: Fluorescence images after staining (48h) of (a) fibroblast (NHDF) and (b) osteoblast (HOB) cells cultured on glass.

Figure 5.6 shows fibroblast (figure 5.6a) and osteoblast cells (figure 5.6b) cultured on the less densely coated Al/Al$_2$O$_3$ nanostructure (LD-NWs). In this case small differences are appreciated. It is observed that the number of osteoblast cells is slightly higher than fibroblast cells. Additionally, the osteoblast cells seem to build more cell-cell interactions (red arrows) between them than on the control. Some

cell accumulations are also observed. It can be also seen that the amount of fibroblast cells seem to be less than in on the glass control.
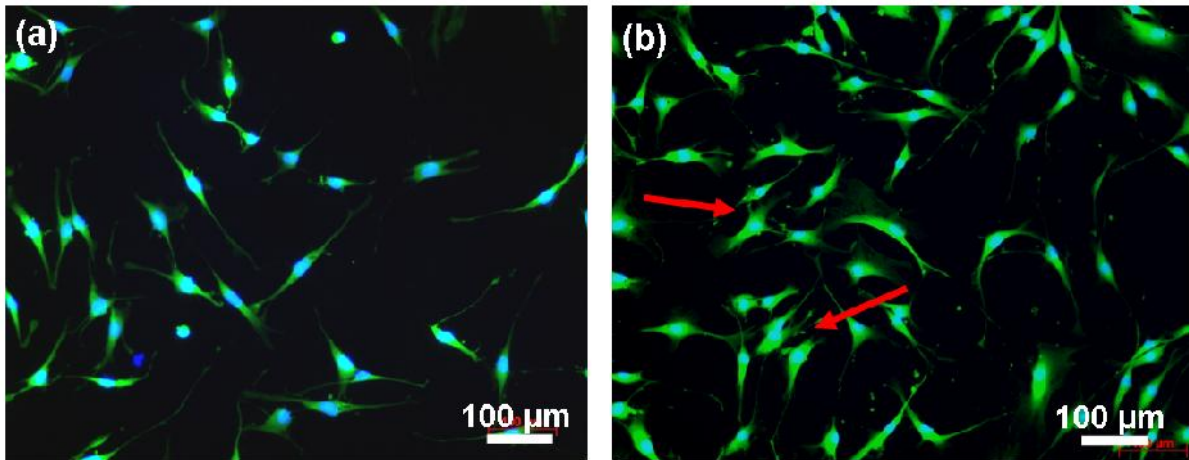
Figure 5.6: Fluorescence images after staining (48h) of (a) fibroblast (NHDF) and (b) osteoblast (HOB) cells cultured on LD deposited Al/Al$_2$O$_3$ NWs.

In figure 5.7a a tendency is observed: the amount of fibroblast cells cultured on MD Al/Al$_2$O$_3$ NWs is less than on the glass control. The number of osteoblast nuclei detected after late adhesion (figure 5.7b) is slightly higher compared to the amount of fibroblast nuclei. Nevertheless, not a big difference is observed between the two cell types.

Figure 5.7: Fluorescence images after staining (48h) of (a) fibroblast (NHDF) and (b) osteoblast (HOB) cells cultured on MD deposited Al/Al$_2$O$_3$ NWs.

As the density of the Al/Al$_2$O$_3$ NWs increases, notable differences are observed concerning cell adhesion. While no big differences were observed on the control, LD-NWs or MD-NWs Al/Al$_2$O$_3$ NWs, a different behaviour is observed on the denser Al/Al$_2$O$_3$ nanostrucures (HD-NWs and UHD-NWs): Figure 5.8 shows clearly how a very high amount of osteoblast cells adhere on the HD-NWs (figure 5.8b). The osteoblast cells are denser than on MD NWs, LD NWs and even glass. The amount of

osteoblast cells found on HD-NWs is higher than the amount of fibroblast cells observed on the same sample type (figure 5.8a). Compared to MD-NWs, LD-NWs and glass a bad fibroblast adhesion is detected. In figure 5.8c it is observed how the morphology of the fibroblast cells is unusuall. The cells seem to be "structured", the nuclei shape is not round and the cells appear to be more disrupted. Another highlight is the fact that the amount of cell-cell interactions is very high in case of osteoblast cells. In figure 5.8d some cell-cell interactions can be appreciated (red arrows). The same behaviour was observed on UHD-NWs. Figure 5.9 shows the amounts of osteoblast cells adhered to the UHD-NWs coating is much bigger than the amount of fibroblasts cells adhered to the same coating.

To sum up:

→ A clear tendency is observed in the fluorescence images. **The amount of <u>osteoblast</u> cells adhered to the substrate increases as the substrates are more densely coated**. In all cases the amount of osteoblast cells detected is the same or even higher compared to the glass control. **On the other hand, the amount of <u>fibroblast</u> cells adhered to the substrate decreases as the Al/Al$_2$O$_3$ nanowire density increases**. In the densest coatings the amount of fibroblast adhering to the substrate is even less than on the glass control. Strictly, quantitative analyses can not be done only with the fluorescence images, therefore, these tendencies will be confirmed with the cell density analyses.
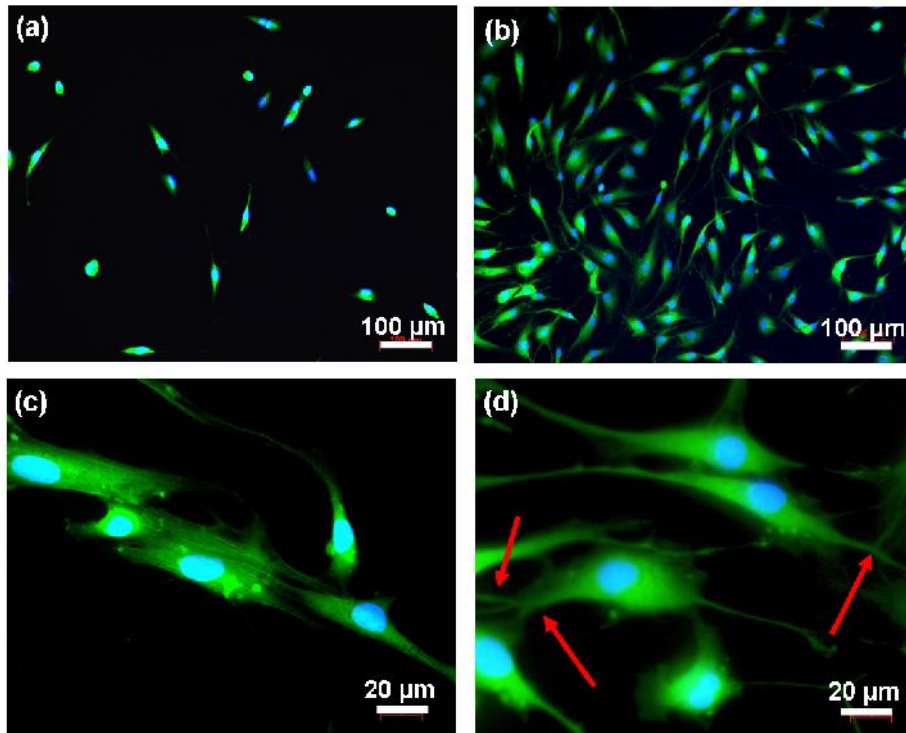
Figure 5.8: Fluorescence images after staining (48h) of (a, c) fibroblast (NHDF) and (b, d) osteoblast (HOB) cells cultured on HD deposited Al/Al$_2$O$_3$ NWs.
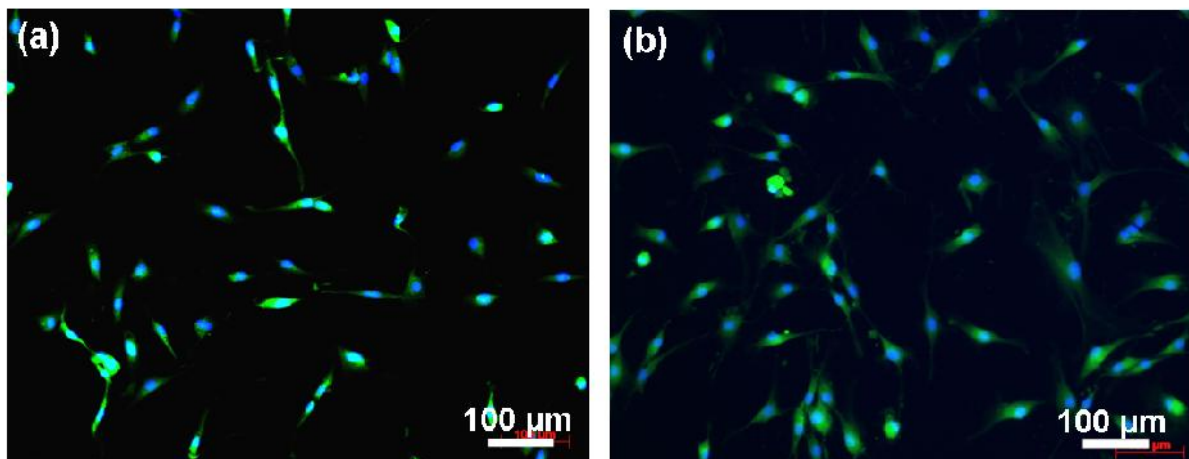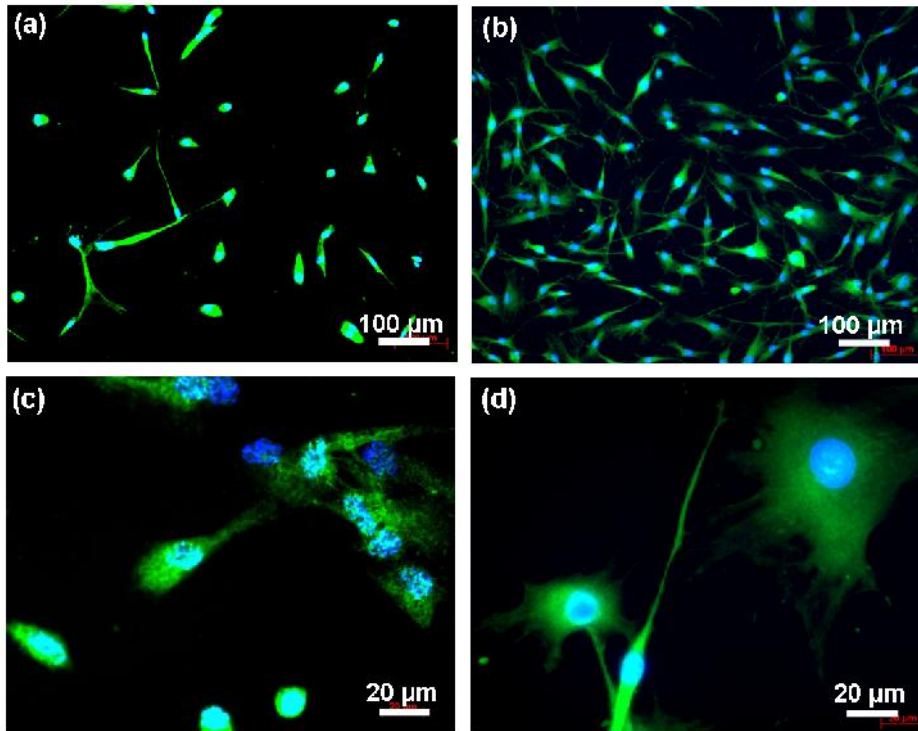
Figure 5.9: Fluorescence images after staining (48h) of (a, c) fibroblast (NHDF) and (b, d) osteoblast (HOB) cells cultured on UHD deposited Al/Al$_2$O$_3$ NWs.

5.2.2.2 Morphology analysis of the cells by SEM

For a better understanding of the cell – surface interaction, SEM was used for visualization of the behaviour of the seeded fibroblasts and osteoblasts on the different deposited Al/Al$_2$O$_3$ nanostructures. After the cells attach to the surface they may spread to a greater or lesser extent. Boyan and colleagues pointed out that a well-spread cell is assumed to be well adapted to culture[4]. In the SEM images shown in figure 5.10 to figure 5.20 spreading as well as shape and morphology of the cultured osteoblast and fibroblast cells is observed for glass (control), LD-NWs, MD-NWs, HD-NWs and UHD-NWs. Figure 5.10 shows that both cells are well spread on glass. The typical morphologies of fibroblast cells (figure 5.10a) and osteoblast cells (figure 5.10b) are observed on the glass substrate used as control. Fibroblast cells show a flatter morphology than osteoblast cells and a numerous filopodia are formed in both cases.
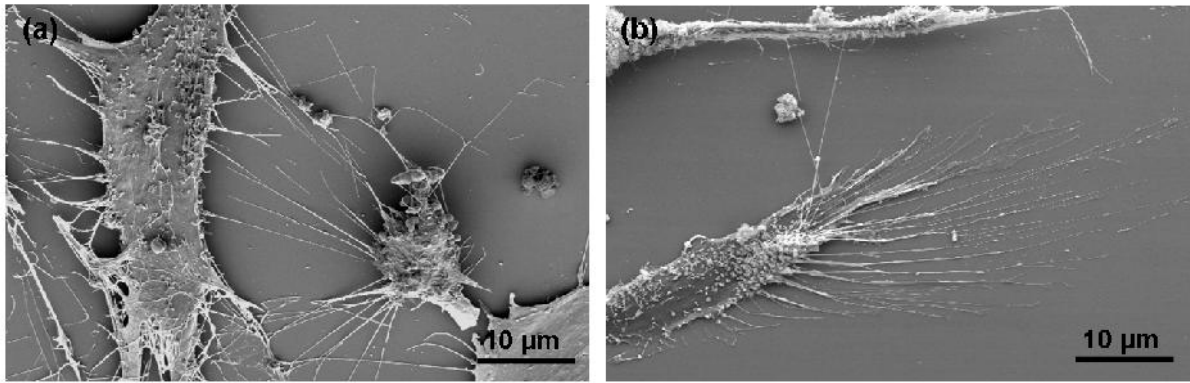
Figure 5.10: SEM images of (a) fibroblast and (b) osteoblast cells seeded on glass.

In case of LD-NWs surfaces (figure 5.11) the behaviour of both cells is similar to the control. Fibroblast as well as osteoblast cells try to adhere to the LD-NWs. A small difference is observed on the fibroblast behaviour. In figure 5.11 is observed that the fibroblast cells are more contracted than the observed fibroblast cells cultured on glass.
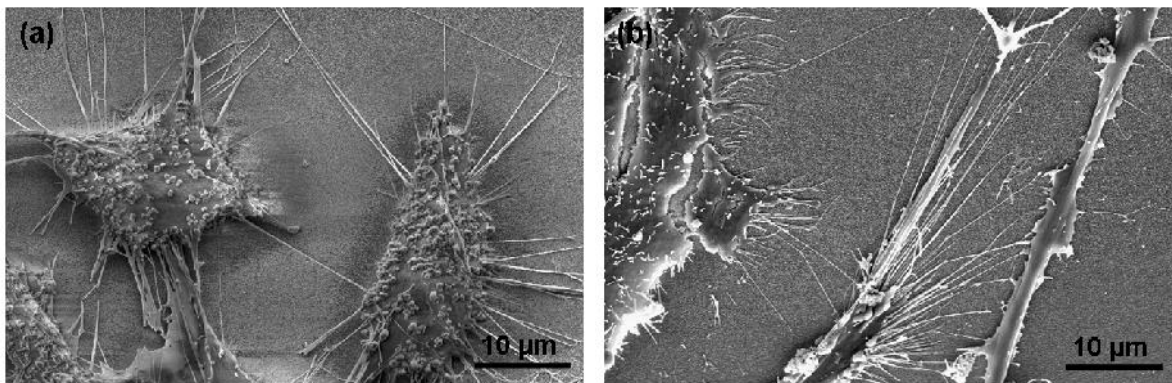
Figure 5.11: SEM images corresponding to (a) fibroblast and (b) osteoblast cells seeded on LD-Al/Al$_2$O$_3$ NWs.

The SEM images corresponding to fibroblast and osteoblast cells cultured on MD-NWs reveal a key difference. It is observed in figure 5.12a that the amount of filopodia from the fibroblast cells trying to anchor and to explore the substrate is less than in the previous samples (LD-NWs and glass). The amount of filopodia from the fibroblast cells is also fewer than the amount of osteoblast filopodia observed on the same sample type (figure 5.12b).
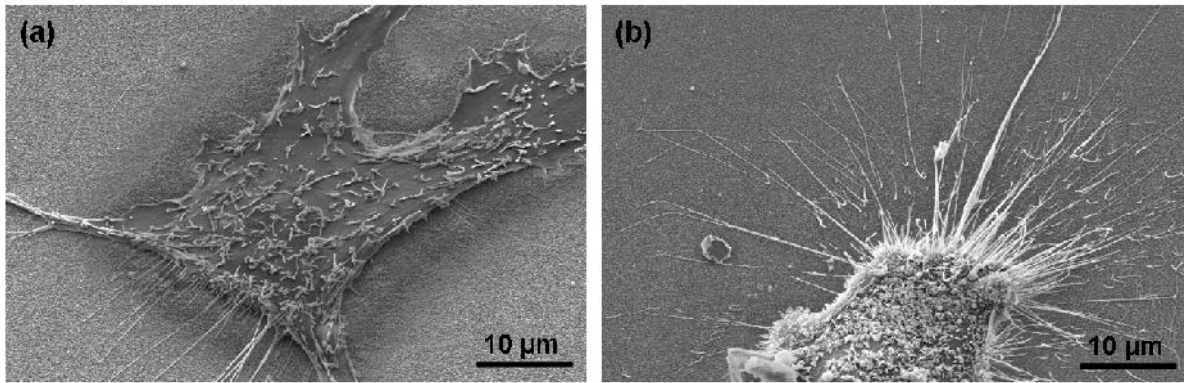
Figure 5.12: SEM images corresponding to (a) fibroblast and (b) osteoblast cells seeded on MD-Al/Al$_2$O$_3$ NWs.

The most important differences between both cells, concerning cell morphology, are detected on HD-NWs and UHD-NWs. **It is observed that on HD-NWs and UHD-NWs <u>fibroblast</u> cells changed drastically their morphology**. The cells are contracted and elongated and no filopodia are observed. As a consequence of spreading absence the cell area is diminished. Therefore, the cells are not growing well on the surface (figure 5.13a and 5.14a). In case of osteoblast cells less filopodia are observed on HD-NWs and UHD-NWs than on the rest of samples, nevertheless the cells still look flat, spread and maintain their shape and area (figure 5.13b and 5.14b).
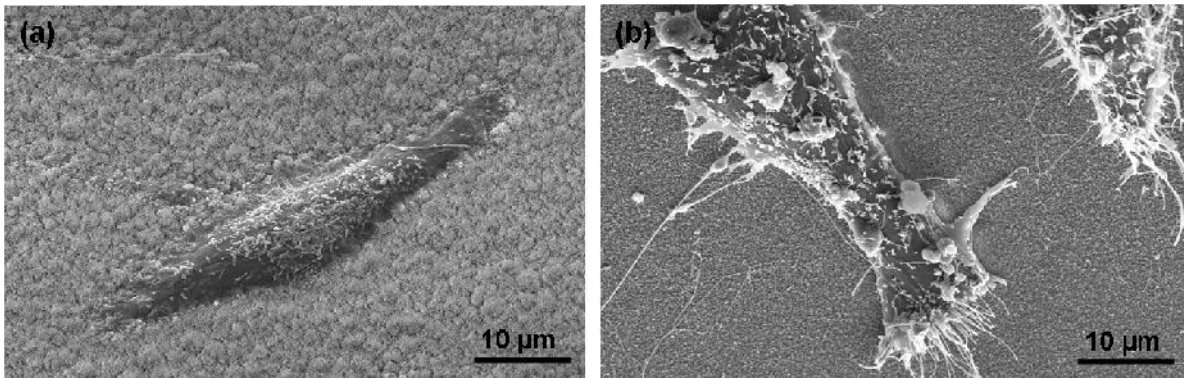
Figure 5.13: SEM images corresponding to (a) fibroblast and (b) osteoblast cells seeded on HD-Al/Al$_2$O$_3$ NWs.
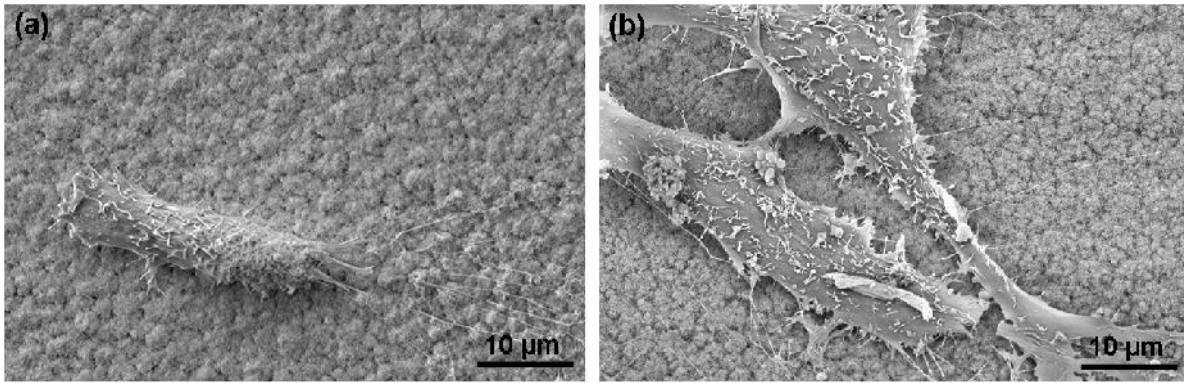
Figure 5.14: SEM images corresponding to (a) fibroblast and (b) osteoblast cells seeded on UHD-Al/Al$_2$O$_3$ NWs.

Figures 5.15 to 5.19 show SEM images taken at higher magnification. It has been observed that in case of HD-NWs and UHD-NWs some elongated protrusions are detected on the fibroblast cells. One hypothesis is that these protrusions could be blebs. In cell biology, blebs are irregular bulges in the plasma membrane of a cell caused by localized decoupling of the cytoskeleton from the plasma membrane[193]. During apoptosis (programmed cell death), the cell's cytoskeleton breaks up and causes the membrane to bulge outward[194]. These bulges may separate from the cell, taking a portion of cytoplasm with them, to become apoptotic bodies. Nevertheless, it cannot be confirmed with SEM images that the observed protrusions are blebs therefore apoptotic bodies are not confirmed. On the other hand, **the absence of filopodia observed on HD-NWs and UHD-NWs confirms that fibroblast cells do not grow in optimum conditions on the mentioned substrates**.

In case of osteoblast cells also some protrusions are observed on the cells cultured on MD-NWs, nevertheless, a big amount of filopodia is detected which leads us to the conclusion that the cell adheres to the surface. Although osteoblast cells on HD-NWs and UHD-NWs developed less filopodia than on the other sample types and the control, they preserved their shape and flattened on the surface. All this leads us to conclude that although no optimum cell morphology is observed on the osteoblast cells on HD-NWs and UHD-NWs, they still are able to adhere to the surface, while in case of fibroblast the cells are more sensitive and chance for cell adhesion is less.

All in all:

→ **It has been observed that as the nanowire density increases, the <u>fibroblast</u> morphology change drastically while the <u>osteoblast</u> morphology changes in a fewer degree.** While fibroblast cells seeded on HD-NWs and UHD-NWs showed anomalies, osteoblast cells still keep a similar morphology than that one observed on the control.
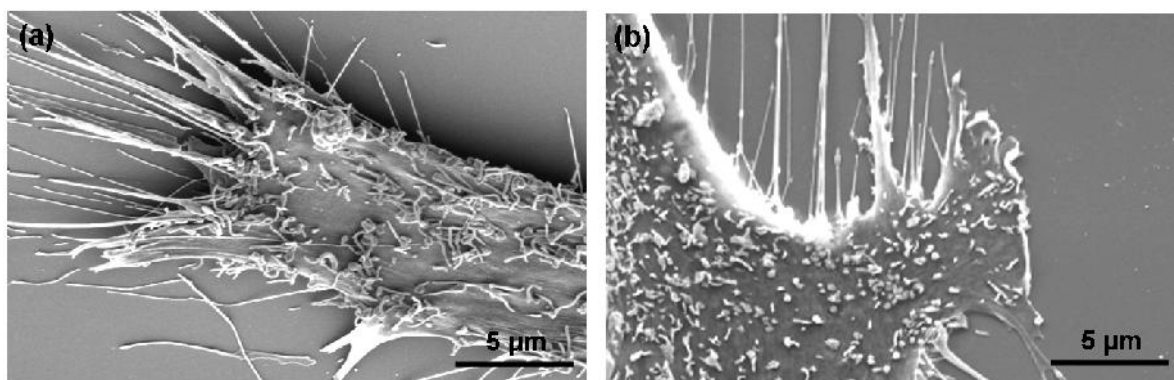
Figure 5.15: High magnification SEM images corresponding to (a) fibroblast and (b) osteoblast cells seeded on glass.
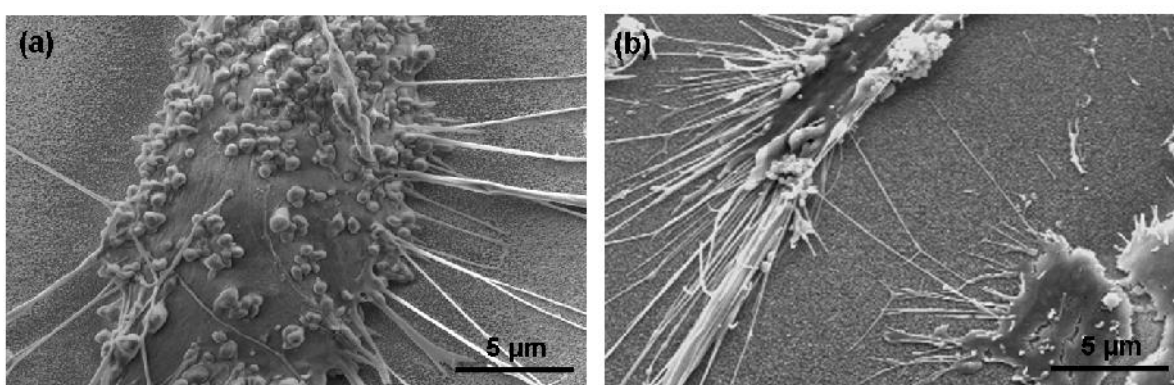
Figure 5.16: High magnification SEM images corresponding to (a) fibroblast and (b) osteoblast cells seeded on LD-Al/Al$_2$O$_3$ NWs.
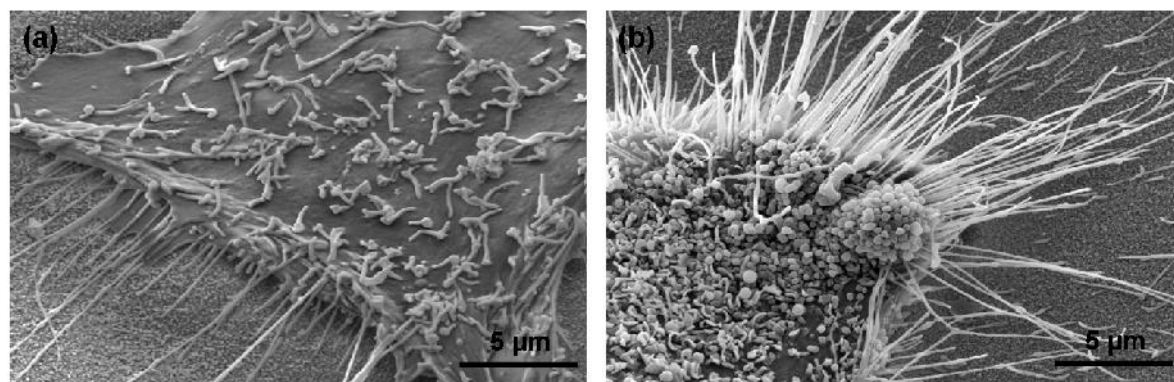
Figure 5.17: High magnification SEM images corresponding to (a) fibroblast and (b) osteoblast cells seeded on MD-Al/Al$_2$O$_3$ NWs.
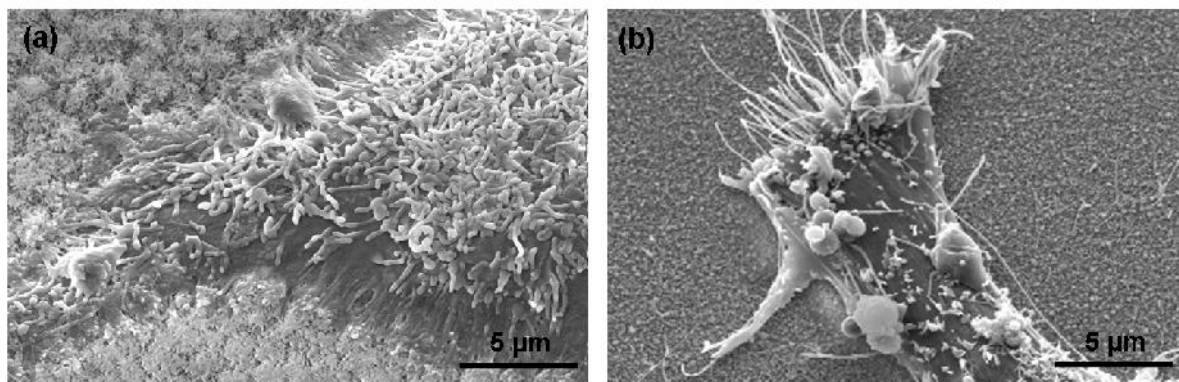
Figure 5.18: High magnification SEM images corresponding to (a) fibroblast and (b) osteoblast cells seeded on HD-Al/Al$_2$O$_3$ NWs.
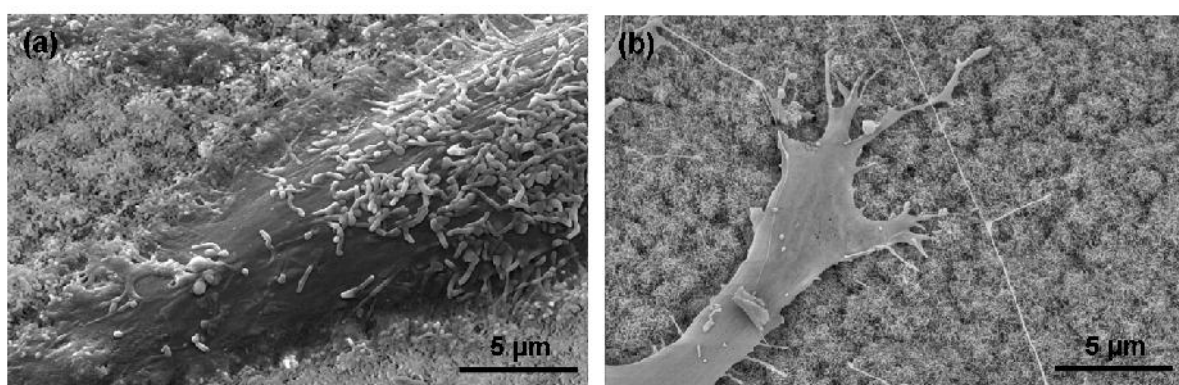
Figure 5.19: High magnification SEM images corresponding to (a) fibroblast and (b) osteoblast cells seeded on UHD-Al/Al$_2$O$_3$ NWs.

In figure 5.20 is observed how the filopodia of osteoblast cells anchor to LD-NWs (a) and MD-NWs (b) and figure 20 shows how they adhere on UHD-NWs substrates. It has been demonstrated by several authors that filopodia are the cell's tools for exploring its surroundings[195]. Filopodia contain receptors for diverse signalling molecules and extracellular matrix molecules. This is why one of the roles of filopodia is to sense the cell surroundings. Also they act as sites for signal transduction. It is known that integrins and cadherins, which are cell adhesion molecules, are often found in the tips of filopodia or along the shafts[196-197]. Integrins in filopodia probe the matrix, creating "sticky fingers" along the leading edge that promote cell adhesion and migration[198-199]. Tacking into account that the size of the integrins is in the nanoscale, we believe that the shape, size and distribution of the Al/Al$_2$O$_3$ plays a big role on osteoblast adhesion. It is clearly observed that in case of LD-NWs and MD-NWs the filopodia adhere and try to penetrate the nanostructure. In case of UHD-NWs (figure 5.21) the cauliflower structure that the Al/Al$_2$O$_3$ NWs adopt after long deposition is observed. Here we can observe how the filopodia extremes try to anchor to the nanowire tips rather than to the clustered NWs (yellow circles and red arrows). Such images lead us to think that the **osteoblast filopodia prefer to anchor to the nanostructures rather than to the microstructures.**

105
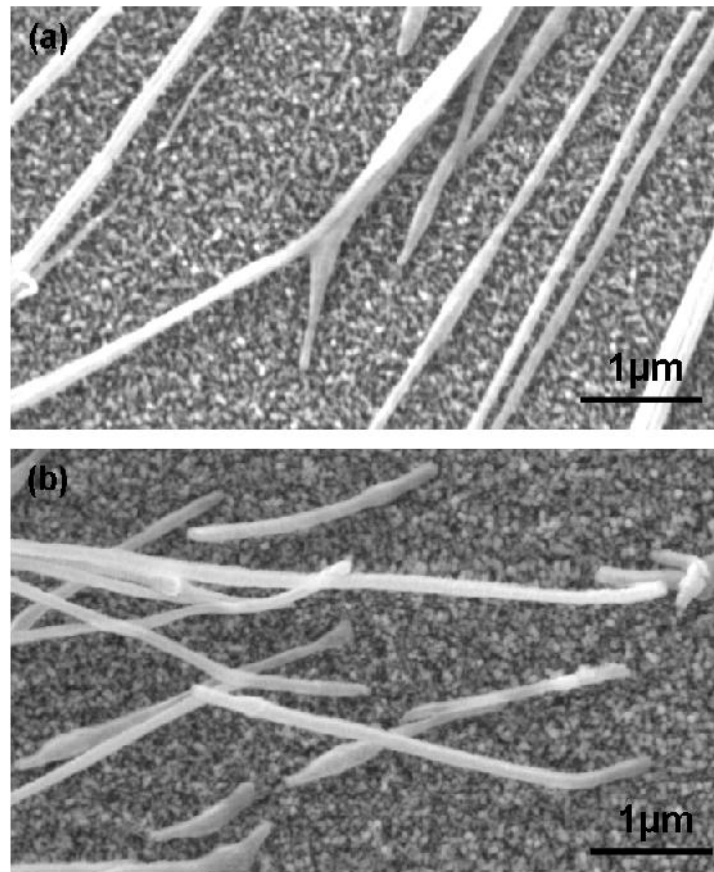
Figure 5.20: SEM images of osteoblast filopodia adhering on deposited Al/Al$_2$O$_3$ NWs. (a) LD-NWs, (b) MD-NWs.
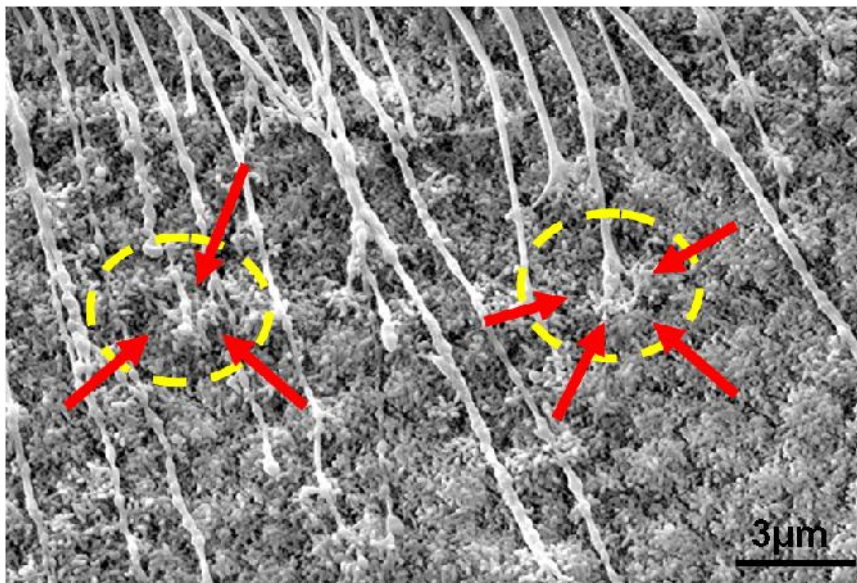
Figure 5.21: SEM images of osteoblast filopodia adhering on deposited UHD-NWs.

5.2.2.3 Cell growth: cell density and mean cell area

The determination of the cell growth was performed by quantification of two parameters, cell density and mean cell area 48 h post seeding, which represents late adhesion. After 6 h early adhesion takes place and after 48 h information about both, adhesion and proliferation, can be obtained. Cell density and mean cell area were quantified and compared for fibroblast and osteoblast cells after seeding them on the 1D Al/Al$_2$O$_3$ NWs. Due to the different seeding densities used for every cell type the results have been normalized to the control.

Figure 5.22 shows that the cell density of osteoblast cells on 1D Al/Al$_2$O$_3$ NWs tends to be higher compared to the corresponding control as the coating density increases, while in the contrary, fibroblast cell density tends to decrease. This quantitative analysis confirms the tendency shown by fluorescence images after staining in a previous section of this chapter; **while the amount of <u>osteoblast</u> cells observed increased as the Al/Al$_2$O$_3$ NWs density type increased, the amount of <u>fibroblast</u> decreased** (figure 5.22).

Statistical analysis were performed using a paired t-test analysis and the results showed that in case of LD-NWs the difference in the mean cell density values between fibroblast and osteoblast is not great enough to reject the possibility that the difference is due to random sampling variability. There is not a statistically significant difference ($p = 0.089$). On the other hand, in case of MD-NWs, HD-NWs and UHD-NWs the difference in the mean values between fibroblasts and osteoblasts is greater than would be expected by chance, therefore there is a statistically significant difference ($p = 0.033$ for MD-NWs, $p = 0.008$ for HD-NWs and $p \leq 0.001$ for UHD-NW).
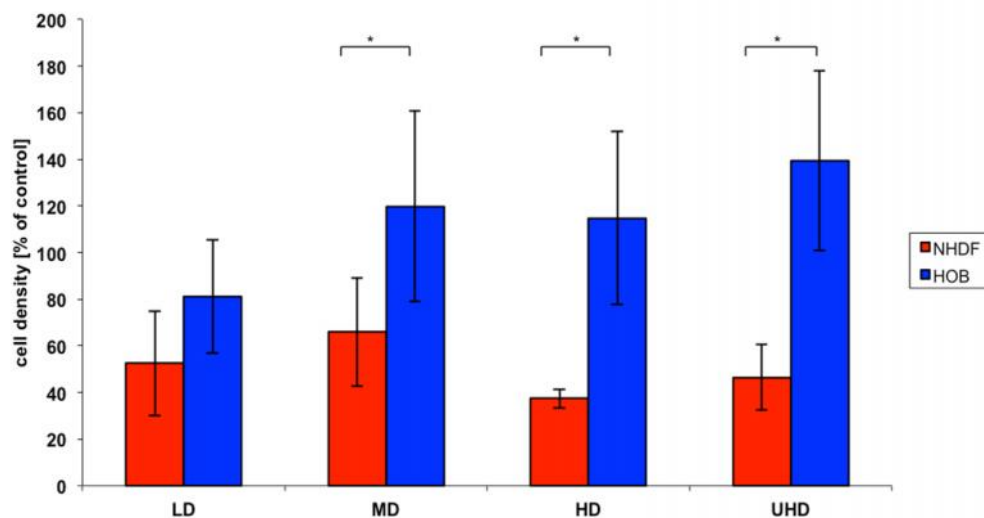
Figure 5.22: Cell density (% of control) comparisons between osteoblast (HOB) and fibroblast (NHDF) cells cultured on deposited Al/Al$_2$O$_3$ NWs.

Concerning the cell area analysis, figure 5.23 depicts the mean cell area quantified for fibroblast and osteoblast cells cultivated on the different Al/Al$_2$O$_3$ nanostructures. **It is observed that the mean cell area in case of <u>osteoblast</u> cells remains constant regardless of the density of deposited 1D Al/Al$_2$O$_3$ NWs while the mean cell area of <u>fibroblasts</u> varies**. The quantitative analysis results confirm what was observed in the SEM images in a previous section of this chapter which showed that fibroblast cells changed their shape and morphology as the Al/Al$_2$O$_3$ nanowire density increased due to difficulties to adhere to the substrate and as a consequence, their area varies.

Similar to the cell density, statistical analyses were performed applying a paired t-test analysis and the results showed that in case of LD-NWs the difference in the mean cell area values between fibroblasts and osteoblasts is not great enough to reject the possibility that the difference is due to random sampling variability. There is not a statistically significant difference (p = 0.222). On the other hand, in case of MD-NWs, HD-NWs and UHD-NWs the difference in the mean values between fibroblasts and osteoblasts is greater than would be expected by chance, therefore there is a statistically significant difference (p ≤ 0.001 for MD-NWs, p ≤ 0.001 for HD-NWs and p = 0.002 for UHD-NW).

Figure 5.23: Mean cell area (% of control) comparison between osteoblast (HOB) and fibroblast (NHDF) cells cultured on deposited Al/Al$_2$O$_3$ NWs.

5.2.2.4 Overall metabolic activity, WST-1 test

In order to evaluate the overall metabolic activity of fibroblast and osteoblast cells on the different Al/Al$_2$O$_3$ nanostructures the WST-1 test was performed. The graph from figure 5.24 shows that no differences in the WST-1 could be found between fibroblast and osteoblast cells cultivated on 1D Al/Al$_2$O$_3$ NWs. Different set-up experiments were used for every cell type and this is why the results

were normalized to the control. Similarly than for cell density and mean cell area, statistical analysis were performed using the paired t-test analysis and the results showed that in all cases the difference in the mean WST values between fibroblasts and osteoblasts is not great enough to reject the possibility that the difference is due to random sampling variability. There are no statistically significant differences ($p = 0.589$ for LD-NWs, $p = 0.921$ for MD-NWs, $p = 0.369$ for HD-NWs and $p = 0.054$ for UHD-NW).
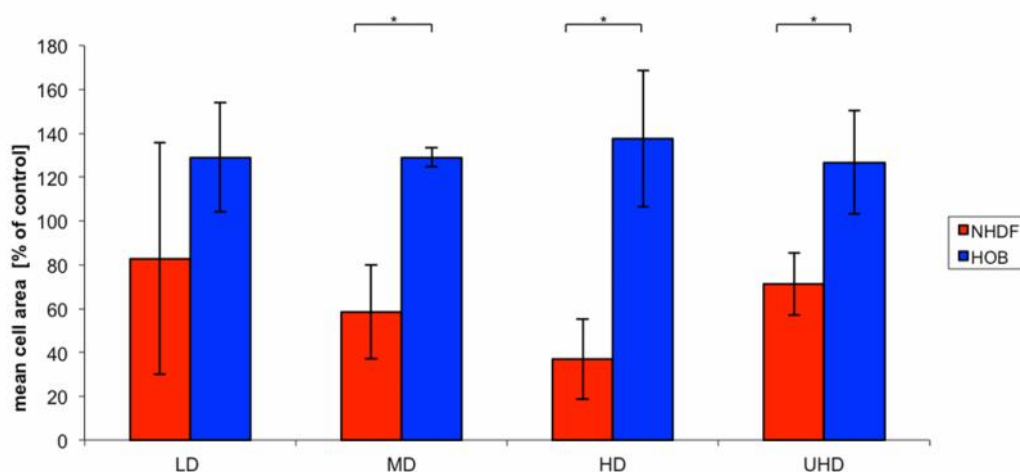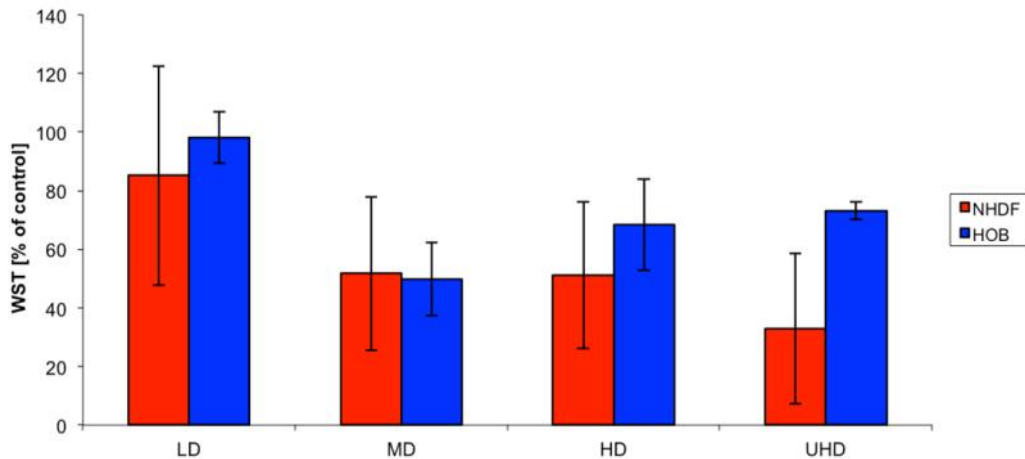

Figure 5.24: WST-1 comparison between osteoblast (HOB) and fibroblast (NHDF) cells cultured on deposited Al/Al$_2$O$_3$ NWs.

All the presented results lead to the conclusion that **there is a <u>selective adhesion between the two competitive cell lines</u> as the density of the deposited Al/Al$_2$O$_3$ NWs increases**. It is of high importance to identify which are the material properties, which influence bone and competitive cell adhesion. In chapter 4 several parameters, which could affect cell adhesion, were defined.

5.3 Osteogenic differentiation on Al/Al$_2$O$_3$ NWs

In bone formation, osseointegration at the bone-implant interface requires activation of key regulatory pathways, which influence osteoblastogenesis, promotion of osteoblastic differentiation and maturation, and finally bone repair/regeneration. Investigating the effect of surface topography on changes in gene expression may therefore, provide information into the regulatory mechanisms behind bone formation at the bone-implant interface[200]. In this work, the osteoblast differentiation is investigated on the four different Al/Al$_2$O$_3$ nanostructures defined in previous chapters. Several studies investigated alterations in cellular behaviour patterns such as; adhesion, morphology, DNA synthesis, integrin and extracellular matrix gene expression, and enzyme activity have been carried

out *in vitro* to elucidate the finer elements of the osteoblast response to materials used in fracture fixation[145,142, 201-203].

In the frame of this work the effect of different Al/Al$_2$O$_3$ coatings on the osteogenic gene expression by means of qRT-PCR is investigated for first time. The gene expression experiments have been performed by the Collaborative Research Centre of Homburg from AO foundation and the AO Reasearch Institute Davos in Switzerland. The results included in this section have been submitted by Metzger et al. to the journal "Biomaterials".

5.3.1 Basics of osteogenic differentitaion:

Jäger et al.[204] explained that osteoblasts and osteoclasts are mainly responsible for the osteointegration of nanostructured biomaterials in orthopaedics. Osteoblasts derive from mesenchymal progenitor cells, which are localized mainly in the bone marrow and periosteum. They are characterized by cuboidal and flat morphology (diameter about 20 µm), present a large amount of rough endoplasmatic reticlum and a large Golgi apparatus, and are potent to produce osteoid, a collagen I rich matrix[205]. In addition, these mononuclear cells are also responsible for osteoid calcification (hydroxyapatite). Typical marker proteins for osteoblasts are core binding factor 1 (Cbfa1), runt-related transcription factor 2 (Runx2), osteocalcin, osteopontin, osteonectin, bone sialoprotein (BSP), osteoprotegrin (OPG), collagen I, and alkaline phosphates (ALP). Figure 5.25 gives a brief summary of the expression of several markers during osteoblast differentiation. The differentiation of osteoblast is characterized by different stages and lasts *in vivo* about 3 days. 50 to 70 % of all osteoblasts undergo programmed cell death (apoptosis) whereas the rest differentiate into osteocytes or persists as resting or bone-lining cells[206]. In case of on vitro the osteoblasts differentiate over 21 days. After 5 days the effects can be checked.
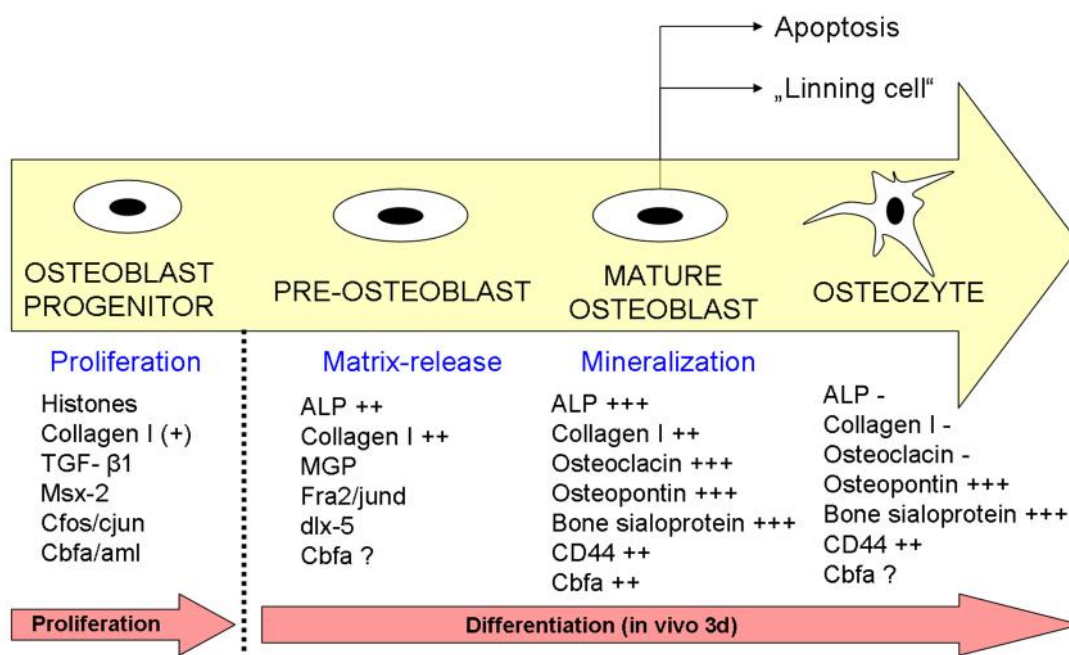
Figure 5.25: Osteoblast differentiation *in vivo* (adapted from[204]).

When trapped into the mineralized bone, osteoblasts differentiate into osteocytes. Osteocytes act in a paracrine and mechanosensory manner, and can activate osteoblasts and osteoclasts. The latter cell type derived from the hematopoieticline, has multiple nuclei and is responsible for bone resorption. Its ruffled border is flanked by a sealing zone which facilitates local acidification and removal of bony matrixsuch as Ca^{2+}, H$_3$PO$_4$, and H$_2$CO$_3$ by endocytosis. Osteoclasts express high levels of tartrate-resistant acid phosphatase (TRAP) and cathepsin K. The interaction between nosteoblasts and osteoclasts is complex. During differentiation, the ostoblast progenitors express receptor activator of nuclear factor κβ ligand (RANKL) and macrophage colony stimulating factor (M-CSF) which are strong stimuli for osteoclastogenesis. In contrast, osteoprotegerin (OPG) is a potent inhibitor of osteoclasts. Moreover, the interactions between osteoblasts and osteoclasts *in vivo* are regulated by several hormones and cytokines, including parathyroid hormone (PTH), calcitonin, and IL-6.

5.3.3 Experimental approach

5.3.3.1 Synthesis of Al/Al$_2$O$_3$ NWs

Similarly than in the previous section of this chapter, glass coverslips (⌀ = 32 mm, Thermo Scientific, Germany) were used as substrate for this experiment. The required diameter of the substrates is bigger for this experiment. The deposited Al/Al$_2$O$_3$ NWs were deposited on the glass coverslips as described in chapter 3. For this experiment a specific graphite susceptor was designed. 3 holes (⌀$_{hole}$

= 32 mm) were perforated on the graphite. This geometry allowed us to coat 3 samples at the same time under identical conditions. For every density type 25 samples were fabricated. A total number of 100 coated samples were used for this experiment. The experiment number was n = 6.

5.3.3.2 Gene expression analysis

Cell Culture

Similarly than in the previous experiment, Human osteoblasts (HOB) from PromoCell (Heidelberg, Germany) were cultivated in Dulbecco's Modified Eagle Medium (DMEM, PAA-laboratories, Pasching, Austria) supplemented with 15 % fetal calf serum (FCS, PAA-laboratories) in 75 cm^2 tissue flasks until they reached near-confluence. HOB from three different donors were used (donor n°1 51 years-old male, donor n°2 58-years old female, donor n°3 51-years-old male, all bone material derived from knee) with the aim to exclude donor-specific effects. Incubation took place at standard conditions (37°C, 95 % humidity and 5 % CO$_2$) and standard trypsination procedures were used for cell detachment. Multiwell plates (24 well plates or 6 well plates, respectively) were used for all cell culture experiments. Glass cover slips coated with 1D Al$_2$O$_3$ nanostructures and uncoated cover slips serving as control were sterilized by incubation in ethanol (70 %) for at least 20 min. After sterilization the samples were heated up to 240°C for at least 4 h to destroy RNases for the qRT-PCR-experiments. Cells designated to be used in qRT-PCR-experiments were seeded at 400 cells/mm^2. The cell culture and the subsequent procedures were done two times with cells from three different donors (n = 6). Cell confluence was reached after 72 h and the medium was supplemented for osteogenic differentiation according to Hayes et al.[207] with ascorbic acid (50 µg/ml; Fluka, Buchs, Suisse), dexamethasone (10 nM; Sigma, St. Louis, MO, USA), β-glycerophosphate (5 mM; Calbiochem, Darmstadt, Germany) and penicillin-streptomycin (1 %; PAA-laboratories). Total RNA was isolated on day 0, day 7, day 14 and day 21 after incubation in differentiation medium.

RNA isolation

After cell culture, the medium was removed and the samples (n = 6) were rinsed three times with PBS (37°C). Afterwards, 300 µl of TRI-reagent (Sigma) and 2.5 µl of Polyacryl-Carrier™(Molecular Research Center, Cincinnati, OH, USA) were added. The cells were lysed by the action of TRI-reagent. 150 µl of 1-bromo-3-chloro-propane (Sigma) was added to the samples and they were incubated for 10 min at RT. After centrifugation at 12.000 x g at 4°C for 15 min three phases and the aqueous solution were formed. The contained RNA was transferred to a new RNA-free tube. Prior to incubation, 125 µl isopropanol (100 %, Sigma) and 125 µl of high salt precipitation solution (0.8 M sodium citrate and 1.2 M sodium chloride, Sigma) were added and mixed by inversion. Incubation took place during 10 min at RT and afterwards an additional centrifuging was performed as described

above. After removing the supernatant the resulting pellet was dissolved in 300 µl of ethanol (75 %, Sigma). According to the manufacturer's instructions the purification of the RNA was performed using QiagenRNeasy columns (Qiagen, Hilden, Germany). In order to analyse the purity and quantity of the RNA a Nanodrop system was used by determination of the Absorption 260/280 nm-ratio. A minimum absorption at 260 nm of 0.15 absorption units and a ratio of Absorption 260/280 nm-ratio between 1.8 and 2.2 was set as our internal quality threshold. The storage of the RNA-samples was performed at –80°C until the reverse transcription.

Reverse Transcription

The High-Capacity cDNA Reverse Transcription Kit (Applied Biosystems, Carlsbad, CA, USA) was used to perform the reverse transcription (RT). A 2x Master Mix was prepared containing 2.0 µl 10x RT-buffer, 0.8 µl 25x dNTP mix (100 mM), 2.0 µl 10x RT-random primers, 1.0 µl Multi Scripe™ Reverse Transcriptase (final concentration 50 U/µl), 1 µl RNase inhibitor and 3.2 µl RNase-free-water. 10 µl of the Master Mix were mixed with 10 µl of the RNA-sample for every transcription. A Gene Amp 2400 (Perkin Elmer, San Jose, CA, USA) was used in order to perform the reverse transcription; the primer incubation was done at 25°C for 10 min, the reverse transcription at 37°C for 120°C and the incubation of the reverse transcriptase at 85°C for 5 min. Until the quantitative real-time polymerase chain reaction (qPCR) was performed the obtained cDNA was stored at -20°C

Quantitative real-time polymerase chain reaction

A SDS 7500 Real Time PCR instrument (Applied Biosystems) was used to carry out the Real time polymerase chain reaction (qRT-PCR) esperiment using 2x Gene Expression Master Mix (Applied Biosystems). Table 5.2 describes the primer-probe systems used under standard thermal conditions. Verification of the efficiencies of the custom-designed primer-probe systems has been done using the ΔCt method described in the ABI PRISM 7700 Sequence Detection System User Bulletin #2 (Applied Biosystems) PCR mixtures contained 900 nM of each forward and reverse primers, 250 nM Taq Man™ probe (or 1 µL 20x primer-probe concentrate for gene expression assays), and 2 µL cDNA in a total reaction volume of 20 µL. In order to activate the polymerase the temperature conditions were 95°C for 10 min followed by denaturation (45 cycles at 95°C for 15 sec) and annealing/Extension (at 60°C for 60 sec). The relative quantification (ΔΔCt) method was used for gene expression data normalization to 18S ribosomal RNA and relative expression to the mRNA expression level of cells cultured on glass as the internal control for each donor.

The genes of interest related to osteogenic differentiation were bone sialoprotein (BSP2) 2, Collagen 1 (COL1), osteocalcin (OC), osteopontin (OPN), Runt-related transcription factor 2 (RUNX2), Sp7

transcription factor (osterix, SP7) and alkaline phosphatase liver/bone/kidney (ALP). Each sample was run in duplicates.

Table 5.2: qPCR primers and TaqMan© probes for the analyses of the gene expression profile F = Forward, R = Reverse.

Gene Accession Nr.	Primer nucleotide sequence (5' to 3') or Gene Expression Assay number
BSP2 NM_004967	F TGC CTT GAG CCT GCT TCC R GCA AAA TTA AAG CAG TCT TCA TTT TG Probe CTC CAG GAC TGC CAG AGG AAG CAA TCA
COL1 NM_000088	F CCC TGG AAA GAA TGG AGA TGA T R ACT GAA ACC TCT GTG TCC CTT CA Probe CGG GCA ATC CTC GAG CAC CCT
OC NM_199173	F AAG AGA CCC AGG CGC TAC CT R AAC TCG TCA CAG TCC GGA TTG Probe ATG GCT GGG AGC CCC AGT CCC
OPN NM_000582	F CTC AGG CCA GTT GCA GCC R CAA AAG CAA ATC ACT GCA ATT CTC Probe AAA CGC CGA CCA AGG AAA ACT CAC TAC C
RUNX2 NM_001024630	F AAG CAG TAT TTA CAA CAG AGG GTA CAA G R GGT GCT CGG ATC CCA AAA Probe CAT CAA ACA GCC TCT TCA GCA CAG TGA CAC
SP7 NM_152860	F CCT GCT TGA GGA GGA AGT TCA R GGC TAG AGC CAC CAA ATT TGC Probe TCC CCT GGC CAT GCT GAC GG
ALP	Gene expression assay Nr. Hs00758162_m1
18S rRNA	Gene expression assay Nr. 4310893E

5.3.4 Results and discussion

Gene expression profile

Alkaline phosphatase (ALP) mRNA expression was significantly up-regulated in cells cultured on all the investigated surfaces as compared to the glass control surface at day 7 of culture. ALP expression still tended to be enhanced at day 14, while there was no more difference to the glass cultures by day 21 of culture (figure 5.26a). ALP is an enzyme that is associated with calcification, although its

exact role is not known. Almost all cells have alkaline phosphatase in their plasma membranes, although cells that calcify their extracellular matrix, including odontoblasts (tooth forming cells), cementoblasts (cementum forming cells), and growth plate chondrocytes (cartilage cells at the ends of long bones), tend to have higher levels of this enzyme. Moreover, activity of the enzyme increases when osteoblasts produce osteoids, owing in large part to the production of extra cellular membrane organelles celled matrix vesicles. This is an early marker of osteoblast differentiation because activity is greatest just before mineralization actually begins. The effect of alkaline phosphatase is to increase local levels of inorganic phosphate, one of the components of apatite, the mineral phase of bone.

The gene expression of BSP showed a clear trend to be increased in cells cultured on all the surfaces compared to glass at day 14; this was most significant for the UHD-NWs (p = 0.055) (figure 5.26b).

Osteopontin mRNA expression was increased already at day 0 in the UHD-NWs and MD-NWs cultured cells; by day 21 the expression of osteopontin was markedly up-regulated in cells cultured on UHD-NWs, HD-NWs and MD-NWs surfaces as compared to glass (figure 5.26c). Culture on UHD-NWs also resulted in elevated mRNA expression levels of collagen type I and Runx2 by day 14, although the gene expression differences in comparison to glass were small (figure 5.26d). No differences in osteocalcin and SP7 gene expression levels were observed, except for a slight increase in SP7 mRNA in the LD-NWs group at day 7.
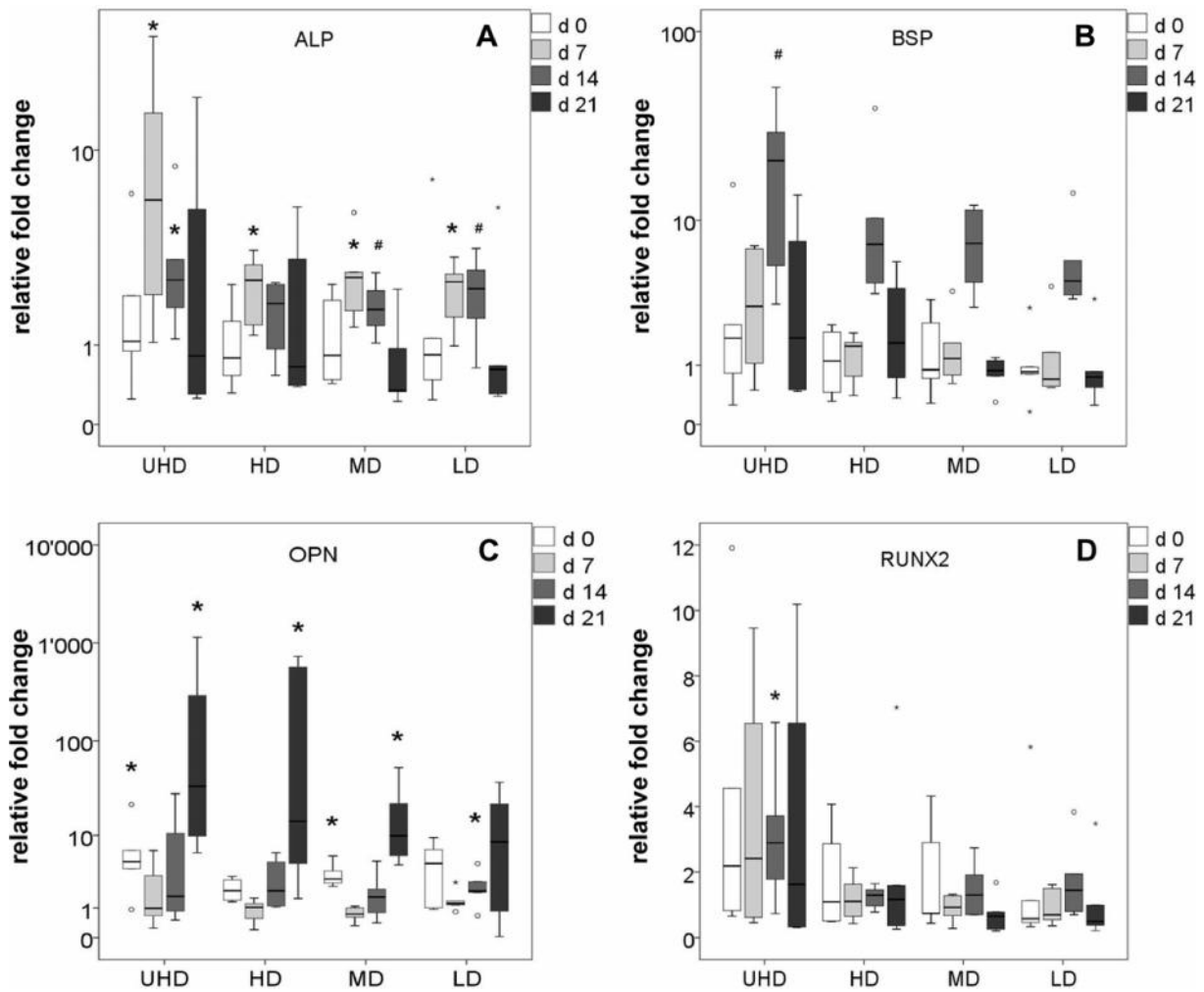
Figure 5.26: Gene expression profiles of HOB cultivated on cover slips coated with 1D Al$_2$O$_3$ nanostructures of different densities for ALP (a), BSP2 (b), OPN (c), RUNX2 (d). Data are expressed as the meanfold increase in mRNA-expression relative to glass at the same time point.

These results clearly show that the **gene expression of osteoblast is affected by the topography of the substrate. Some of osteogenic marker genes under investigation where significantly up-regulated after cultivation on the different NWs, indicating that the NWs were able to induce osteogenic differentiation processes.** This is in line with the literature reports describing an increased osteogenic differentiation on rougher surfaces compared to smoother ones[4,142]. Unfortunately, most of the reports on this topic deal with microtopographies and not with topographies in the nanometer range. Therefore, a direct comparison with data from literature is difficult. Since we are working with nanotopographies it is difficult to discriminate between direct influences of the topography or indirect influence of the adsorbed protein layers on osteogenic differentiation.

5.4 Quantisation of cell adhesion on Al/Al$_2$O$_3$ NWs using cell monolayer rheology (CMR)

The specific biochemical adhesion of molecules to the extracellular matrix plays a leading role in many cellular processes, among them cell differentiation, morphogenesis, and wound healing. Various medical applications require endogen cells to bind to an exogenous substrate as in the case of an implant. Coatings with proteins that naturally belong to the extracellular matrix are known to enhance the cell adhesion. However, the choice of inorganic materials, which promote cell adhesion, is limited. In order to reliably determine cell-mechanical properties, the ''Cell Monolayer Rheology (CMR)'' technique was used. Fernandez and colleagues[208] developed the CMR technique in order to determine cell-mechanical properties. They performed a broad and systematic investigation of the rheological properties of fibroblast cells using CMR technique. This new technique provides a one-shot averaging of rheological data over ~10^6 cells, making the experiments highly reproducible and reliable. They showed that mechanical behaviour of fibroblast cells could be characterised by a set of very robust, general mechanical responses. The study of rheological properties with the help of rheometers is a well-described method that has been used by material scientists for decades.

In this context, the CMR technique has been used in order to investigate the mechanical behaviour of fibroblast cells on the as deposited Al/Al$_2$O$_3$ NW coatings. The cell culture and rheology experiments have been performed in the Biological Experimental Physics department of the Saarland University by the PhD student Mathias Sander under the supervision of Prof. Ott. We already reported the experimental approach and results presented in this section in the "Applied Surface Science" journal[209].

5.4.1 Experimental approach

5.4.1.1 Synthesis of Al/Al$_2$O$_3$ NWs

LD-Al/Al$_2$O$_3$ NWs were deposited on glass plates by CVD of the molecular precursor [^{t}BuOAlH$_2$]$_2$. For this experiment two specific graphite susceptors were designed in order to adapt the graphite geometry as much as possible to the substrate avoiding air gaps between the susceptor and the substrate. A single hole was perforated in the middle of the graphite susceptors with diameters of 35 mm and 45 mm respectively. The deposition was conducted as explained previously in chapter 3. Deposition time was kept around 10 minutes and the flow rate was controlled manually using a sensitive pressure sensor coupled to the vacuum chamber. In figure 5.27 is observed that the coated glass plate has a greyish colour and is less transparent than the glass.

Figure 5.27: Optical image of non-coated (left) and coated (right) glass plates.

5.4.1.2 CMR set up

A commercial rhemoeter (Haake Mars rotational rheometer, Thermo Fisher Scientific) has been used as a measurement tool for the rheological experiments. The rheometer is capable of performing controlled stress and controlled deformation experiments. As measurement geometry we used a plate-ring setting. The setting consists of a lower plate (diameter of 40 mm) fixed onto the base of the rheometer and a ring (outer diameter of 20 mm, inner diameter of 15 mm) connected via a rotational sensor to the measurement head of the rheometer[210].
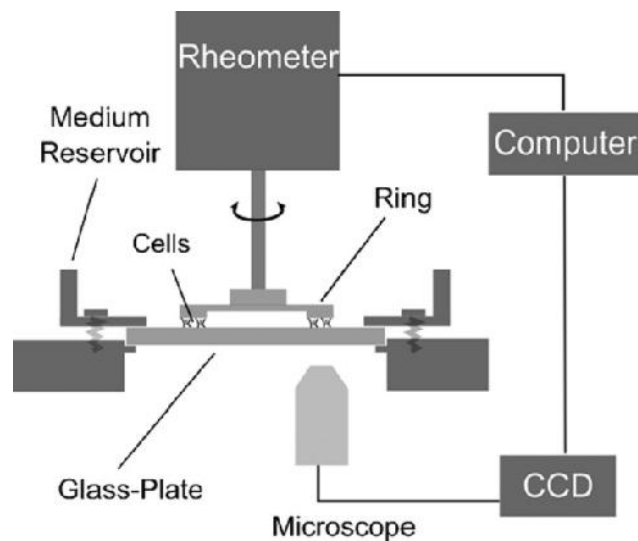
Figure 5.28: Schematic representation of the CMR setup.

5.4.1.3 Cell culturing

NIH Swiss 3T3 cells derived from the DSMZ (Deutsche Sammlung für Mikroorganismen und Zellkulturen GmbH) were used for this experiment. Cell culturing was done using standard protocols[211]. The medium components are 500 ml Dulbecco's Modified Eagles Medium (DMEM with 4.5 g/l glucose and L-glutamine), 10 % of foetal bovine serum (FBS Gold, PAA Laboratories), and 100 mul of antibiotics penicillin/streptomycin. In order to detach the cells from the cell culture flasks

incubation with a Trypsin-EDTA solution (1x, Sigma Aldrich) was performed for 5 minutes inside an incubator at 37 °C. The Trypsin inhibition was performed with 40 ml of cell medium followed by a 5 min centrifugation step at 200 G. Afterwards, the cells were re-suspended. A micro-bead solution (1.5 µl, diameter 6.84 µm) was added to the final cell suspension for the exact alignment of the glass plates parallel to each other within the rheometer.

5.4.1.4 Rheological measurement of the cell adhesion

As reported in our publication[209] the homogenized cell solution was introduced into a medium reservoir. The glass ring was loosely screwed onto a rotational sensor and aligned parallel to the second glass plate. During 45 minutes the process is stoped in order to let the cells adhere to both plates. The adjustment of the upper plate was fixed to the rotational sensor and another 60 minutes adherence step took place. In order to measure unstressed cells, the gap between the plates was adjusted to the mean diameter of fibroblast cells (approx. 15 µm). The complete procedure is shown in Figure 5.29.
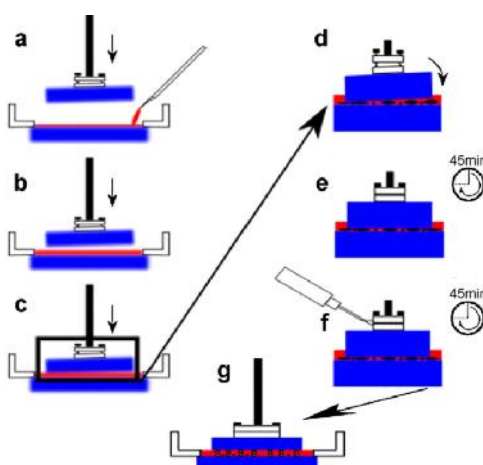
Figure 5.29: Schematic presentation of the micro-bead procedure for parallel plate adjustment.

5.4.2 Results and discussion

5.4.2.1 Cell culturing on Al/Al$_2$O$_3$ NWs

The cells were cultures on glass plates coated with fibronectin and NWs for comparision. Optical images were taken after 1, 3 and 21 hours after incubation. Comparing the change in the cell morphology and proliferation in the course of time we observed a change in the cell morphology, which indicates a good cell adhesion and proliferation, which shows a healthy cell growth. After 1 hour the 3T3-cells were beginning to spread on both culturing substrates, which mark the beginning of the adherence process (Figure 5.30). During the following 2 hours an increasment on the spreading was observed. After 3 hours the cells started proliferating indicating a healthy cell growth.
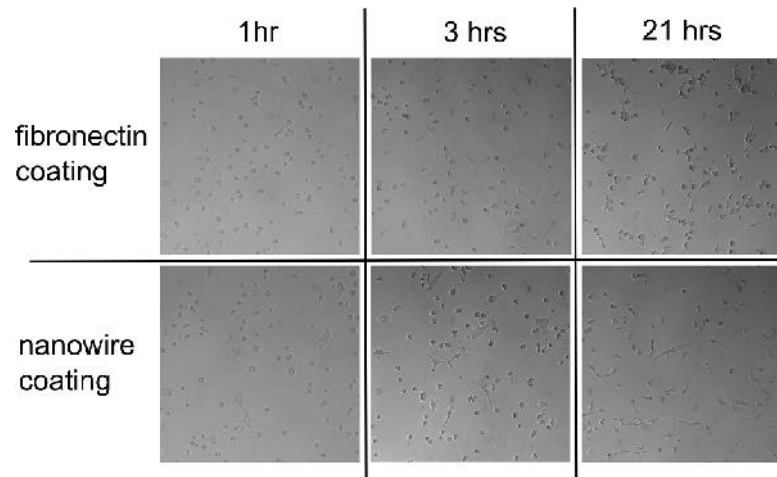
Figure 5.30: Optical images of fibroblasts on fibronectin (upper) and NWs coated glass plates (lower) after 1, 3, and 21 hours (from left to right).

5.4.2.2 Cell mechanical properties and cell adhesion force measurement

CMR analysis was carried out in detail with the aim to compare themechanical behaviour of cells on NWs coated and non-coated glass plates. For this measurement a cell monolayer harmonically (sinusoidal) was deformed at a defined amplitude and frequency. The resistive torque was measured in phase and at a 90° shift. Elastic and viscous moduli, G' and G'', were deduced. In Figure 5.31a and 5.31b it can be seen that fibronectin and NWs coatings exhibit similar rheological behaviour in terms of amplitude and frequency sweeps. This indicates a similar structure of the cell cytoskeleton, which is strongly governed by cell adhesion properties. For the measurement of cell adhesion strength, we performed adhesion rupturing tests. We kept increasing the deformation amplitude until a rupture of cell adhesion bonds could be detected by optical microscopy simultaneously to a drop in the restoring force.
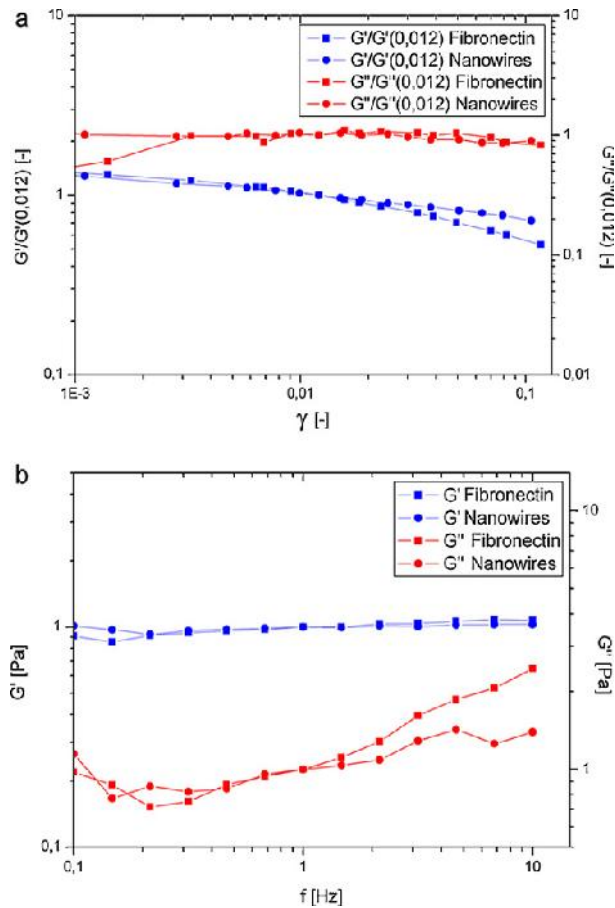
Figure 5.31: (a) Normalized viscoelastic moduli derived by an amplitude sweep at f = 1 Hz for fibronectin and NWs coated glass plates. (b) Frequency-dependence of the normalized moduli determined by a frequency sweep with oscillation amplitude of 1 %.

Results from rupturing tests are shown in figure 5.32. The viscoelastic moduli as well as the stress-deformation-relationships exhibit a leap at a deformation of comparable size for both NWs and fibronectin coatings. At the leap, which is due to a rupture of adhesion bonds, the deformation becomes much more distinctive in response to a small increase in stress.
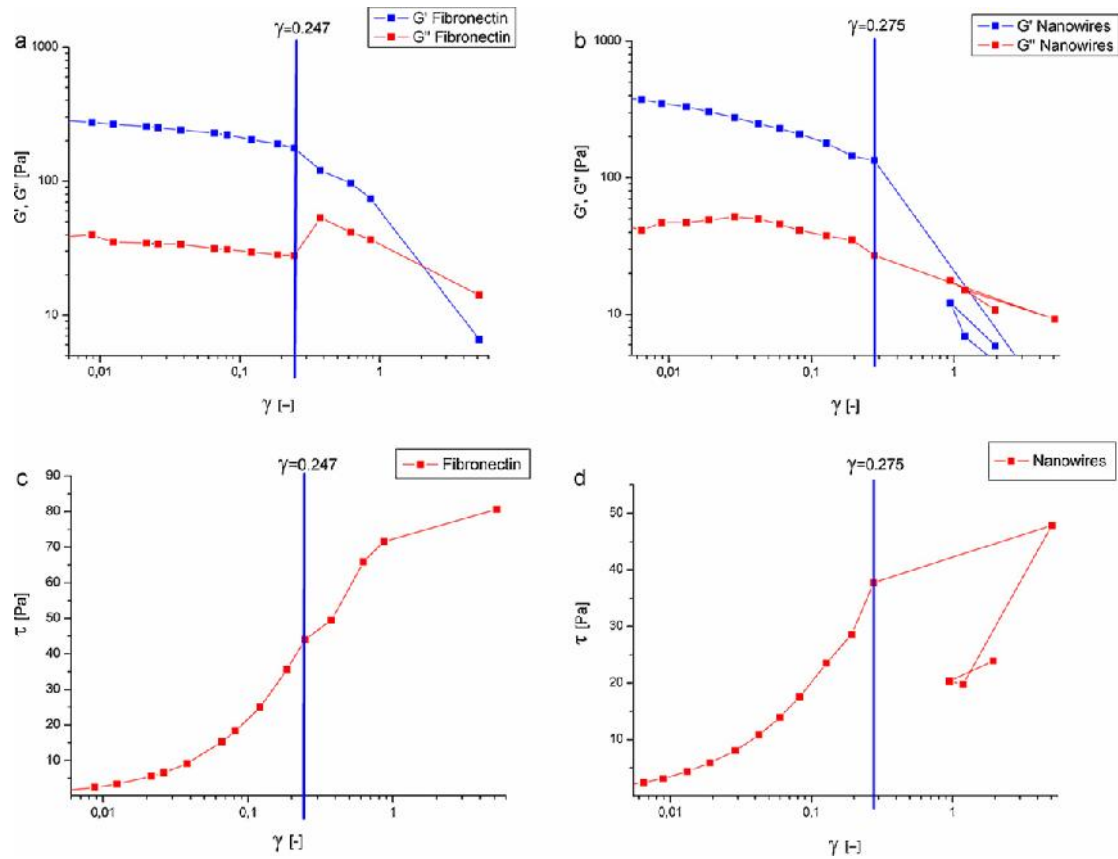
Figure 5.32: Viscoelastic moduli determined by an amplitude sweep at f = 1 Hz, (a) fibronectin and (b) NWs coated glass plates. Stress-Strain-Relationship for a cell-rupturing-experiment (c) fibronectin and (d) NWs coated glass plates.

The rupturing tests revealed an adhesion bond failure at a deformation of about 25 % for fibronectin and 27.5 % for NWs coating. We observed comparable adhesion strengths for both substrates, differences in absolute values corresponded mostly to differences in cell density. However, whereas in case of NWs coating, the cells collectively ruptured in one event, cell rebinding occurred for the fibronectin coating. The latter was identified from multiple leaps in the stress-deformation graph resulting in a higher relative increase in resistive force, compared to the first rupturing event. In contrast to culture conditions, we observed that here the cells seemed to need more time to establish a mechanically robust adhesion to the NWs. This difference may be due to the fact that fibronectin is part of the natural ECM. Pulling on integrin mediated bonds (such as fibronectin) is known to stimulate mechanical cell response, which increases adhesion bond size and mechanical cell resistance. For the NWs-coating, the binding mechanisms may be more non-specific. It will be interesting to gain a broader view on cell adhesion dynamics on NW coatings in the future.

6

Conclusion and outlook

In this thesis the CVD technique has been used in order to obtain 1D Al/Al$_2$O$_3$ NWs. A home-built CVD device has been designed and constructed in order to coat a big number of samples at the same time under same conditions fulfilling in this way the requirements of "reproducibility" and "repeatability". The deposition of the single source precursor [^{t}BuOAlH$_2$]$_2$ was performed under a fixed temperature and pressure. For the first time different nanostructures were obtain changing exclusively the deposition time. Four different deposition times were used obtaining as a result **four different coating densities: LD-NWs, MD-NWs, HD-NWs and UHD-NWs.** As the deposition time increases so does the he Al/Al$_2$O$_3$ nanowire density.

For first time, a **3D model** of the Al/Al$_2$O$_3$ coatings has been reconstructed using FIB/SEM techniques and specific software in order to quantify and analyse some structural properties of the coating and provide a better understanding and visualization. As a result, from the 3D model is concluded that:

- The **LD-NWs can be considered as nanorods** due to their low aspect ratio (< 20) while the aspect ratio for MD-NWs, HD-NWs and UHD-NWs fit the "nanowire" definition. **UHD-NWs present a cauliflower structure** at top of the coating. Some clusters are formed with nanowires over them. In this context, the UHD-NWs is considered a structure containing micro and nanofeatures while LD-NWs, MD-NWs and HD-NWs present nanofeatures exclusively.

- The thickness of the coatings increases as the deposition increases following a linear tendency. Characteristically, the UHD-NWs structure does not fit the linear tendency. This fact is due to the presence of micro and nanofeatures in this singular structure.

- 2D and 3D porosity were analysed for all densities. The **2D porosity** is, for all densities, constant along x and y-directions of the coating but it **decrease along the width of the coatings (z-direction)**. Values around 70 % are found at the bottom of the coatings reaching almost 100 % at the top of the coatings. The evolution of the 2D porosity through the z-direction reveals that **the interaction between nanowires (branching and contacts) increases as the Al/Al$_2$O$_3$ nanowire density increases**. Concerning x any y-directions, values between 80 % and 90 % porosity have been found. The **global porosity ( ) is ~80 % for all densities.** High porosities confined in a nanostructured network open up some applications related with the gas and liquid flow and retention through and in the coating. As an

example, our coatings could be promising for **hydrogen storage** purposes or used as **membranes for gas treatment**, or for **nanofiltration in the field of water treatment**.

- The **specific surface area (S$_v$) increases as the Al/Al$_2$O$_3$ nanowire coating is denser**. Similarly, the specific **surface area to volume ratio (SA/V) also increases**. Strucutres containing big surface areas are of high interest due to their **big capacity to react with external agents**.

- The **geometrical tortuosity ( )** is rectilinear in x and y directions for all density types and more complex along the z-direction. **The complexity in z-direction increases as the Al/Al$_2$O$_3$ nanowire coating is denser.** Having an idea of which is the tendency of the geometric tortuosity provides a better understanding of the **transport properties** of our porous media.

- The Euler number ( ) indicates that **the connectivity between the nanowires is higher as the Al/Al$_2$O$_3$ coating is denser**. The loss of connectivity in bones is one of the reasons of "osteoporosis" illness. In order to mimic as much as possible the structure of a healthy bone it is important to take into account that a high connectivity between features is optimal.

Additionaly, the surface of the Al/Al$_2$O$_3$ coatings has been studied using characterization well known techniques and as a conclusion:

- The XPS spectra verified the assumed hypothesis that the **surface chemistry is identical for the different Al/Al$_2$O$_3$ densities**.

- The roughness has been analysed using AFM and profilometer techniques. It has been found that the **nanoroughness increases as the Al/Al$_2$O$_3$ NWs are denser due to the effect of the micro-sized clusters**. **The micro roughness remains constant regardless from the Al/Al$_2$O$_3$ nanowire density.**

- The wetting angle revealed **hydrophilic behaviour of the Al/Al$_2$O$_3$ surface**. For all nanowire densities the contact angle with water was < 10°. **This result reflects that the micro effect is same for all densities**. The surface energy measurements revealed that the surface energy (E$_s$) decreases as the Al/Al$_2$O$_3$ NWs are denser. As the nanometer effect decreases, the E$_s$ also does. Last but not least, it was found that the contact angle with glycerin decreases as the Al/Al$_2$O$_3$ density increases. **The less dense coatings (LD-NWs and MD-NWs) showed oleophobic behaviour while the denser coatings (HD-NWs and UHD-NWs) are oleophilic**. The oleophilic behaviour of the Al/Al$_2$O$_3$ NWs has not been presented so far and could be promising in fields dealing with **oil/water separation and oil solvent materials**.

Last but not least, concerning the cell compatibility experiments all experiments pointed out that our Al/Al$_2$O$_3$ coatings may be good candidates as implant coating materials:

- **All cell compatibility results of Al/Al$_2$O$_3$ NWs with osteoblast and fibroblast cells point out a selective adhesion between the two cell types as the density of the Al/Al$_2$O$_3$ NWs increases. Osteoblast cells were favoured and fibroblast cells disfavoured.**

- The **gene expression of osteoblast is affected by the topography of the substrate. Some of osteogenic marker genes under investigation where significantly up-regulated after cultivation on the different nanowires, indicating that the nanowires were able to induce osteogenic differentiation processes.** Since we are working with nanotopographies it is difficult to discriminate between direct influences of the topography or indirect influence of the adsorbed protein layers on osteogenic differentiation.

- **It has been shown that Al/Al$_2$O$_3$ NWs substantially promote the fibroblast adhesion compared to untreated glass using CMR technique**. The highly porous inorganic layer provides a cell adhesion similar to that of fibronectin coating, which is a standard control substrate for most of the *in vitro* cell studies demanding cell adhesion.

Nevertheless, still some further experiments could be done following the lines of this thesis in order to have more certainty that Al/Al$_2$O$_3$ nanowire coatings are highly adequated for improvement of implant materials; FIB/SEM technique, which was used in this work for reconstruction of the Al/Al$_2$O$_3$ nanowire coatings, could be use to obtain a 3D model of the Al/Al$_2$O$_3$ NWs with cells cultured on them. Such analysis would permit a cross-sectional visualization of the cells cultured on the substrate providing a better understanding and visualization of the cell-surface interaction. Wear resistance experiments could be performed in order to know how resistant to mechanical abrasions the coatings are. This is a point of high importance from a surgical point of view. Additionally, co-culture of osteoblast and fibroblast cells would be essential for a better understanding of the selective adhesion and lastly, it would be very interesting to procede with *in vivo* osseointegration studies on the Al/Al$_2$O$_3$ nanowire coatings.

7

List of publications

The following publications were realized during the PhD time:

- J. Lee, L.K. Schwarz, C.K. Akkan, **M.M. Miró**, O.T. Abad, K.H. Schäfer, M. Veith, C. Aktas, Laser induced periodic patterns on biphasic core/shell nanowires for neurite guidance, Submitted to *physica status solidi*, 2012

- C. Aktas, J. Lee, A. Barnoush, **M. Martinez-Miró**, M. Veith, Alpha alumina synthesis by laser treatment of composite nanowires: functional applications, *Applied Surface Science*, (accepted) 2012

- J. Lee, **M.M.Miró**, C.K. Akkan, A. Haidar, W. Metzger, L.K. Schwarz, V. Zaporojtchenko, K.H. Schäfer, H. Abdul-Khaliq, M. Veith, Development of multi scale structured Al/Al_2O_3 nanowires for controlled cell guidance, *Journal of Biomedical Nanotechnology*, (accepted) 2012

- M. Veith, J. Lee, **M.M. Miró**, C.K. Akkan, C. Dufloux, O. C. Aktas, Bi-phasic Nanostructures for Functional Applications, *Chemical Society Reviews*, 2012

- C. Aktas, E. Dörrschuck, C. Schuh, **M.M. Miró**, J. Lee, N. Pütz, G. Wennemuth, W. Metzger, M. Oberringer, M. Veith, H. Abdul-Khaliq, Micro- and nanostructured Al_2O_3 surfaces for controlled vascular endothelial and smooth muscle cell adhesion and proliferation, *Materials Science and Engineering C*, 2012

- A. Haidar, **M. M. Miró**, J. Lee, C.K. Akkan, S. Brück, K. Löw, O.C. Aktas, H. Abdul-Khaliq Improved endothelialisation on silicon oxide (SiOx) thin film: possible approach for stent coatings, *Clinical research in cardiology*, 2011

- L. Schimmelpfennig, B. Schwab, W. Metzger, D. Sossong, C. Akas, **M. Martinez**, J. Lee, M. Veith, T. Pohlemann, M. Oberringer , Cell compatibility of micro- and nanostructured alumina surfaces prepared by chemical vapor deposition, *Tissue engineering*, 2011

- C. Aktas, A. Haidar, **M.M. Miró**, E. Dörrschuck, J. Lee, M. Veith, H. Abdul-Khaliq, Improved endothelialisation on nanostructured surfaces, *Advanced Materials Research*, 2011

- Aktas, M. Sander, **M.M. Miró**, J. Lee, C.K. Akkan, H. Smail, A. Ott, M. Veith, Enhanced fibroblast cell adhesion on Al/Al_2O_3 nanowires, *Applied Surface Science*, 2011

- M. Veith, O.C. Aktas, J. Lee, **M.M. Miró**, C.K. Akkan, K.H. Schäfer, U. Rauch, Biphasic nano-materials and applications in life sciences: 1D $A1/Al_2O_3$ nanostructures for improved neuron cell culturing, *Ceramic Transactions*, 2010

Patents:

- O.C. Aktas, M. Veith, J.Lee, H.Smail, **M. Martinez-Miró**

  Laminate having a one-dimensional composite strucutre

  Patent Application DE10 20120 021 691.7, 2010

- O.C. Aktas, M. Veith, C.K. Akkan, J.Lee, **M. Martinez-Miró**

  Coating for converting radiation energy

  Patent Application PCT/EP 2011/061694, 2011

Awards:

A.Haidar, **M. Martinez Miró**, C.K. Akkan, J. Lee, K. Löw, M. Veith, H. Abdul-Khaliq, C. Aktas

Laser interference patterned 1D nanostructures for vascular implant applications

OUTSTANDING RESEARCH AWARD

8th Nanoscience-Nanotechnology Congress & IANM 3rd World Congress, Ankara-Turkey, June 2012

8

References

[1] B.D. Boyan, T.W. Hummert, D.D. Dean, Z. Schwartz, *Biomaterials*, 1996; 17: 137-146.

[2] D.M. Brunette, B. Chehroudi, *J. Biomech. Engng*, 1999 ; 121: 49-57.

[3] K. Anselme, *Biomaterials*, 2000; 21: 667-681.

[4] B.D. Boyan, C.H. Lohmann, D.D. Dean, D.L. Cochran, Z. Schwartz, *Annu. Rev. Mater. Res.,* 2001; 31: 357-371.

[5] M. Dalby, *Med. Engng Phys.,* 2005; 27: 730-742.

[6] A. Ponche, M. Bigerelle, K. Anselme, *J. Engineering in Medicine*, 2010; 224 (12): 1471-1486.

[7] S. Hulbert, *Singapore: World Scientific Publishing*, 1993; 25–40.

[8] L.L. Hench, *J. Am. Ceram. Soc.,* 1991; 74: 1487-510.

[9] A. Walpole, E. Briggs, M. Karlsson, E. Palsgard, P. Wilshaw, *Materialwiss Werkst*, 2003; 34 (12): 1064-1068.

[10] C. Wang, G.A. Karlis, G.I. Anderson, C.R. Dunstan, A. Carbone, G. Berger, *J Biomed Mater Res A*, 2009; 90A (2): 419-428.

[11] Z. Weidong, L.Qibin, Z. Min, W. Xuding, *Journal of Biomedical Materials Research Part A*, 2008; 87A (2): 429-433.

[12] A. Oberlin, M. Endo, T. Koyama, Journal of Crystal Growth, 1976; 32 (3): 335–349.

[13] Z. Wei Pan, Z. Rong Dai, Z. Lin Wang, Science, 2001; 291: 1947-1949.

[14] J. C. Carbery, C. B. Alcock; US-Patent 5028404.

[15] K. S. Shamala, L. C. S. Murthy, K. R. Narasimha, *Mater. Sci. Eng. B*, 2004; 106 (3): 269-274.

[16] H. Bartzsch, D. Glosz, B. Bocher, P. Frach, K. Goedicke, *Surf. Coat. Technol.,* 2003; 174-175: 774-778.

[17] H. Exner, A.-M. Reinecke, M. Nieher, *J. Ceram. Process. Res.,* 2002; 3 (2): 66-69.

[18] J. Soro, A. Smith, C. Gault, *J. Eur. Ceram. Soc.*, 2007; 27 (2): 1469-1474.

[19] R. Gras, J.L. Duvail, T. Minéa, M. Dubosc, P.Y. Tessier, L. Cagnon, P. Coronel and J. Torres, *Microelectronic Engineering*, 2006; 83 (11-12): 2432-2436.

[20] J. Zhang, Y. Huang, J. Lin, X. X. Ding, C. Tang, S. R. Qi, *J. Solid State Chem.,* 2005; 178 (7): 2262-2266.

[21] A. Jagminas, J. Kuzmarskyte, L. Malferrari, M. Cuffiani, *Mater. Lett.,* 2007; 61 (14): 2896-2899.

[22] T.J. Webster, C. Ergun, R.H. Doremus, R.W. Siegel, R. Bizios, *Biomaterials*, 2000; 21 (17): 1803-1810.

[23] H. Liu, T.J. Webster, *Biomaterials*, 2007; 28 (2): 354-369.

[24] T.J. Webster, E.L. Hellenmeyer, R.L. Price, *Biomaterials*, 2005; 26 (9): 953-960.

[25] T.J. Webster, J.U.Ejiofor, *Biomaterials*, 2004; 25: 4731–4739.

[26] M. R. Noordin, K.Y. Liew, Ashok Kumar (Ed), InTech, 2010; ISBN 978-953-7619-86-2; 438.

[27] R.L. Price, L.G. Gutwein, L. Kaledin, F. Tepper, T.J. Webster, *Journal of Biomedical Materials research Part A*, 2003; 67A (4): 1284-1293.

[28] R. S. Wagner and W. C. Ellis, *Vapor-Liquid-Applied Physics Letters*, 1964; 4 (5): 89-90.

[29] E. I. Givargizov, *Journal of Crystal Growth*, 1975; 31: 20-30.

[30] Z.M. Wang Editor. One-dimensional nanostructures. Lecture notes in nanoscale science and technology 3, page 3.

[31] K.L. Choy, *Progress in Materials Science*, 2003; 48: 57–170.

[32] M.J. Hampden-Smith, T.T. Kodas, *Chem. Vap. Dep.,* 1995; 1 (1): 8-23.

[33] P. Auerkari, 1996; ISBN 951-38-4987-2

[34] D. Samélor, A.M. Lazar, M. Aufray, C. Tendero, L. Lacroix, J.D. Béguin, B. Caussat, H.Vergnes, J. Alexis, D. Poquillon, N. Pébère, A. Gleizes, C. Vahlas, *Journal of Nanoscience and Nanotechnology*, 2011; 11: 1-5.

[35] C.D. Chandler, M.J. Hampden-Smith, R.W. Schwartz, *Mater. Res. Soc. Symp. Proc.,* 1993; 310: 357.

[36] J.P. Carpenter, C.M. Lukheart, S.B. Milne, S.R. Stock, and J.E. Wittig, *Inorg. Chim. Acta.*, 1996; 251: 151-156.

[37] B.D. Fahlman, *Curr. Organic Chem.,* 2006; 10 (9): 1021-1033.

[38] N.L. Pickett, P.O´Brien, *Chem. Record.,* 2006; 10; 102.

[39] S. Mathur, M. Veith, H.Shen, and S. Hüfner, *Mater.Sci. Forum*, 2002; 341: 386-388.

[40] P. Werndrup, M.Verdenelli, F. Chassagneux, S. Parola, and V.G. Kessler, *J.Mater. Chem.,* 2004; 14: 344-350.

[41] V.G. Kessler, *J.Sol-Gel Sci. Technol.,* 2004; 32: 11-17.

[42] M.Veith, *J. Chem. Soc., Dalton Trans.,* 2002; 2405-2412.

[43] M. Veith, S. J. Kneip, S. Faber, E. Fritscher, *Mater. Sci. Forum*, 1998; 269: 303.

[44] M. Veith, K. Andres, *J. Metastable and Nanocrystalline Materials*, 2003; 15: 279-282.

[45] M. Veith, S. J. Kneip, A. Jungmann and S. Hüfner, *Z. Anorg. Allg. Chem.,* 1997; 623: 1507.

[46] M. Veith, N. Lecerf and M. Gasthauer, THERMEC 2000, TMS, Elsevier, Las Vegas, Nevada, USA, 2001.

[47] X. S. Fang, C. H. Ye, X. X. Xu, T. Xie, Y. C. Wu and L. D. Zhang, *J. Phys. Condens. Matter*, 2004; 16: 4157-4163.

[48] D. H. L. Ng, P. Yu, N. G. Ma, C. K. Lo, W. Y. Kwok, M. Y. Yau, C. Y. To, T. K. Li and C. J. Deng, *J. Eur. Ceram. Soc.,* 2006; 26: 1561-1565.

[49] C.Y. To, L.Y. Cheung, Y.F. Li, K.C. Chung, D.H.C. Ong and D. H. L. Ng, *J. Eur. Ceram. Soc*., 2007; 27: 2629-2634.

[50] M. Veith, E. Sow, U. Werner, C. Petersen and O. C. Aktas, *Eur .J .Inorg. Chem.,* 2008; 33: 5181-5184.

[51] Y. Wu, P. Yang, *J. Am. Chem. Soc.,* 2001; 123: 3165-3166.

[52] G. D. Lilly, J. Lee, K. Sun, Z. Tang, K. S. Kim and N. A. Kotov, *J. Phys. Chem. C*, 2008; 112: 370-377.

[53] O. C. Aktas, M. Veith, J. Lee, H. Smail, M. Martinez-Miró, Patent Application DE10 2010 021 691.7, 2010.

[54] O. C. Aktas, M. Veith. C. K. Akkan, J. Lee and M. Martinez-Miró, Patent Application PCT/EP 2011/061694, 2011.

[55] M. Veith, K. Jacobs and O. Bäumchen, Saarland University, unpublished results.

[56] W. Barthlott, C. Neinhuis, *Planta*, 1997; 202: 1-8.

[57] M. Veith, S. J. Kneip, *J. Mater. Sci. Lett.,* 1994; 13: 335.

[58] http://physics.nist.gov/Pubs/guidelines/TN1297/tn1297s.pdf

[59] L. Vecan (1195) Introduction and general discussion. In: Glocker DA, Shah SI (eds) Handbook of thin film process technology. Institut of Physics, Bristol, UK. B1.0:1-B1.0:12.

[60] W. Kern, V.S. Ban (1978) Chemical capour deposition of inorganic thin films. In: J.L. Vossen, W. Kern (eds) Thin film processes. Academic, New York, 257-331.

[61] M.L. Hitchman, K.F. Jensen (1993) Chemical vapour deposition: principles and applications. Academic, New York.

[62] J. Konrad, S. Zaefferer, D. Raabe, *Acta Mater.,* 2006; 54 (5): 1369-1380.

[63] F. Lasagni, A. Lasagni, C. Holzapfel, F. Mücklich, H.P. Degischer, *Advanced Engineering Materials*, 2006; 8 (8): 719-723.

[64] D. Weiss, G. Schneider, B. Niemann, P. Guttmann, D. Rudolph, G. Schmahl, *Ultramicroscopy*, 2000; 84: 185-197.

[65] M. Koguchi, H. Kakibayashi, R. Tsuneta, M. Yamaoka, T. Niino, N. Tanaka, K. Kase, M. Iwaki, J. *Electron* Microsc. 2001 ; 59 (3): 235-241

[66] A. Pyzalla, B. Camin, T. Buslaps, M. Di Michiel, H. Kaminski, A. Kottar, A. Pernack, W. Reimers, *Science*, 2005; 308: 92-95.

[67] X. S. Liu, X.H. Zhang, K.K. Sekhin, M.F. Adams, D.J. McMahon, J.P. Bilezikian, E. Shane, X. E. Guo, *Journal of Bone and Mineral Research*, 2010; 25 (4): 746–756.

[68] U.Bonse, F. Busch, O. Günnewig, F. Beckmann, R. Pahl, G. Delling, M. Hahn, W. Graeff, *Bone and Mineral*, 1994; 24: 25-38.

[69] R.E. Guldberg, C.L. Duvall, A. Peister, M.E. Oest, A.S. Lin, A.W. Palmer, M.E. Levenston, *Biomaterials*, 2008; 29 (28): 3757-61.

[70] M. Bashoor-Zadeh, G. Baroud, M. Bohner, *Acta Biomaterialia*, 2010; 6: 864-875.

[71] G. Möbus, R.C. Doole, B. J. Inkson, *Ultramicroscopy*, 2003; 96: 433-451.

[72] W. Steiger, F. Rudenauer, H. Gnaser, P. Pollinger, H. Studincka, *Mikrochim. Acta*, 1983 ; 20: 11-117.

[73] F.G. Rüdenauer, W. Steiger, *Mikrochem. Acta*, 1981; 76: 375-389.

[74] B.J. Inkson,T. Steer, G. Möbus, T. Wagner, *J. Microsc.,* 2001; 201 (2): 256-269.

[75] T.J. Steer, G. Möbus, O. Kraft, T. Wagner, B.J. Inkson., *Thin Solid Films*, 2002; 413: 147-154.

[76] B.J. Inkson, L. Mulvihill, G. Möbus, *Scripta Mater.*, 2001; 45: 753-758.

[77] M.D. Uchic, M.A. Groeber, D.M. Dimiduk, J.P. Simmons, *Scripta Mater.*, 2006; 55: 23-28.

[78] H.Z. Wu, S.G. Roberts, G. Möbus, B.J. Inkson, *Acta Mater.*, 2003; 51: 149-163.

[79] D.A. Matthijs de Winter, C.T.W.M. Schneijdenberg, M.N. Lebbink, B. Lich, A.J. Verkleij, M.R. Drury, B.M. Humbel, *J. Microsc.,* 2009 ; 233 (3): 372-383.

[80] M. Kato, T. Ito, Y. Aoyama, K. Sawa, T. Kaneko, N. Kawase, H. Jinnai, *J.Polym.Phys.*, 2007; 45: 677-683.

[81] S.S. Ray, *Polymer*, 2010; 51: 3966-3970.

[82] A. Velichko, PhD Thesis, Universität des Saarlandes, 2008.

[83] C.H. Arns, M.A. Knackstedta, W. Val'Pinczewskib, N.S. Martysc, *J. of Petroleum Science and Engineering*, 2004; 45: 41-46.

[84] M.A. Groeber, B.K. Haley, M.D. Uchic, D.M. Dimiduk, S. Ghosh, *Materials Characterization*, 2006; 57: 259–273.

[85] MAVI. Modular Algorithms for Volume Images. s.l.: ITWM, 2005.

[86] Amira visage imaging, user manual, 2008.

[87] J. Ohser, F. Mücklich, Statistical Analysis of Microstructures in Materials Science.s.l.: John Willey & Sons, 2000.

[88] C. Lang, J. Ohser, R.J. Hilfer, *Microsc.,* 2001; 202: 1-12.

[89] J. Ohser, W. Nagel., K. Schladitz, *Image Anal. Stereol.,* 2003; 22: 11-19.

[90] W. Nagel, J. Ohser, K.J. Pischang, *Microsc.*, 2000; 198: 54-62.

[91] L. Holzer, F. Indutny, P.H. Gasser, B. Münch, M. Wegmann, *J. Microsoc.*, 2004; 216 (1): 84-95.

[92] O. C. Aktas, PhD Thesis, Universität des Saarlandes, 2009.

[93] M. Gudiksen, C. Lieber, *Journal of the American chemical society*, 2000; 122: 8801-8802.

[94] E.A. Sow, PhD Thesis, Universität des Saarlandes, 2008.

[95] E.J. Davies; Conduction and Induction Heating, IEE Power Engineering Series III (1989).

[96] J.X. Lu, B. Flautre, K. Anselme, P. Hardouin, A. Gallur, M. Descamps, *J Mater Sci Mater Med*, 1999; 10(2) : 111–20.

[97] M. Mastrogiacomo, S. Scaglione, R. Martinetti, L. Dolcini, F. Beltrame, R. Cancedda, *Biomaterials*, 2006; 27(17): 3230–7.

[98] O. Gauthier, J.M. Bouler, E. Aguado, P. Pilet, G. Daculsi, *Biomaterials*, 1998; 19 (1–3): 133–9.

[99] V. Karageorgiou, D. Kaplan, *Biomaterials*, 2005; 26 (27): 5474–91.

[100] L. Sh, J.R. de Wijn, J. Li, P. Layrolle, K. de Groot, *Tissue Eng*, 2003; 9 (3): 535–48.

[101] M. Bohner, G.H. van Lenthe, S. Gruenenfelder, W. Hirsiger, R. Evison, R. Mueller, *Biomaterials*, 2005; 26 (31): 6099–105.

[102] F.A. Soldera, F.A. Lasagni, F. Mücklich (2011) In: F.A. Lasagni, A.F. Lasagni (eds.), Fabrication and Characterization in the Micro-Nano Range, Advanced Structured Materials, 10.

[103] H. Yang, A.C. Kot, *IEE Transactions on multimedia*, 2007; 9 (3): 475-486.

[104] S. Lavenus, G. Louarn, P. Layrolle, *International Journal of Biomaterials*, 2010; doi:10.1155/2010/915327

[105] J. Woo, D.C. Cannon, 17th ed. JB Henry, RA McPherson, Philadelphia, 1984; 133.

[106] R.L. Williams, S.A. Brown, K. Merrit, *Biomaterials*, 1988; 9: 181-186.

[107] S.S. Liao, F.Z. Cui, Y. Zhu, *J Bioact Compos Pol*, 2004; 19: 117-123.

[108] N. Huang, P. Yang, X. Cheng, Y. Leng, X. Zheng, G. Gai, Z. Zhen, F. Zhang, Y. Chen, X. Liu, T. Xi, *Biomaterials*, 1998; 19: 771-776.

[109] C.J. Murphy, N.R. Jana, *Adv. Mater.,* 2002; 14 (1): 80-82.

[110] J. Graham, M. Ries, L. Pruitt, *J Bone Joint Surg Am*, 2003; 85 (10): 1901-1908.

[111] K.A. Hing, B. Annaz, S.Saeed, P.A. Revell, T. Buckland, *Journal of materials science: materials in medicine*; 2005; 16: 467-475.

[112] E.P. Briggs, A.R. Walpole, P.R. Wolshaw, M. Karlsson, E. Palsgard, *Journal of materials science: materials in medicine*, 2004; 15: 1021-1029.

[113] S. Lavenus, M. Berreur, V. Trichet, P. Pilet, G. Louarn, P. Layrolle, *European Cells and Materials*, 2011; 22: 84-96.

[114] J. Ohser, F. Mücklich, Statistical Analysis of Microstructures in Materials Science, 2000, Wiley, Chichester.

[115] E. Detsi, E. De Jong, A. Zinchenko, Z. Vukovic, I. Vukovic, S. Punzhin, K. Loos, G. ten Brinke, H.A. De Raedt, P.R. Onck, J.T.M. de Hosson, *Acta Materialia*, 2011; 59: 7488–7497.

[116] A. Wittstock, V. Zielasek, J. Biener, C.M. Friend, M. Bäumer, *Science*, 2010; 327: 319-322.

[117] L.C. Nagle, J.F. Rohan, *Int J Hydr Energy*, 2010; doi:10.1016/ j.ijhydene.2010.09.077.

[118] C. Xu, X. Xu, J. Su, Y. Ding., *J Catal.,* 2007; 252 (2): 243-248.

[119] X.Y. Lang, H.T. Yuan, Y. Iwasa, *Chen MW. Scripta Mater.,* 2011 ; doi:10.1016/j.scriptamat.2011.01.038.

[120] H. Liu, G. Zhu, *J Power Sources*, 2007; 171 (2): 1054-1061.

[121] J. Weissmüller, R.N. Viswanath, D. Kramer, P. Zimmer, R. Würschum, H. Gleiter, *Science*, 2003; 300: 312-315.

[122] H.J. Jin, X.L. Wang, S. Parida, K. Wang, M. Seo, J. Weissmüller, *Nano Lett*, 2010; 10: 187-194.

[123] J. Biener, A. Wittstock, L.A. Zepeda-Ruiz, M.M. Biener, V. Zielasek, D. Kramer et al., *Nature Mater*, 2009; 8: 47-51.

[124] H.J. Jin, J. Weissmüller., *Adv Eng Mater*, 2010; 12 (8): 714-723.

[125] P.C. Carman, *Trans. Inst. Chem. Eng.,* 1937; 15: 150-166.

[126] H. I. Chang, Y. Wang, *Cells and Biomaterials*, 2011.

[127] M.M.C.G. Silva, L.A. Cyster, J.J.A. Barry, X.B. Yang, F.R.A.J. Rose, *Biomaterials*, 2006; 27: 5909-5917.

[128] C. Leber, H. Choi, S. Bose, A. Bandyopadhyay, *Material science and engineering*, 2010; 30: 71-77.

[129] K.E. Herold, A. Rasooly (editor). Lab-on-a-Chip Technology: Biomolecular Separation and Analysis. Caister Academic Press., 2009, ISBN 978-1-904455-47-9.

[130] A. Odgaard, H.J.G. Gundersen, *Bone*, 1993; 14: 173-182.

[131] B.K. Alldredge, K.K. Mary Anne, Y.L. Young, A. Wayne, B. Kradjan, J. Guglielmo (2009), Applied therapeutics: the clinical use of drugs. Philadelphia: Wolters Kluwer Health/Lippincott Williams & Wilkins. pp. 101–3.

[132] topnews.net.nz

[133] J.C. Russ, R.T. Dehoff, Practical Stereology. New York: Kluwer Academic/Plenum Publishers, 2000.

[134] K. Cai, J. Bossert, K.D. Jandt, *Colloids and Surfaces B: Biointerfaces*, 2006; 49: 136–144.

[135] J. Protivínský , M. Appleford, J. Strnad, A. Helebrant, *J.L. Ong, Int J Oral Maxillofac Implants*, 2007; 22: 542-550.

[136] Y. Yang, J. Tian, L. Deng, J.L. Ong, *Biomaterials*, 2002; 23: 1383-1389.

[137] G. Zhao, A.L. Raines, M. Wieland, Z. Schwartz, B.D. Boyan, *Biomaterials*, 2007; 28: 2821-2829.

[138] hand book spectrosky

[139] Y. Ekinci, H. H. Solak, J. F. Löffler, *Journal of Applied Phisics*, 2008; 104; P. 083107.

[140] C. D. Wagner, W. M. Riggs, L. E. Davis, J. F. Moulder, Handbook of X-ray Photoelectron Spectroscopy (Ed.: G. E. Muilenberg), Perkin-Elmer Corporation, Eden Prairie, Minnesota, USA, 1979

[141] J.Y. Martin, Z. Schwartz, T.W. Hummert, D.M. Schraub, J. Simpson, J. Lankford et al., *J Biomed Mater Res*, 1995; 29(3): 389-401.

[142] B.D. Boyan, L.F. Bonewald, E.P. Paschalis, C.H. Lohmann, J. Rosser, D.L. Cochran et al., *Calcif Tissue Int*, 2002; 71 (6); 519- 29.

[143] Z. Schwartz, P. Raz, G. Zhao, Y. Barak, M. Tauber, H. Yao et al., *J Bone Joint Surg Am*, 2008; 90 A (11): 2485-98.

[144] W. Att, N. Tsukimura, T. Suzuki, T. Ogawa, *Int J Oral Maxillofac Implants*, 2007; 22 (5): 719-28.

[145] K. Kieswetter, Z. Schwartz, T.W. Hummert, D.L. Cochran, J. Simpson, D.D. Dean et al., *J Biomed Mater Res*, 1996; 32 (1): 55-63.

[146] A.L. Raines, R. Olivares-Navarrete, M. Wieland, D.L. Cochran, Z. Schwartz, B.D. Boyan, *Biomaterials*, 2010; 31 (18): 4909-17.

[147] D. Buser, R.K. Schenk, S. Steinemann, J.P. Fiorellini, C.H. Fox, H. Stich, *J Biomed Mater Res*, 1991; 25 (7): 889-902.

[148] D.L. Cochran, R.K. Schenk, A. Lussi, F.L. Higginbottom, D. Buser, *J Biomed Mater Res*, 1998; 40 (1): 1-11.

[149] D.L. Cochran, *J Periodontol*, 1999; 70 (12): 1523-39.

[150] D.L. Cochran, D. Buser, C.M. ten Bruggenkate, D. Weingart, T.M. Taylor, J.P. Bernard et al., *Clin Oral Implants Res*, 2002; 13 (2): 144-53.

[151] A.M. Lipski, C.J. Pino, F.R. Haselton, I.W. Chen, V.P. Shastri, *Biomaterials*, 2008; 29 (28): 3836-46.

[152] A.S.G. Curtis, N. Gadegaard, M.J. Dalby, M.O. Riehle, C.D.W. Wilkinson, G. Aitchison, *IEEE Trans Nanobioscience*, 2004; 3 (1): 61-5.

[153] M.O. Riehle, M.J. Dalby, H. Johnstone, A. MacIntosh, S. Affrossman, *Mater Sci Eng C*, 2003; 23 (3): 337-40.

[154] B.C. Ward, T.J. Webster, *Mater Sci Eng C*, 2007; 27 (3): 575-8.

[155] R.A. Gittens, T. McLachlan, R. Olivares-Navarrete, Y. Cai, S. Berner, R. Tannenbaum, Z. Schwartz, K.H. Sandhage, B.D. Boyan, *Biomaterials*, 2011; 32: 3395-3403.

[156] P.E. Mazeran, L. Odoni, J.L. Loubet, *Surf. Sci.*, 2005; 585: 25-37.

[157] E.P. Degarmo, J.T. Black, R.A. Kohser, 2003; Materials and Processes in Manufacturing (9th ed.), Wiley, p. 223, ISBN 0-471-65653-4.

[158] K. Kieswetter, Z. Schwartz, D.D. Dean, B.D. Boyan, *Crit Rev Oral Biol Med*, 1996; 7 (4): 329-345.

[159] G. Balasundaram, T.J. Webster, *Nanomedicine*, 2006; 1 (2): 169-176.

[160] T. Young, *Phil. Trans. R. Soc. Lond.,* 1805; 95: 65-87.

[161] R.N. Wenzel, *Industrial and engineering chemistry*, 1936; 28 (8): 988.

[162] A. B. D. Cassie, S. Baxter, *Trans. Faraday Soc.,* 1944; 40: 546-551

[163] P. G. de Gennes, *Reviews of Modern Physics*, 1985; 57 (3): 546-551.

[164] R. Shuttleworthn, L. J. Bailey, the spreading of a liquid over a rough solid, 1948; 16-22.

[165] A.M. Cazabat, S. Gerdes, M.P. Valignat, S. Villette, *Interface Science*, 1997; 5 : 129–139.

[166] C. Dufloux, PhD Thesis, Universität des Saarlandes, 2012 (submitted).

[167] K.M. Yamada, D.W. Kennedy, *The journal of cell biology*, 1984; 99: 29-36.

[168] D. Khang, J. Lu, C. Zao, K. M. Haberstroh, T.J. Webster, Biomaterials, 2008; 29: 970-983.

[169] P. Boutin, P. Christel, J.M. Dorlot, A. Meunier, A. de Roquancourt, D. Blanquaert, S. Herman, L. Sedel, J. Witvoet, *Journal of Biomedical Materials Research*, 1988; 22: 1203-1232.

[170] P. Roach, D. Eglin, K. Rohde, C.C. Perry, *J Mater Sci: Mater Med*, 2007; 18: 1263–1277.

[171] M.B. Nasab, M.R. Hassan, *Trends Biomater. Artif. Organs*; 2010; 24 (1): 69-82.

[172] E. Eisenbarth, nanotechnologically modified biomaterials, text book, nanobiotechnology course, 2010.

[173] F. Barrère, C.A. van Blitterswijk, K. De Groot, *International Journal of Nanomedicine*, 2006; 1 (3): 317–332.

[174] R.A. Latour, Encyclopedia of Biomaterials and Biomedical Engineering, 2005; DOI: 10.1081/E-EBBE-120041856.

[175] D.E. Hugues, D.M. Salter, S. Dedhar, R. Simpson, *Journal of Bone and Mineral Research*, 1993; 8 (5): 527-533.

[176] P.G. Robery, C.T. Brighton, G. Friedlaender, J.M. Lane, Editor.1994, Normal Bone Formation: Structure, in Bone formation and repair American Academy of Orthopaedic Surgeons: Rosemont, IL p.3-12.

[177] A.S. Posner, Bone mineral and mineralization process, in Bone and Mineral research, WA, Peck, Editor.1998, Elsevier: Amsterdam.p.65-116

[178] R.S. Tuan. Development skeletogenesis, in Bone formation and repair, Brighton CT, Friedlander G, Lane JM, Editor 1994, American Academy of Orthopaedic Surgeons: Rosemont, IL. P. 13-22

[179] B. Albert, D. Bray, J. Lewis, M. Raff, K. Roberts, J.D. Watson. Differentiated cells and maintenance of tissues, in Molecular biology of the cell. Editor. 1994, Garland Publishing: New York. P. 1138-1193

[180] J.L. Katz, Orthopedic Applications, structure and properties of calcified tissues, in Biomaterials Science: An introduction to Materials in Medicine, Ratner BD, Hoffman AS, Schoen FJ, Lemons JE, Editor.1996, Academic Press: San Diego. P.335-340

[181] J. Soro, A. Smith, C. Gault, *J. Eur. Ceram. Soc.,* 2007; 27 (2): 1469.

[182] R. Gras, J.L. Duvail, T. Minéa, M. Dubosc, P.Y. Tessier, L. Cagnon, P. Coronel, J. Torres, *Microelectronic Engineering*, 2006; 83 (11-12): 2432-2436.

[183] C. Petersen, PhD Thesis, Universität des Saarlandes, 2007.

[184] M. Veith, C. Petersen, O. C. Aktas, W. Metzger, M. Oberringer, T. Pohlemann, M. Müller and S. Gerbes, *Mater. Lett.*, 2008; 62: 3842.

[185] M. Veith, O.C.Aktas, W.Metzger, D.Sossong, H.Ullah Wazir, I.Grobelsek, N.Pütz, G.Wennemuth, T.Pohlemann, M.Oberringer, *Biofabrication*, 2010; 2: 035001

[186] M. Veith, O.C. Aktas, J. Lee, M.M. Miró, C.K. Akkan, K.H. Schäfer, U. Rauch, *Ceram. Trans.,* 2010; 214: 117.

[187] J. Lee, M.M. Miró, C.K. Akkan, A. Haidar, W. Metzger, L.K. Schwarz, V. Zaporojtchenko, K.H. Schäfer, H. Abdul-Khaliq, M. Veith, 2012, accepted.

[188] C. Aktas, E. Dörrschuck, C. Schuh, M.M. Miró, J. Lee, N. Pütz, G.Wennemuth, W. Metzger, M. Oberringer, M. Veith, H. Abdul-Khaliq, *Materials Science and Engineering: C*, 2012; 32 (5): 1017–1024.

[189] C. Aktas, A. Haidar, M.M. Miró, E. Dörrschuck, J. Lee, M. Veith, H. Abdul-Khaliq, *Advanced Materials Research*, 2011; 324: 105-108.

[190] A. Haidar, Master Thesis, Universität des Saarlandes, 2011.

[191] Invitrogen: http://products.invitrogen.com

[192] Roche: https://www.roche-applied-science.com

[193] O.T. Fackler, R. Grosse, *J Cell Biol*., 2008; 181 (6): 879–84.

[194] G.T. Charras, C.K. Hu, M. Coughlin, T.J. Mitchison, *J. Cell Biol.*, 2006; 175 (3): 477–90.

[195] P.K. Mattila, P. Lappalainen, *Nature reviews: Molecular cell biology*, 2008; 446-453.

[196] C.G. Galbraith, K.M. Yamada, J.A. Galbraith, *Science*, 2007; 315: 992–995.

[197] M.A. Partridge, E.E. Marcantonio, *Mol. Biol. Cell*, 2006; 17: 4237–4248.

[198] M.B. Steketee, K.W. Tosney, *J. Neurosci*., 2002; 22: 8071–8083.

[199] V. Vasioukhin , C. Bauer, M. Yin, E. Fuchs, *Cell*, 2000; 100: 209–219.

[200] U. Meyer, A. Büchter, H.P. Wiesmann, U. Joss, D.B. Jones, *European cells and materials*, 2005; 9: 39-49.

[201] G. Gronowicz, M.B. McCarthy, *Journal of Orthopedic Research*, 1996; 14: 878-887

[202] I. Degasne, M.F. Baslé, V. Demais, G. Huré, M. Lesourd, B. Grolleau, L. Mercier, D. Chappard, *Calcif Tissue Int*, 1999; 64: 499–507.

[203] C.H. Lohmann, E.M. Tandy, V.L. Sylvia, A.K. Hell-Vocke, D.L. Cochran, D.D. Dean, B.D. Boyan, Z. Schwarz, *Journal of Biomedical Materials Research*, 2002; 26 (2): 204-213.

[204] M. Jäger, C. Zilkens, K. Zanger, R. Krauspe, *Journal of Biomedicine and Biotechnology*, 2007; ID 69036; 1-19.

[205] C. Schmidt, D. Kaspar, M.R. Sarkar, L.E. Claes, A.A. Ignatius, *Journal of Biomedical Materials Research*, 2002; 63 (3): 252-261.

[206] R.L. Jilka, R.S. Weinstein, T. Bellido, A.M. Parfitt, S.C. Manolagas, *Journal of Bone and Mineral Research*, 1998; 13 (5): 793-802.

[207] J.S. Hayes, I.M. Khan, C.W. Archer, R.G. Richards, *European Cells and Materials*, 2010; 20: 98-108.

[208] P.A. Fernandez, A. Ott, N. Aksel, L. Heymann, P.A. Pullarkat, Shear rheology of a cell monolayer, *New J. Phys.,* 2007; 9: 419.

[209] O. C. Aktas, M. Sander, M. M. Miró, J. Lee, C. K. Akkan, H. Smail, A. Ott and M. Veith, *Appl. Surf. Sci.*, 2011; 257 (8): 3489-3494.

[210] N. Aksel, P. Fernandez, L. Heymann, A. Ott, P. Pullarkat, Eur. Patent Application EP 071141782 (2007).

[211] G. Todaro, H. Green, *J. Cell Biol*., 1963; 17: 299–313.